THERMOCHEMICAL MODELING AND CHEMICAL VAPOR DEPOSITION OF TWO-PHASE BORIDES IN THE Hf-Si-B-Cl-H SYSTEM

by

Eric Joseph Wuchina

Dissertation submitted to the Faculty of the

Virginia Polytechnic Institute and State University

in partial fulfillment of the requirements for the degree of

DOCTOR OF PHILOSOPHY

in

Materials Engineering Science

APPROVED:

Dr. Jesse J. Brown, Jr.
Chairman

Dr. Ronald S. Gordon

Dr. Ronald G. Kander

Dr. William T. Reynolds

Dr. Stephen Kampe

Dr. Inna G. Talmy

June 8, 1995
Blacksburg, Virginia

THERMOCHEMICAL MODELING AND CHEMICAL VAPOR DEPOSITION OF TWO-PHASE BORIDES IN THE Hf-Si-B-Cl-H SYSTEM

by
Eric Joseph Wuchina
Dr. Jesse J. Brown, Jr, Chairman
Department of Materials Engineering Science
(ABSTRACT)

Advanced, very high temperature materials that are ablation-resistant in oxidizing atmospheres are needed to withstand the severe environments found in rocket engine and aerospace vehicle applications. Boride-based coatings that form a protective layer during oxidation have been found to withstand these extreme conditions. Chemical vapor deposition has been chosen as a viable processing technique for producing these coatings. It is expected that two-phase boride coatings will have enhanced oxidation resistance over the single-phase materials by forming an oxide/glass layer to seal the base material from direct attack. Thermochemical modeling of CVD reactions was done to predict the processing conditions for the deposition of two-phase HfB_2-SiB_6 or HfB_2-SiB_4 coatings. The SOLGASMIX-PV computer program was used for these calculations, which were based on $ZrCl_4$, $SiCl_4$ BCl_3, and H_2 reactant gases. An array of temperatures (1100, 1300, and 1500K), total pressures (0.02, 0.1, and 1 atm.) and excess hydrogen concentrations (10:1, 25:1, and 50:1 H:(Zr + Si + B + Cl)) were investigated. These calculations show that two-phase HfB_2-SiB_6 and HfB_2-SiB_3 coatings are possible over a wide range of processing conditions, suggesting that a wide variety of two-phase compositions with a diverse

population of microstructures can be deposited. This points to the possibility of optimizing oxidation resistance of these coatings by varying the processing conditions. A hot-wall CVD reactor was designed and constructed specifically for deposition reactions in this system. It was found to be necessary to separately deliver $SiCl_4$ and BCl_3 to the hot zone to prevent reactions between them and to eliminate interference with the in-situ hafnium chlorination reaction. SiB_4, rather than SiB_6, was the preferred deposition product in the Si-B-Cl-H system. HfB_2 was the only compound found to deposit in the Hf-B-Cl-H system. Both borides coatings exhibited several different surface morphologies. The separate delivery of BCl_3 and $SiCl_4$, while necessary to prevent their gas phase reaction, caused reactant concentration gradients at the substrate surface due to poor mixing. This resulted in a variation of microstructural features across the substrate surface (both domed and faceted morphologies were deposited at the same temperatures), suggesting that reactant supersaturation is more important in determining surface morphology than temperature, pressure, and hydrogen concentration at the conditions studied. The first successful deposition of the two-phase HfB_2-SiB_4 coating was accomplished. Analysis of these two-phase coatings again reveals a broad range of microstructural characteristics, and the compositional gradients across the substrate surface also suggest the need for better gas mixing.

ACKNOWLEDGEMENTS

The author would like to thank the following:

- My parents, whose patience, love, guidance, and encouragement have made me a better person.

- My brother and sister, for always supporting me.

- Dr. and Mrs Jesse Brown, for helping spark my interest in research and my pursuit of a graduate education, as well as being good friends.

- Dr. Inna Talmy, for being my friend, mentor and avid supporter.

- Rick Lowden, for patiently answering my incessant questions. Our invaluable discussions have made much of this research possible.

- Bill, Robbie, Flynn, Heidi, Stephanie, and the other professional tailgaters for helping me recapture my school spirit, and making me remember why Tech is such a great place - its the people.

- Dr. Ron Kander, for encouraging a camaraderie among the students and fostering student-faculty interactions at the weekly "Fluid-Flow and Aerodynamics" Seminars.

- Drs. Bill Reynolds and Steve Kampe for valuable scientific discussions.

- Dr. Ronald Gordon, for teaching me valuable lessons that needed to be learned.

- Dr. Jim Zaykoski, for helping edit this manuscript and being a good friend.

- Dave Graham, for patiently teaching me the intricacies of SOLGASMIX.

- Dr. Bob Brizzolara, for assisting with the scanning electron microscopy.

- Drs. Mark Opeka and Bill Messick for supporting this research through the NSWC Materials Technology Program.

- Justin Cooper, for assisting with the x-ray calibration curve.

- Drs. James Sheehan and Robert Shinavski, for their advice on CVD reactions.

- The whole Fest crew, for remaining my friends for a long, long time.

- The staff at the High Temperature Materials Lab Users Facility, ORNL, for their assistance with the electron microprobe analysis.

- Susan Fleming and Lee Ann Ellis for helping to make my scheduled visits to campus less stressful.

TABLE OF CONTENTS

LIST OF TABLES....vii

LIST OF FIGURES....viii

CHAPTER 1. INTRODUCTION....1

CHAPTER 2. LITERATURE REVIEW

2.1 Boride Materials for Oxidation Resistance....3
2.2 Properties of SiB_4 and HfB_2....8
2.3 Phase Equilibria in the Hf-Si-B System....10
2.4 Chemical Vapor Deposition....15
2.4.1 Reaction Types....15
2.4.2 CVD Systems....18
2.4.3 Other Coating Technologies....20
2.4.4 Advantages and Disadvantages....22
2.4.5 Applications....23
2.4.6 Non-Coating Applications....26
2.5 CVD of Two-Phase Coatings....32
2.6 CVD of HfB_2 and SiB_4....36

CHAPTER III. RESULTS AND DISCUSSION....39

3.1. Thermodynamic Modeling of CVD Reactions....39

3.1.1 Results of Modeling Reactions in the Zr-Si-B-Cl-H System....39
3.1.2 Discussion of Thermodynamic Modeling Results....49
A. Calculation Technique Used for Modeling....49
B. Discussion of Modeling Zr-Si-B-Cl-H System....52
C. The Role of Thermodynamics in CVD....55

3.2 Reactor Design....63

3.2.1 Hot-Wall vs. Cold-Wall Systems....63
3.2.2 Reactor Design....66
3.2.3 Gas Delivery System....68
$SiCl_4$ Flowrate Calibration....72
3.2.4 Pressure Control and Exhaust System....78

3.3 Source Materials....81

3.4 Experimental Procedure....82

3.5. Characterization....85

3.6 Deposition and Characterization of CVD Coatings....86

3.6.1 SiB_4....87
3.6.2 HfB_2....97
3.6.3 HfB_2-SiB_4....103

3.7 Discussion of CVD Results....132

3.7.1 Kinetics and Mass Transport Issues during CVD....132
3.7.2 Microstructural Development - Nucleation and Growth of Films..129
3.7.3 Uniformity and Adherence of CVD Coatings....154
3.7.4 Deposition Results....157

3.8 SUMMARY....162

3.9 CONCLUSIONS....163

APPENDIX A....165

REFERENCES....191

VITA....200

LIST OF TABLES

Table 1. Oxidation Behavior of HfC and HfB_2 in 7% Oxygen as a Function Temperature and Time[2]

Table 2. The Properties of HfB_2 and SiB_4

Table 3. Thermodynamic Properties of Gaseous Species Used in SOLGASMIX Calculations

Table 4. Thermodynamic Properties of Condensed Species Used in SOLGASMIX Calculations

Table 5. Properties of Hf and Zr[78]

Table 6. Experimental Conditions for SiB_4 Deposition

Table 7. Experimental Conditions for HfB_2 Deposition

Table 8. Experimental Conditions for Two-Phase HfB_2-SiB_4 Deposition

LIST OF FIGURES

Figure 1. Thermogravimetric Analysis of CrB_2, CrB_2/Al_2O_3, and $CrB_2/Al_2O_3/SiB_4$ Ceramics[7]

Figure 2. The Si-B System[23]

Figure 3. The Hf-B System[27]

Figure 4. The Hf-Si System[26]

Figure 5. The Hf-Si-B System at 1300°C[28]

Figure 6. Schematic of Forced Flow, Thermal Gradient Chemical Vapor Infiltration of Preform for Producing Ceramic Matrix Composites[35]

Figure 7. Scanning Electron Micrograph of Si_3N_4 Deposited on SiC Fibers at Hot Face[35]

Figure 8. Scanning Electron Micrograph of Cross Section of Composite Produced by CVI[35]

Figure 9. Output from SOLGASMIX Computer Program at 1100K and 0.01 atm.

Figure 10. Ternary CVD Phase Diagram at P = 1 atm., T = 1300K, and H/(Zr + Si + B + Cl) = 10

Figure 11. Binary CVD Phase Diagram at $X_{ZrCl4} = 5\%$

Figure 12. Schematic Diagram Illustrating Sequentially-Linked Steps in a CVD Process[84]

Figure 13. Original Design for the Hot-Wall CVD Reactor

Figure 14. $SiCl_4$ Bubbler

Figure 15. Calibration Curve of $SiCl_4$ Flowrate vs. H_2 Flowrate

Figure 16. Final Design of Hot-Wall CVD Reactor

Figure 17. Schematic of Complete Chemical Vapor Deposition System

Figure 18. Scanning Electron Micrographs of Fibrous Coating on Graphite

Figure 19. X-Ray Diffractogram of SiB_4 Coating on Graphite

Figure 20. Scanning Electron Micrographs of SiB_4 Coating Showing Domed Morphology

Figure 21. Scanning Electron Micrographs of SiB_4 Coating Showing Preferred Growth of Some Grains

Figure 22. Scanning Electron Micrographs of SiB_4 Coating Showing Faceted Morphology

Figure 23. X-Ray Diffractogram of HfB_2 Coating on Graphite

Figure 24. Scanning Electron Micrographs of HfB_2 Coating Showing Porous Coating with Spherical Morphology

Figure 25. Scanning Electron Micrographs of HfB_2 Coating Showing Domed Morphology

Figure 26. Scanning Electron Micrographs of HfB_2 Coating Showing Faceted Morphology

Figure 27. X-Ray Diffractograms of HfB_2-SiB_4 Powder Mixtures for Quantitative Analysis

Figure 28. X-Ray Calibration Curve

Figure 29. X-Ray Diffractogram of HfB_2-SiB_4 Two-Phase Coating on Graphite

Figure 30. Scanning Electron Micrographs of HfB_2-SiB_4 Coating Showing a) Separate Faceted Crystals, b) Crystals Inpinging Upon One Another, c, d) Continuous Dense Coating

Figure 31. Scanning Electron Micrographs of HfB_2-SiB_4 Coating Showing a) Discontinuous and b) Continuous Domed Grains

Figure 32. Scanning Electron Micrographs of HfB_2-SiB_4 Coating Showing Preferred Grain Growth

Figure 33. Scanning Electron Micrographs of HfB_2-SiB_4 Coating Showing Development of Clusters of Preferred Growth Grains

Figure 34. Scanning Electron Micrographs of HfB_2-SiB_4 Coating Showing a) Spherical, and b) Platelet Morphology

Figure 35. Scanning Electron Micrographs of HfB_2-SiB_4 Coating Showing Development of Second-Phase Clusters

Figure 36. Scanning Electron Micrographs of HfB_2-SiB_4 Coating Showing Faceted and Domed Morphologies, Along with Branched Clusters

Figure 37. Scanning Electron Micrographs of HfB_2-SiB_4 Coating Showing Clusters Growing from Faceted Grains

Figure 38. Scanning Electron Micrographs of HfB_2-SiB_4 Coating Showing a) Dark and Light Colored Surface and b) Transition Region at Higher Magnification

Figure 39. Scanning Electron Micrographs of HfB_2-SiB_4 Coating Showing Development of Darker Phase

Figure 40. a) Scanning Electron Micrograph Image, b) Hf x-ray map, and c) Si x-ray map of HfB_2-SiB_4 Coating

Figure 41. Scanning Electron Micrographs of HfB_2-SiB_4 Coating Showing Coexistance of Faceted SiB_4 and Domed HfB_2 Morphologies

Figure 42. Backscattered Electron Image of Faceted Crystal on Domed Primary Coating, from HfB_2-SiB_4 Coating

Figure 43. Scanning Electron Micrographs of HfB_2-SiB_4 Coating Showing Two Different Morphologies

Figure 44. Scanning Electron Micrographs of HfB_2-SiB_4 Coating Showing Coexistence of Two Different Morphologies

Figure 45. a) Scanning Electron Micrograph, b) Hf X-Ray Map, and c) Si X-Ray Map of HfB_2-SiB_4 Coating Showing That Small White Crystals are HfB_2 and Continuous Dark Phase is SiB_4

Figure 46. Backscattered Electron Image of HfB_2-SiB_4 Coating Showing Two Different-Sized Faceted Crystals on the Domed Primary Phase

Figure 47. a),b) Scanning Electron Micrographs and, c) Si X-Ray Map of HfB_2-SiB_4 Coating Showing Faceted Second Phase on Domed Continuous Phase

Figure 48. a) Scanning Electron Micrograph, b) Backscattered Electron Image, and c) Si X-Ray Map of HfB_2-SiB_4 Coating Showing Highly Faceted Second Phase on a Domed Continuous Phase

Figure 49. Typical Temperature Dependence of Deposition Rate

Figure 50. Typical Flow Rate Dependence on Deposition Rate[104]

Figure 51. The Basic Modes of Film Growth[31]

Figure 52. Scanning Electron Micrographs Showing Development of Morphology of SiC Films[106]

Figure 53. Effect of Processing Conditions on Microstructure[32]

Figure 54. Schematic Representation of Coating Microstructures Deposited by CVD a) Columnar Grains with Domed Tops; b) Faceted, Columnar Grains; and c) Equiaxed Grains[34]

Figure 55. The Evolution of Columnar Microstructures During CVD[107]

Figure 56. The Integration of Descrete Particles into the Growing Film[108]

Figure 57. Hook-Shaped Whisker Formed by Repetitive Change in Growth Direction[109]

Figure 58. Scanning Electron Micrographs of Textured Surfaces Deposited by CVD[111]

CHAPTER 1. INTRODUCTION

1.1 Background

The borides of the group IV-VII transition metals display a number of unique properties, including high melting point, very high hardness and strength, high thermal conductivity and relatively low thermal expansion, as well as high chemical stability. This combination of properties make borides potential candidates for various structural applications requiring high temperature strength, thermal stress resistance, and stability in severe environments (especially oxidizing atmospheres). Borides can have application as protective coatings, cutting tools, armor shielding, and electrodes for aluminum smelting. In particular, boride-based materials are being considered as excellent candidates for high-temperature ablation-resistant components (such as nosetips and leading edges) on advanced aerospace vehicles.

The goal of this research is to produce two-phase HfB_2-SiB_4 composite coatings. It is expected that this coating will have enhanced oxidation resistance over the end-member boride materials. Since it is anticipated that the necessary material properties do not need to be exhibited by the bulk material structure, a surface coating can be applied to achieve the desired performance characteristics for the given application. Chemical vapor deposition has been chosen as the processing route for making these

materials due to the ability to control compound stoichiometry, chemical purity, coating morphology, orientation, and crystal structure. (Additionally, the use of this material as a matrix in composites processed by chemical vapor infiltration can be a goal.)

This dissertation will thus seek to give the reader a proper background for the proposed research. The Introduction (Section I) will include a review of CVD processing, a summary of boride material development, the properties HfB_2 and SiB_4 ceramics, previous CVD studies of these compounds, the known phase equilibria in the Hf-Si-B system, the two-phase materials that have been deposited by CVD, thermodynamics and kinetics issures in CVD, and a discussion of the coating microstructures that can be produced by CVD. The thermochemical modeling of reactions in the Zr-Si-B-Cl-H system using the SOLGASMIX computer program will be described, with a discussion of the relevance of the approach, in the Section II. The design and construction of a hot-wall CVD reactor specifically for the preparation of two-phase coatings in this chemical system and the experimental procedure will be covered in Section III. The results, discussion, and conclusions are given in Section IV.

CHAPTER 2. LITERATURE REVIEW

2.1 Boride Materials for Oxidation Resistance

Advanced, very high temperature materials that are ablation-resistant in oxidizing environments are needed to withstand the rapid heating and cooling environments found in rocket engine and aerodynamic vehicle applications. The sharp edges needed for maneuverability, as well as the temperatures and stresses endured during these missions make current carbon ablators and silicon-based ceramics unsuitable for advanced applications. The ability to withstand high heating rates to 2760°C, plus long exposure times at lower temperatures, coupled with near zero recession rates are the target materials selection criteria for re-entry and engine applications. NASA, NSWC, and the Air Force all have programs aimed at advanced materials development. Several materials research programs are focused on either the modification of known baseline materials or creating novel compounds or composites for these applications.

Silicon-based ceramics are excellent in oxidizing environments at temperatures up to 1500°C due to the formation of a passive, self-healing SiO_2 layer. At higher temperatures or reduced pressures, the formation of SiO gas (active oxidation) causes rapid material loss and ultimately, component failure.

The driving force for this research is to develop a material that will

oxidize at a slow rate to minimize the material recession. The performace criteria are based on the needs of a particular application, with the effects of exposure times, heating rates, oxygen pressures, and mechanical stresses all contributing to the selection of a particular material. At the temperatures, oxygen pressures, and stresses experienced during service, all materials will undergo some degree of oxidation, ablation, or melting. For most applications, the formation of an oxide layer is not necessarily detrimental to performance. The oxide needs to be able to withstand the surface stresses and temperatures while protecting the underlying structure.

Graphite and carbon/carbon composites use ablation techniques to dissipate the high heat fluxes generated during service, but the need for shape stability has precluded their use for some applications. Refractory carbides (non-silicon-based) have excellent high temperature oxidation resistance, but at lower temperatures, recession rates can be high due to the lack of a self-healing glass layer to protect the bulk structure.

The focus of recent studies of high-temperature oxidation-resistant materials has been based on an extensive program at ManLabs funded by the Air Force[1] in the 1960's. In this program, a variety of materials, including borides, carbides, silicides, graphites, and refractory metals were evaluated for high-temperature oxidation resistance, with HfB_2 and ZrB_2, emerging as the most versatile materials for a wide array of conditions. HfB_2

was found to form a thin oxide layer in plasma arc tests. A comparison of the oxidation behavior of HfC and HfB_2 over the temperature range 1500-2200°C for exposure times of 10 minutes to 10 hours is shown in Table I[2,3]. It is seen that HfB_2 performs much better than HfC at lower temperatures and shorter times.

Clougherty[4], Hinze[5] and Rasky[6] have reported that additions of up to 20% SiC to HfB_2 and ZrB_2 improved the oxidation resistance of the diborides due to the formation of a continuous glass layer. (HfB_2 and ZrB_2 both form adherent, high-melting temperature oxides, with HfB_2 slightly ouperforming ZrB_2. Both HfO_2 and ZrO_2 undergo phase transformations at high temperatures that might affect performance. Recent evidence suggests that since the HfO_2 goes through this transformation at higher temperatures, it happens closer to the outer surface, and doesn't affect oxide adherence.) Early stages of oxidation showed a parabolic rate dependence, suggesting that diffusion through the oxide layer is the rate controlling mechanism. Below 1100°C, a porous ZrO_2 scale forms, with B_2O_3 liquid filling the void space to protect the underlying structure from direct oxidation. Above 1100°C, boria vaporizes and at 1400°C, it is no longer protective. The SiC addition, at temperatures above 1200°C, helps to form a borosilicate glass that retards the vaporization of boria and acts as an effective barrier to oxygen diffusion. SiC is only slightly oxidized at 1300°C, with SiC particles

still embedded in the ZrO_2 and glass scale. The addition of other silicon-bearing compounds, such as Si_3N_4 or metal silicides were also found to improve oxidation performance. Recent work[7] has shown that different boride materials do not oxidize in the same manner; the formation of a continuous protective layer is system dependent. NbB_2 shows a slight weight loss at $T > 1100°C$, due to the concurrent formation of niobium oxide and evaporation of boria. CrB_2, on the other hand, shows a significant weight gain that levels out at 1100°C. The Cr_2O_3 and B_2O_3 react to form a continuous chromium borate ($CrBO_3$) film that acts as an effective diffusion barrier. The hot-pressed boride monoliths studied by the Air Force, however, were found to suffer from poor thermal shock resistance and low fracture toughness, and the emergence of SiC, Si_3N_4, and ceramic composites reduced interest in boride materials during the 1970's and 1980's.

The purpose of this research is to integrate recent knowledge with the results of previous researchers. The substitution of SiB_4 for SiC in the HfB_2-SiC composites should still provide increased oxidation resistance over pure HfB_2 by the formation of a borosilicate glass that seals the pores and cracks in the high-melting temperature HfO_2 that forms from the oxidation of HfB_2. This substitution is done to provide a simpler system for co-deposition, as the co-deposition of borides and carbides might be kinetically unfavorable, as described in Section 2.5.

Table 1. Oxidation Behavior of HfC and HfB_2 in 7% Oxygen as a Function Temperature and Time[2]

Temp. (°C)	HfC Oxide Thickness (μm)			HfB_2 Oxide Thickness (μm)		
	10 min	1 h	10 h	10 min	1 h	10 h
1500	96	236	746	6	15	47
1700	179	438	1,385	24	60	190
1800	233	571	1,804	114	684	6,840
1900	296	725	2,294	264	1,584	15,840
2100	451	1,104	3,491	1,200	7,200	72,000
2200	542	1,327	4,199	2,304	13,824	138,240

2.2 Properties of SiB_4 and HfB_2

The group IV diborides display a number of unique properties, including high melting point, very high hardness and strength, high thermal conductivity and relatively low thermal expansion, as well as high chemical stability. The high hardness and good thermal and electrical properties have made these materials useful in cutting tool, armor shielding, and electrode applications[8]. It is primarily the good oxidation behavior and high melting temperatures displayed by these materials that make them attractive for future aerospace applications. Some material properties of HfB_2 are listed in Table II[9]. The oxidation behavior of HfB_2 was reviewed in the previous section.

The existence of the silicon borides was first reported in the 1900's by Moisan and Stock[10]. A surge in interest in these materials during the early 1960's centered around the low specific gravity, oxidation, mechanical, and electrical behavior of these compounds to make lightweight structures and electronic devices. Several methods have been used to prepare pure SiB_4 ceramics. The reaction of the elements in air at elevated temperatures by Brewer[11] and Stavrolakis[12] was not successful, but later work by Colton[13] and Tremblay and Angers[14] utilized an argon atmosphere to produce the compound, with excess silicon or boron later etched away to leave pure SiB_4. Samsonov[15] used hot pressing of the elemental powders or a thermite

reaction between SiO_2 and B_2O_3 to produce the tetraboride.

Characterization of these materials has been reported by many of these researchers. X-ray diffraction studies by Brosset and Magnuson[16] and Matkovich[17] showed that this material has a rhombohedral crystal structure, with lattice parameters (and other properties) given in Table 2. Feigelson and Kingery[18] and Rizzo[19] describe the oxidation of SiB_4 in terms of the production of a thin borosilicate layer that is protective up to the decomposition temperature of 1400°C. Talmy, Zaykoski, and Wuchina[20] have found that the addition of SiB_4 to CrB_2-based ceramics have resulted in a dramatic improvement in the oxidation resistance, as shown in Figure 1.

Table 2. The Properties of HfB_2 and SiB_4

	HfB_2	SiB_4
Melting/Decomposition Temperature (°C)	3380	1400
Elastic Modulus (GPa)	500 (10% decrease above 1000°C)	300
Density (g/cm^3)	10.7	2.42
Hardness (kg/mm^2)	2900	2000
Crystal Structure	Hexagonal	Rhombohedral
Lattice Parameters (Å)	a = 3.15, c = 3.48	a = 6.33, c = 12.74
Thermal Expansion (x 10^6 mm/mm/K)	$\alpha_a = 5.21$ $\alpha_c = 6.03$	$\alpha_{bulk} = 5.8$

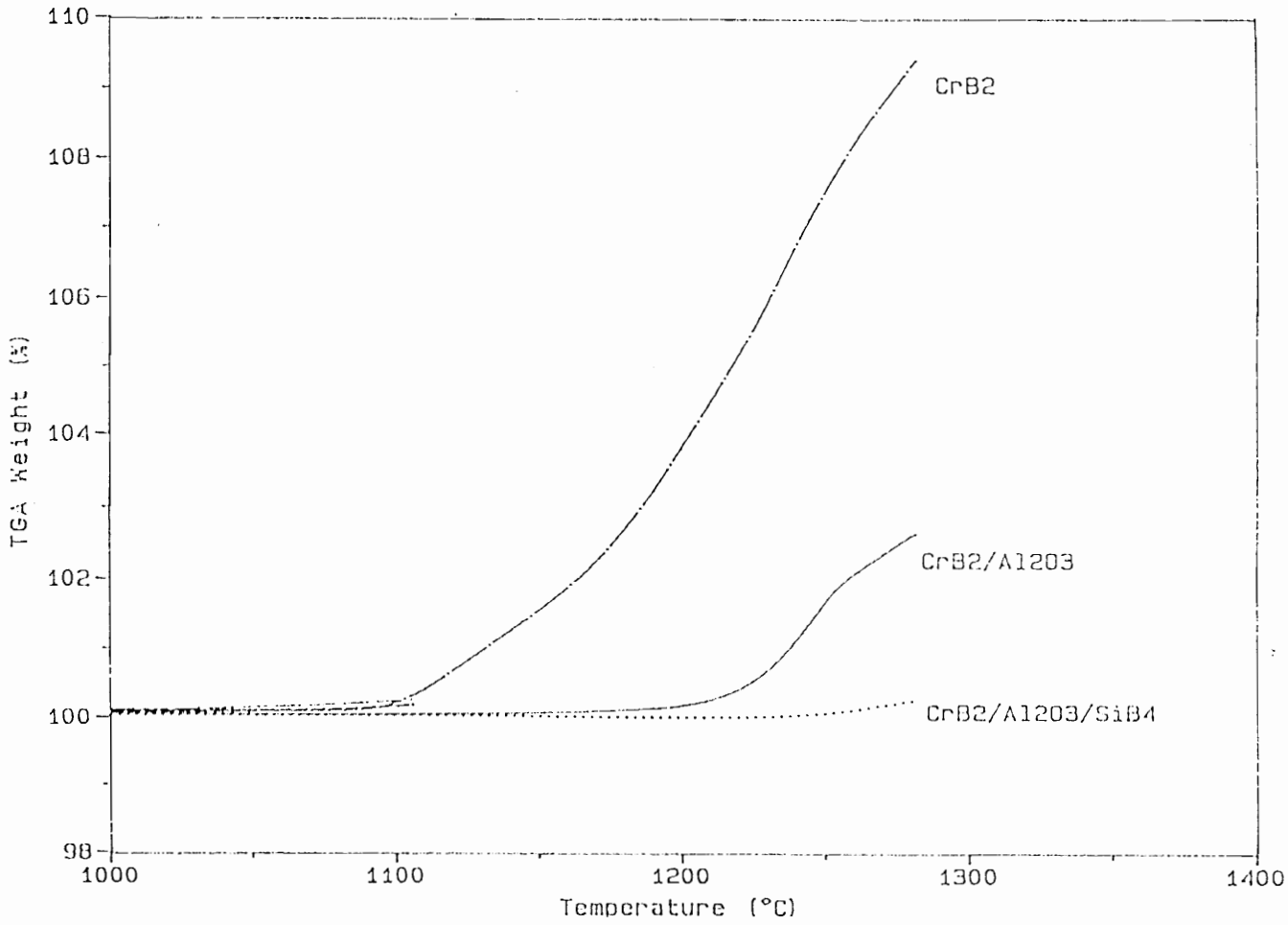

Figure 1. Thermogravimetric Analysis of CrB_2, CrB_2/Al_2O_3, and $CrB_2/Al_2O_3/SiB_4$ Ceramics[7]

2.3 Phase Equilibria in the Hf-Si-B System

i. The Si-B System

There have been a number of studies of compounds in the Si-B system. There has been some controversy regarding the composition of the lower boride phase. Early work by Moisan[10] identified this phase as SiB_3, while subsequent reports listed this phase as SiB_4 [13,16,17,19,21]. This lower boride has been reported to be a nonstoichiometric phase, SiB_n, with $n = 2.8$ to 5. Presently, it seems pretty well established that this phase is SiB_4, with the JCPDS Powder Diffraction Files[22] listing it as the tetraboride. The Si-B system contains two other stable compounds, SiB_6 and another non-stoichiometric compound, commonly given as SiB_{14}. The phase equilibrium diagram constructed by Olensinski and Abbaschian[23] shown in Figure 2 is generally accepted as the best representation of this system.

ii. The Hf-B System

Rudy and Windisch[24] first established the phase equilibrium (Shown in Figure 3) for the Hf-B system based on the work of a number of researchers. Two compounds, the high-melting temperature diboride (HfB_2) and monoboride (HfB) are reported. A complete review of the equilibria, phase stoichiometry, solubility, crystal chemistry, and thermodynamic data is given by Rogl and Potter[25].

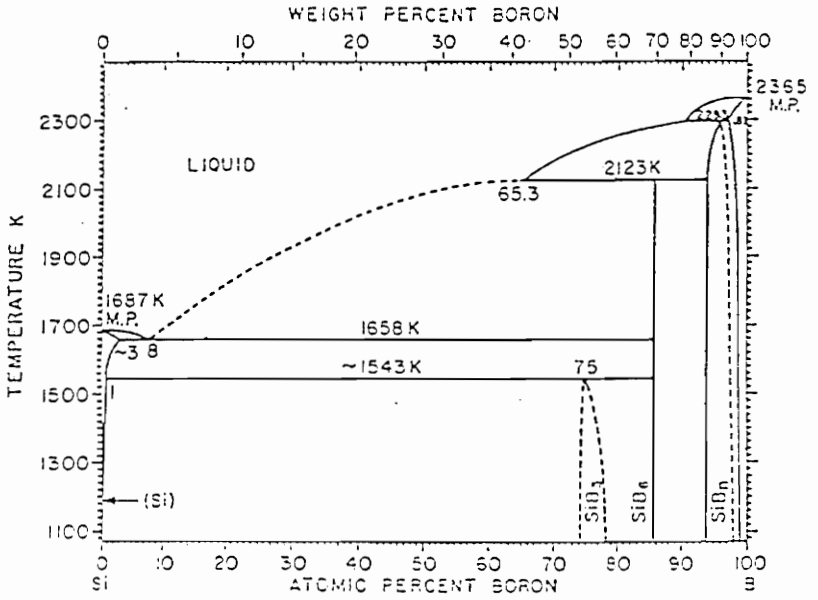

Figure 2. The Si-B System[23]

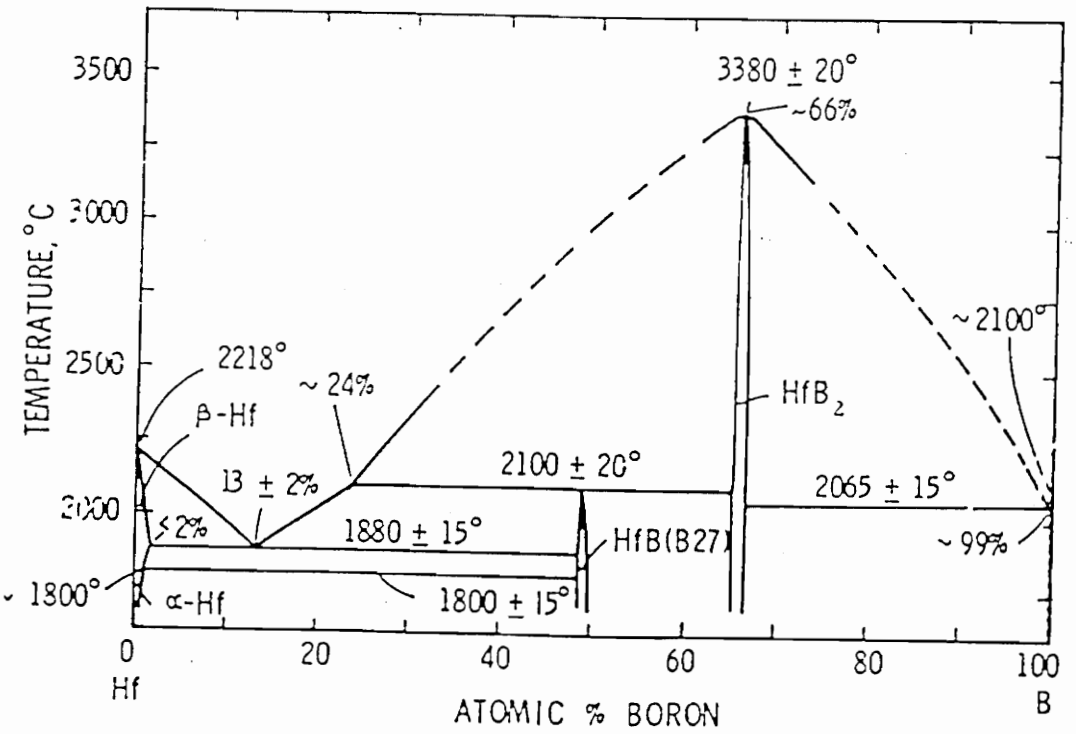

Figure 3. The Hf-B System[27]

iii. The Hf-Si System

Gokhale and Abbaschian[26] assessed the phase diagrams reported for the Hf-Si System, and concluded that the diagram of Brukl[27], shown in Figure 4, is most accurate. A discussion of the formation and melting temperatures, as well as crystal structure data for the five compounds in this system are given in this review. Thermodynamic data for these compounds have not been reported.

iv. The Hf-Si-B System

Rudy[28] published the 1300°C isothermal section for the Hf-Si-B system, as seen in Figure 5. This is the only known investigation of this ternary system. A ternary compound identified as a $D8_8$- Nowotny phase of composition $Hf_{52}Si_{38}B_{10}$ was reported.

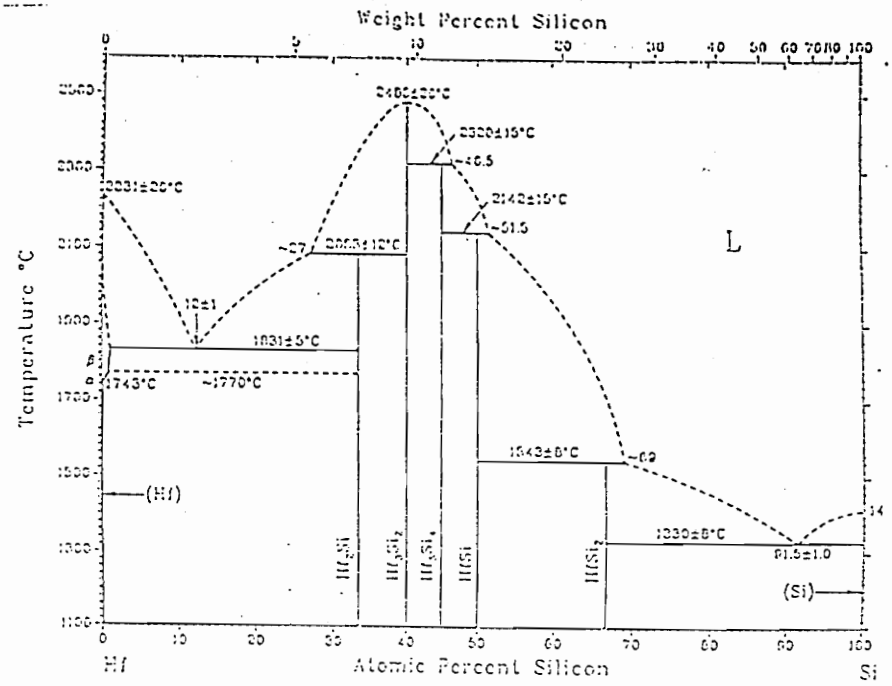

Figure 4. The Hf-Si System[26]

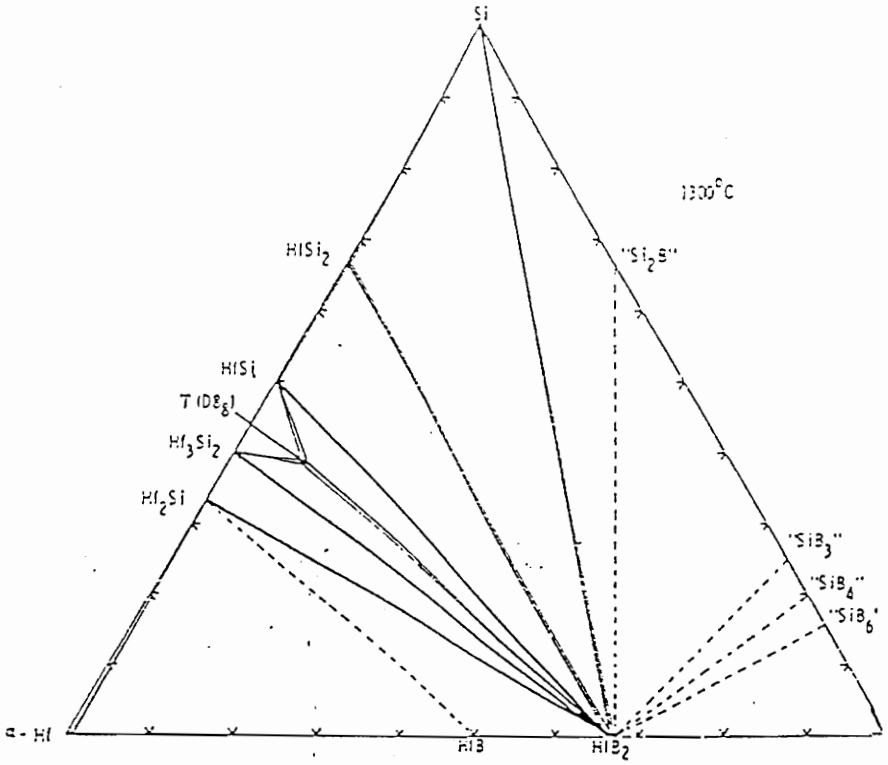

Figure 5. The Hf-Si-B System at 1300°C[28]

2.4 Review of Chemical Vapor Deposition

Chemical vapor deposition (CVD) is a process where gaseous precursors flow into a reactor, and chemical reactions take place to produce a solid coating on a substrate plus gaseous reaction products. In conventional CVD processes, the thermal energy supplied by the heated substrate drives the reaction, and product gases are removed from the reaction zone by fresh reactant gases continually supplied to the substrate.

CVD is not a new process. Its first practical use was in the 1880's, with tungsten deposits made by the hydrogen reduction of WF_6 being used to improve the strength of incandescent filaments. The iodine decomposition work of Van Arkel and deBoer[29] during the 1920's is commonly referred to as the origin of modern CVD technology. The production of high-purity refractory metals by the carbonyl (Mond) process was the other major pre-WWII use of CVD. The 1960's and 1970's brought the greatest advances in CVD technology, due to the development of semiconductor fabrication and the introduction of plasma and metal-organic technologies.

2.4.1 Reaction Types

The chemical reaction is the basic element of the CVD process. These deposition reactions can be classified into several general categories, all widely used in industrial production processes. These include: thermal

decomposition (pyrolysis), reduction, and disproportionation reactions[30].

The simplest reaction is pyrolysis. In this reaction, a molecule is broken apart, either into a simpler molecule or its elements. A common example of this type of reaction is the decomposition of hydrocarbons, such as methane, to form amorphous carbon, graphite, or diamond by the reaction

$$CH_4 \rightarrow C\ (s) + 2H_2\ (g).$$

Hydride, carbonyl, and halide decomposition reactions are widely used in the electronics industry.

Reduction reactions involve the lowering of the oxidation state of a gaseous specie. The hydrogen reduction of halide precursors, such as

$$WF_6 + 3H_2 \rightarrow W(s) + 6HF(g),$$

to make refractory metals like tungsten at much lower temperatures than the corresponding pyrolysis reactions. The co-reduction of halides to form high-temperature compounds (such as carbides, nitrides, borides) is a very important commercial process, since the high melting or sintering temperatures of these materials make other processing techniques uneconomical. An example of this type of reaction would be:

$$TiCl_4 + 2BCl_3 + 5H_2 \rightarrow TiB_2 + 10HCl.$$

Compound formation involving both pyrolysis and reduction reactions, such as

$$TiCl_4 + CH_4 \rightarrow TiC + 4HCl$$

are also common.

Silicon carbide is a commercially important material, and one of the most widely deposited CVD materials, so a special mention of precursors used in making SiC films is important. A number of researchers have investigated a variety of precursors to form SiC, starting from simple pyrolysis/reduction reactions with $SiCl_4$ and C_6H_6 through $SiHCl_3$ and CCl_4 that led to the development of volatile compounds containing both silicon and carbon in the same molecule. (CH_3SiCl_3 is widely used for making SiC for high-temperature structural applications.) The choice of precursor is based on the properties of the coating desired, and involve thermodynamic and kinetic considerations discussed later.

Disproportionation reactions are possible when volatile compounds have different degrees of stability at different temperatures. This is common when the base metal can exist in multiple valence states, with the lower valent state more stable at higher temperatures. The metal can be deposited when the lower-valent halide disproportionates at low temperatures, and regenerates the higher valent halide. This reversible reaction type is widely used for the production of GaAs films[30,31].

While not traditionally considered CVD reactions, carburization and nitridation involve gas-metal reaction to form solid films and deserve mention here. In these cases, the substrate participates in the reaction to form the

coating. The diffusion of metal to the coating or nonmetal through the coating to the coating/substrate interface controls the reaction and coating properties[32].

2.4.2 CVD Systems

As mentioned previously, traditional CVD reactions are thermally activated. This type of system is referred to as conventional CVD. There are two types of reactor design commonly used, based on the source of thermal energy supplied to the substrate. A hot-wall reactor uses resistively heated elements to supply heat to the whole furnace, producing a large hot zone with minimal temperature gradients. Cold-wall reactors, on the other hand, utilize the electrical properties of the substrate to directly heat it by induction or direct resistance; nothing but the substrate gets hot. (Other classifications of reactors, including closed/open and batch/continuous reactor designs will not be reviewed in this thesis.) A more in-depth discussion of thermal CVD reactors, along with the design of gas handling and pressure control systems will be carried out in Section 3.2.

Other CVD processing systems have been developed to produce lower deposition temperatures than traditional thermal CVD reactions require. These include gas activation techniques, such as plasma-, laser-, and photolytic- CVD, or the use of low decomposition-temperature gases, known as metal-organic CVD[30,31,32].

In plasma assisted CVD (PACVD), the reaction is enhanced, or activated, by a plasma. The plasma is achieved by increasing the temperature of the gas to a high enough level to strip the gas atoms of their electrons. For fully dissociating the gas atoms, the gas temperatures need to be exceedingly high. High chamber temperatures can be used to produce plasmas, but two other methods of producing a plasma without increasing substrate temperatures are the low frequency (arc) discharge or high frequency electric field (glow discharge). By decomposing the gas molecules into electrons, ions, atoms, and molecules, the highly reactive fragments allow the CVD reaction to occur at a much lower substrate temperature. Low melting temperature metals, such as aluminum, sensitive electronic components, and even plastics can be coated using plasma reactors. An example of the unique conditions generated by plasmas is in the deposition of diamond. Thermodynamically a high-pressure phase, diamond can be deposited at low pressures by a combination of reactive etching of more thermodynamically stable graphitic deposits by atomic hydrogen, along with the stabilization of sp3 bonding on the as-growing diamond surface.

Two other methods of activating the CVD reactions are with thermal laser or photolytic sources. In laser-assisted CVD, a laser produces local heating in a substrate, with the gas molecules absorbing little energy due to the wavelength of light used. The deposition mechanisms and reaction

chemistries are the same as in conventional thermal CVD. In photolytic CVD, the chemical reaction is induced by the energy from a light source, which has sufficient energy to break the chemical bonds in the gas molecules. Since heat is not required to drive the deposition reaction, the substrate can be held a room temperature.

Another special area of CVD processing involves the use of metal-organic precursors. These chemicals can be dissociated at lower temperatures than traditional metal halide precursors, allowing deposition temperatures to be significantly lowered. MOCVD is very important in the electronics industry for the deposition of Group III-V semiconductor compounds.

2.4.3 Other Coating Technologies

Chemical vapor deposition is just one gas-phase molecular-forming technique available to produce films and coatings for a variety of applications. Its versatility and advantages make one of the most widely utilized processing techniques in industry. There are, however, many other processing routes available for the formation of thin and thick films. These alternate processes will be reviewed in this section to give a better understanding to where CVD "fits in" in the commercial arena. These other major deposition processes include the use of liquid precursors (sol-gel, painting, dipping), electrolytic reactions(electroplating, fused-salt

electrolysis), particulate precursors (plasma-spraying, flame spraying) and physical vapor deposition, or PVD (evaporation, sputtering, ion plating, molecular beam epitaxy).

While painting and dipping are very well known and have a wide variety of industrial applications, sol-gel processing is more of an emerging technology. This technique uses a liquid reactive precursor that forms a colloidal suspension (sol) that goes through a gelling stage before drying and firing. Control of shrinkage and cracking have limited widespread use of this technology outside the laboratory.

Electrolytic coatings also have widespread industrial usage. While inexpensively producing thick protective coatings for corrosion protection applications, the preparation of thin films can be a problem due to porosity and inclusions. Environmental concerns are also an issue. Ion implantation, a major part of the semiconductor industry, uses accelerated ions to impact the surface and change its behavior.

Particulate deposition is an inexpensive route for producing coatings. However, these techniques are more amenable to producing thick coatings for corrosion and wear protection, with thin electronic or optical films not readily prepared by these methods.

Physical vapor deposition (PVD) processes are widely used in the electronics and optical industries. It is, like CVD, a vapor phase process.

But, unlike CVD, it is a condensation process that does not require a chemical reaction to form the product. Evaporation is the simplest PVD process, involving the heating (by resistance, laser beam, arc discharge, or electron beam) of a material above its boiling temperature, and then condensing it on a cold substrate. This process necessitates the use of a high-vacuum system, but good deposition rates are possible. Adhesion problems and the line-of-sight nature of this process limit applications to mostly metal materials for optical and decorative coatings. Sputtering involves the bombardment of a target material by gas ions accelerated by high voltages. Atoms from the target are ejected and deposit on the substrate, again in a line-of-sight fashion. Ultra-high vacuums are needed for this process, resulting in lower deposition rates.

2.4.4 Advantages and Disadvantages of CVD

One of the major attractions of CVD is its versatility. Unlike the other techniques, it has the ability to produce a wide range of metals, alloys, intermetallics, and ceramics (carbides, nitrides, borides, silicides, and oxides). The chemical composition can be controlled such that graded, layered, and mixed-phase coatings can be produced. Grain size and morphology can be varied (as discussed in Section 3.7.2). High densities and good adhesion to the substrate can also be obtained. Very high-purity materials can be produced (due to the high purity of the gaseous precursors)

at a fraction of the melting or sintering temperatures. The deposition rates (throwing power) are much greater than those attainable by PVD processes[33]. The ability to coat complex shapes, since it is not a line-of-sight process, is one of the principal advantages. Expensive high-vacuum equipment is generally not needed for CVD processing, and with readily-available precursors and the re-processing of unreacted gases, this technique is economically competitive.

CVD is not a panacea for every application, and does have some drawbacks. The relatively high deposition temperatures for the most widely used halide reactions can limit the choice of substrate materials. (This has led to the spin-off PACVD and MOCVD technologies discussed above. However, the metal-organic precursors are expensive and not available for all materials, and plasma systems tend to be expensive and limited to flat substrate geometries.) Gas handling and containment , as well as off-gas scrubbing are also important issues.

2.4.5 Applications of CVD

CVD is a versatile materials processing technique that is used in a wide variety of industries. Traditionally, CVD coatings have been used to modify the surface characteristics, including corrosion-, oxidation-, or wear-resistance of substrate materials. Frequently, engineered materials possess the required mechanical properties for a given application, but lack the

necessary surface characteristics for an application. Oftentimes, it is more economical to apply a thin coating to a component that to fabricate the entire part from the more costly or difficult-to-fabricate material. Carbide, oxide, nitride, and diamond coatings on tool bits, extrusion dies, bushings, and other high-wear components have higher harness and thermal capabilities, allowing greater machine speeds, less downtime for worn component replacement, and greater product lifetimes than uncoated versions, while the toughness of the base metal component is retained. Noble-metal and ceramic coatings on carbon-carbon and graphite structures in rocket nozzles and leading edges have increased operating temperatures and performance capabilities of aircraft and rockets. CVD coatings offering resistance to chemical attack are used extensively in the chemical, plastics and metals industries for handling corrosive liquids and abrasive slurries.

The extensive use of CVD in the electronics and optical industries deserves a more detailed analysis. Thin films produced by CVD reactions are used in the fabrication of solid-state devices. Insulators, dielectrics, semiconductors, conductors, and magnetic materials can all be deposited by CVD. The benefits of uniform coverage (without the shadowing possible in line-of-sight PVD processing), the ability to produce high-quality thin films makes CVD a desirable technology. The development of low-deposition temperature metal-organic precursors was spurred mainly by the need to

produce high-purity electronic devices. Al_2O_3 and SiO_2 have been used for capacitor dielectrics and as protective packaging materials. Refractory nitrides have been employed as barrier coatings, gate and packaging materials. Aluminum nitride and diamond films, with high thermal conductivity, are employed as substrate materials for thermal management. Thin film technologies, specifically CVD, have played a critical role in the development of integrated devices, where a million components can now be put on a single chip.

Silicon, gallium arsenide, germanium, and more recently silicon carbide and diamond semiconductor materials are all produced by CVD processes. The recent development of single-crystal SiC substrates by cold-wall CVD has led to the emerging technology areas of high-temperature, high-power devices. (This is due to the wider bandgap of SiC than the other materials, with diamond semiconductors being an infant technology.) Epitaxial semiconductors are an indispensable part of every microelectronic system, and CVD lends itself very well to making these materials due to the ease of in-situ doping. (This is especially important in covalently-bonded materials, like SiC or diamond, where the addition of dopants by solid-state diffusion would be difficult.)

Optoelectronic materials combine special electrical with optical properties (transmission, reflection, absorption) to provide unique capabilities

for a wide range of applications. The Group III-V and II-VI semiconductor compounds are the most important materials for these devices, including photodiodes, light-emitting diodes (LEDs), lasers, photovoltaics, and ferroelectrics. Among the wide array of commercial and military applications are: compact disc players, laser printers, radar detectors, cellular telephones, television, fiber-optic communications, photo-and non-contact switches, and IR sensors[30].

2.4.6 Non-Coating Applications of CVD

One of the main attractions of CVD is that it is not limited in application to just depositing a coating on the exterior of a substrate. CVD is used on a wide scale to produce fibers (boron, silicon carbide, and refractory metals) for polymer-, ceramic- and metal-matrix composites. TiB_2, HfN and TiC whiskers are also grown by CVD techniques. The production of highly pure ceramic and metal powders, with particle sizes down to the nanometer scale, is an emerging technology area in CVD. (The growth of whiskers and powders is not desirable when preparing dense coatings, however. The conditions necessary for whisker growth and powder formation will be discussed in later sections.) Free standing monolithic shapes, such as graphite, boron nitride, and refractory metal crucibles, rods, tubes, nozzles, electrodes, and radomes have been produced on mandrels or fugitive substrates.

The application of CVD technology to making ceramic matrix composites deserves special attention. With the inherent brittleness of ceramic materials, catastrophic failure of monolithic structures is a major problem. The lack of ductility in ceramics due to the strong bonding in ceramics cause stresses from applied loads to be concentrated at flaws such as voids, notches, scratches, and grain boundaries. In order to "engineer" fracture toughness, fiber-reinforced ceramic matrix composites are being developed. The use of fibers or whiskers to bridge or deflect the crack, or break to absorb the crack energy produces some damage tolerance in the material. Traditional ceramic processing techniques, such as die-pressing or slip casting, with subsequent pressureless sintering or hot-pressing, are not well-suited for handling surface-sensitive whiskers. Fiber abrasion, orientation and uneven firing shrinkage result in lower strengths and toughness in the final body. Continuous-fiber reinforcement, necessary for some high-loading applications, require the infiltration of the matrix material into the porous fiber preform. Directed metal oxidation (Lanxide process) following molten metal infiltration is an area of interest, but is limited to a few metal/fiber systems. Liquid infiltration with sol-gel precursors also has some advantages, but the need for multiple infiltration/drying steps and matrix cracking remain problems. A modification of the CVD process, called chemical vapor infiltration (CVI)[34], allows the precursor gases to diffuse, or

be forced[35], through a porous fiber preform before reacting at the fiber surface, as shown schematically in Figure 6. In this manner, the matrix material is built-up over time, as shown in Figures 7 and 8[36], with final densities of up to 95% reported. The modification of the fiber/matrix interface by the pre-deposition of a different material can enhance the fiber pullout, leading to greater damage tolerance and higher fracture toughness.

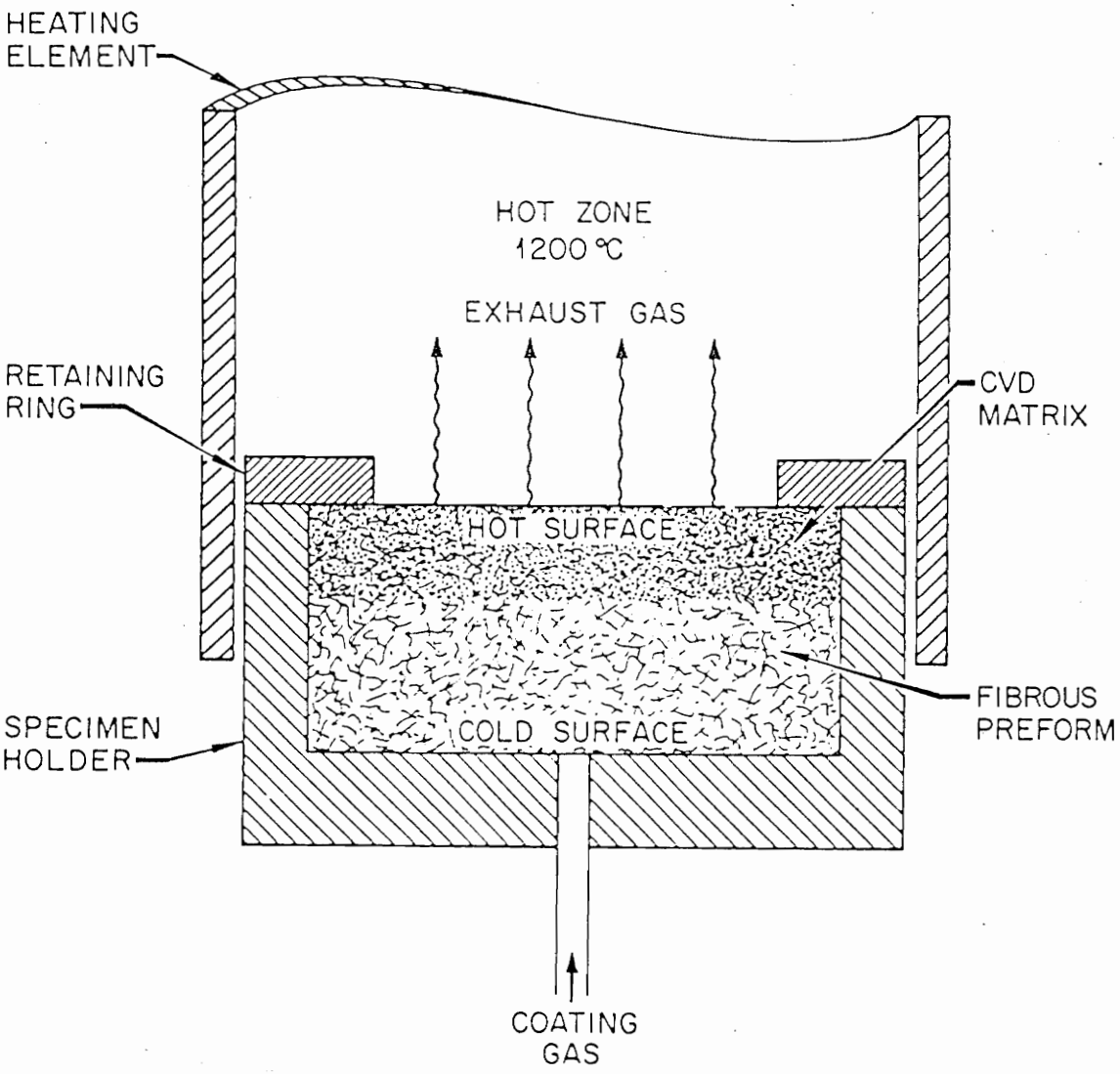

Figure 6. Schematic of Forced Flow, Thermal Gradient Chemical Vapor Infiltration of Preform for Producing Ceramic Matrix Composites[35]

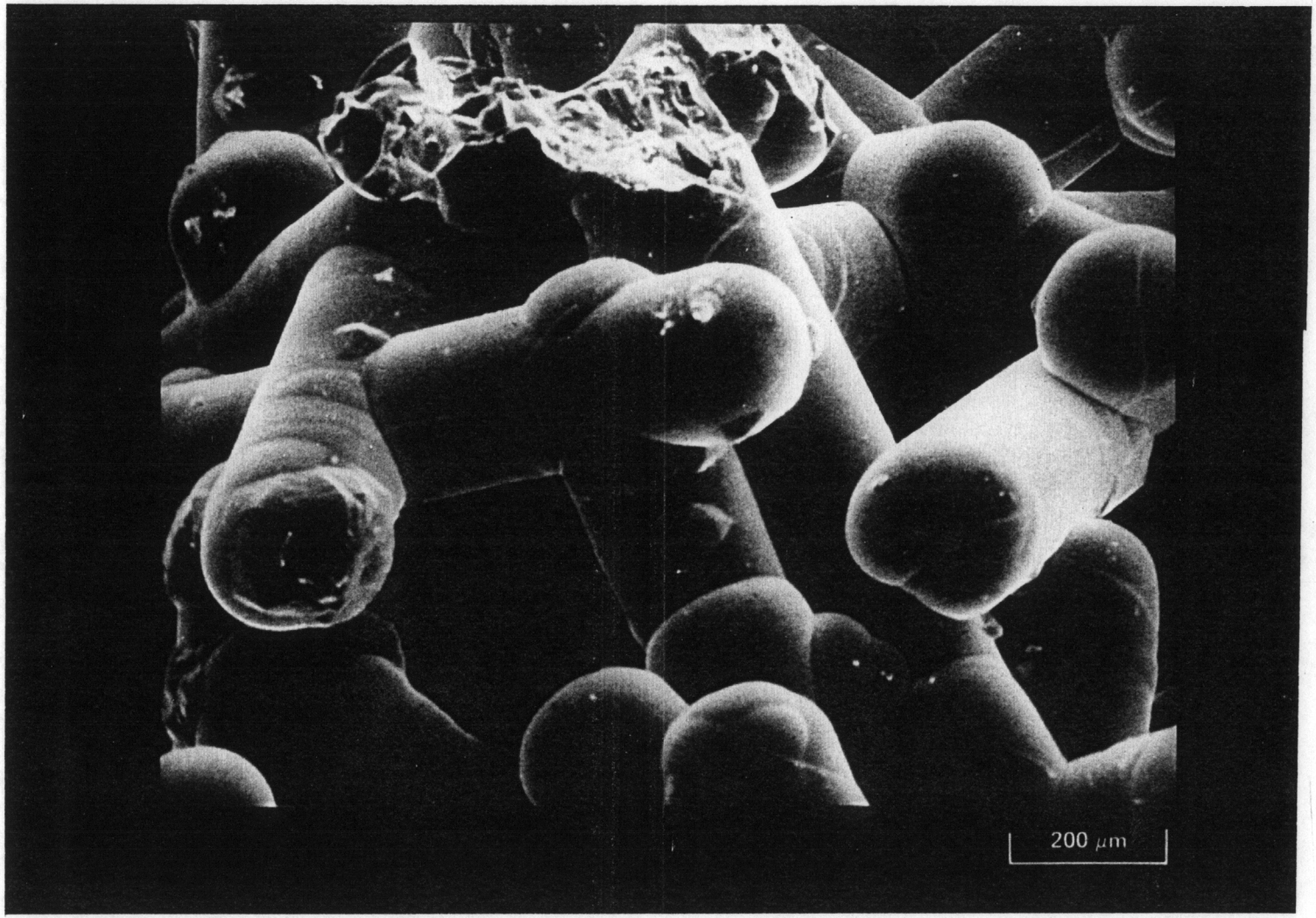

Figure 7. Scanning Electron Micrograph of Si_3N_4 Deposited on SiC Fibers at Hot Face[35]

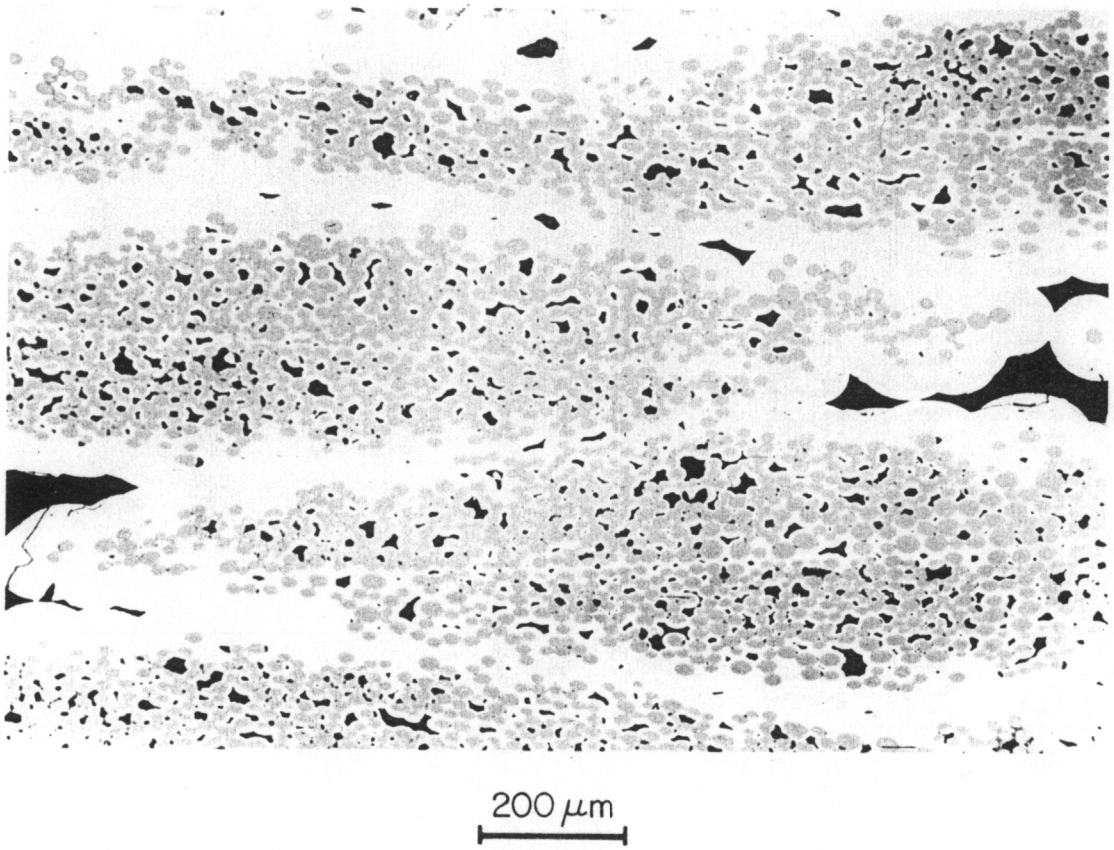

Figure 8. Scanning Electron Micrograph of Cross Section of Composite Producd by CVI[35]

2.5 CVD of Two-Phase Coatings

Traditionally, CVD coatings have been applied on a substrate for surface modification. The deposition of more than one phase has generally been limited to the sequential deposition of mulilayered coatings, for electronic devices, thermal expansion matching, or oxidation/emissivity coatings. The co-deposition of two or more phases simultaneously has not been widely reported. However, with increasing material performance demands, composite structures that can exhibit a number of beneficial characteristics not readily available in single-phase materials are gaining wider interest.

As far back as 1947, Campbell[37] stated that it should be "possible to obtain not only pure metals and compounds" by CVD, "but mixed coatings as well." The deposition of multiphase metal alloys have been reported[38-40]. One of the earliest reported examples of the co-deposition of ceramic materials was C + SiC coatings for nuclear fuel particles for increased strength compared to the pure carbon used previously. Blocher[41], Kaae and Gulden[42], and Atkins and Bokros[43] studied the deposit structures along with hardness and flexural strength of these structures.

Hirai and co-workers in Japan[44-48] and Nickl[49] have studied the deposition of Si_3N_4-matrix coatings with TiN, C, BN, and SiC second phases. The second phase tended to be very small (nanometer scale) in size, with a

spherical, layered, or fibrous morphology. They describe the formation of a platelet-shaped ternary compound, Ti_3SiC_2, during deposition in the Ti-Si-C system. They also reported conditions favorable for depositing amorphous single-phase coatings could be used to produce crystalline structures with a variety of surface morphologies. Zirinski and Irene[50] investigated the co-deposition of Si_3N_4 with AlN.

Nickl and Schweitzer[51] studied deposition in the Ti-Si-C and Ti-Ge-C systems. They obtained a number of multiphase coatings, including SiC + TiC, SiC + TiC + C, Ti_3SiC_2 + SiC + TiC, and Ti_3SiC_2 + $TiSi_2$. They also reported that the ternary phase had a lamellar structure when deposited with a binary phase. Similar phenomena was observed in the Ti-Ge-C system. Most multiphase deposits exhibited unoriented intergrowth of the phases or large crystalline aggregates.

Lackey and Stinton[52] also investigated coatings in the Ti-Si-C system. They found that temperatures above 1325°C were needed to deposit a two phase SiC + $TiSi_2$ coating, with single phase SiC depositing at lower temperatures. These composite coatings exhibited greater adherence and higher fracture toughness than SiC. The microstructure was affected by the hydrogen concentration (with uniformity increasing with increasing H_2 content) and coating process (the use of a fluidized bed reactor was found to result in smaller, more equiaxed particles, while a standard reactor produced

a coating with columnar grains). Lackey[53] also investigated BN + AlN coatings, producing turbostratic or amorphous BN with AlN whiskers and BN particles deposited as the second phase. Besmann[54-55] reported thermochemical equilibrium assessments of reaction in the B-C-N and Si-B-N systems. (Deposition experiments in these systems were not successful, resulting in amorphous coatings that showed no evidence of a two-phase structure.[56])

Lowden[57] studied the addition of the chlorides of Ti, Cr, and Mo to CH_3SiCl_3 precursors during the deposition of SiC. His results agreed with those of Hirai and Nickl, showing that the addition of the second phase significantly altered the surface morphology. The single-phase coating has a smooth nodular surface, while the second-phase addition produced a highly textured, faceted surface, with alternating plates of SiC and Ti_3SiC_2. The Cr and Mo additions were found to have little influence on the surface morphology, with Mo producing <200nm Mo_4Si_3C grains and Cr producing slightly larger $CrSi_2$ dispersoids.

In materials systems more closely related to the present investigation, Golda and Gallois[58] researched CVD in the Si-B-C system, while Lackey studied CVD in the Hf-Si-C-B system. Golda and Gallois used thermochemical modeling to predict deposition behavior, and produced a number of multiphase deposits, including SiC + SiB_6, B + B_4C + SiB_6, SiC

+ SiB_6 + SiB_{14}, Si + SiC + SiB_6, and SiC + SiB_6 + B_4C. The morphologies included acicular and spherical dispersoids. Lackey[59-60] modeled the depostion behavior to try to determine what processing conditions could be used to produce the oxidation-resistant HfB_2 + SiC coating. He reported a small region in the corner of the $HfCl_4$-BCl_3-MTS (methyltrichlorosilane) diagram that indicated that such deposits should be possible. The production of two-phase coatings have not been reported for this system. (Since the experimental results are not known, it is theorized that the processing conditions favorable for producing carbide and boride coatings might tend to be different, so kinetic factors could cause the deposition of HfC instead of HfB_2.)

There have been no reports of the co-deposition of any boride/boride materials. Investigations, thermochemical or experimental, of reactions in the Hf-Si-B-Cl-H are not available in the literature.

2.6 CVD of HfB_2 and SiB_4

As far back as 1931, Moers[61] formed the carbides, nitrides, and borides of a variety of refractory metals by the hydrogen reduction of the metal halides with ammonia, toluene, and boron tribromide. The deposition of silicon borides and HfB_2 was reported as early as 1949 by Campbell. Silicon boride has also been studied by a number of researchers using different reactants and deposition techniques. McCandless[62] patented the production of silicon boride monofiliments by deposition onto a thin, hot wire. Armas[63-64] studied the thermal decomposition of $SiBr_4$ and BBr_3 to produce the high-boron phase, SiB_{14}. Goto[65], Golda[58], and Dirkx[66] have deposited SiB_6 by CVD.

Motozima[67] prepared SiB_4 whiskers on quartz substrates at 1000-1100°C using BCl_3, $SiCl_4$, H_2 and argon. The BCl_3 was generated by the chlorination of B_4C. The formation of whiskers was found only to take place when gold impurities were introduced on the substrate surface. The SiB_4 whiskers were wooly and curled, 0.5-2 mm in length and 0.1-1.0 μm in diameter. Low flowrates of BCl_3 and SiB_4 (1-10 cm^3/min) at 1 atmosphere total pressure were required to produce this morphology. Secondary branching occurred as temperatures were raised above 1000°C. Etching at temperatures above 1100°C was found to eliminate whisker growth.

Goto, Mukaida, and Hirai produced free-standing SiB_4 and SiB_6 plates

(1mm thick) for electrical property measurements. They used $SiCl_4$, B_2H_6, and H_2 reactants for the deposition, at temperatures from 1323-1773K (in a cold-wall reactor), and pressures in the range 30-300 Torr. SiB_4 was found to deposit at lower pressures at temperatures in the range 1400-1573K. Higher pressures and higher temperatures led to the deposition of elemental silicon and SiB_6 respectively.

Dirkx and Spear[68] investigated the thermochemical behavior of reactions (reported in Section 3.1.2) as well as the deposition behavior from SiH_4 and BCl_3 precursors. The effects of temperature, pressure, B:Si ratio, and carrier gas (H_2 or argon) on the as-deposited surface morphologies were investigated. Nodular morphologies were deposited at lower temperatures, lower pressures, lower B:Si ratios, and excess H_2, while the crystallites became more faceted at higher values.

HfB_2 has been deposited using CVD techniques by a number of researchers, Gebhardt and Cree[69], Shinavski and Diefendorf[70], Sheehan[71], and Lowden[72] have studied the deposition and infiltration of HfB_2. Gebhardt and Cree heated $HfCl_4$ (94% purity) at low pressures to produce the $HfCl_4$ source vapor, and found that excess H_2 and $HfCl_4$ reduced the presence of uncombined (free) boron in the deposit. Shinavski and Diefendorf produced $HfCl_4$ by the in-situ chlorination of hafnium chips at 350°C. They found that at high temperatures, the deposition reaction was mass transport limited. At

lower temperatures, an Arrhenius plot showed that the activation energy of the deposition was 97 kcal/mole, and that the transition temperature between control mechanisms changes with excess hydrogen concentration. Sheehan and Lowden have deposited HfB_2 onto carbon fibers as a matrix material to produce high-temperature composite structures.

CHAPTER 3. RESULTS AND DISCUSSION

3.1 Thermodynamic Modeling of CVD Reactions

3.1.1 Thermodynamic Modeling of CVD Reactions in the Zr-Si-B-H-Cl System

Thermodynamic modeling of CVD reactions is a common tool for understanding the differences between different chemical systems. The purposes of modeling each system are twofold. First, the modeling can be used to predict what solid, liquid, and gaseous reaction products are likely to occur at given input conditions, among all possible reaction paths, as a result of having the lowest total Gibbs free energy. Secondly, when an array of conditions are examined, the output can be presented to show the conditions most favorable for the production of desired reaction products. In the present study, the computer program SOLGASMIX was used as a tool to predict the equilibrium reaction species for future comparison to experimental findings in the Hf-Si-B-Cl-H system. (It is expected that since CVD is a steady state, not equilibrium process, the correlation would not be perfect, owing to flow and kinetic considerations.) Additionally, from an applications point of view, since the two phase ZrB_2-SiB_4 is a desirable coating material for its potentially high oxidation resistance, it is important to know the feasibility of producing it, or at least give a good starting point for initial experiments of the deposition of this two-phase material.

The SOLGASMIX program was used to perform the thermodynamic

modeling of chemical vapor deposition (CVD) reactions in the system Zr-Si-B-Cl-H system. In this study, the source gases for the reactions were $SiCl_4$, $ZrCl_4$, BCl_3 and H_2. Table III shows the enthalpy and entropy of formation at standard temperature and pressure[73-75] for all 30 gaseous and 18 condensed phases used in this analysis. (It should be noted that this thermodynamic data lists the lower boride phase as a triboride, SiB_3, while in fact this phase is generally accepted as a tetraboride, SiB_4. A range of stoichiometries have been reported for this phase. In this paper, the thermodynamic modeling section will refer to this phase as SiB_3 to agree with the literature values for this material, but in the rest of the document, it will be referred to as SiB_4.) The temperature dependence of the heat capacity of each specie is represented in the database as up to a fourth order polynomial.

Table 3. Thermodynamic Properties of Gaseous Species

	ΔH° (kJ/mol)	ΔS° (J/mol)
B	560	153.43
BCl	141.419	213.24
BCl_2	272.67	-79.5
BCl_3	-403.0	290.17
BH	442.7	171.85
BH_3	201.0	180.19
BH_3	106.7	187.88
B_2	829.7	202.07
Cl	121.3	165.19
Cl_2	0	223.08
H	218.8	114.72
H_2	0	0.033
HCl	-92.312	186.9
Zr	610.03	183.03
ZrCl	205.43	254.5
$ZrCl_2$	-186.19	292.57
$ZrCl_3$	-524.25	339.01
$ZrCl_4$	-869.98	367.72
Si	450.0	167.98
Si_2	589.94	192.13
Si_3	635.97	211.44
SiCl	198.32	237.83
$SiCl_2$	-168.62	281.33
$SiCl_3$	-390.37	-318.19
$SiCl_4$	-662.75	330.95
SiH	376.66	198.04
$SiHCl_3$	-496.22	313.72
SiH_2Cl_2	-320.49	286.73
SiH_3Cl	-141.84	250.76
SiH_4	34.31	204.65

Table 4. Thermodynamic Properties of Condensed Species Used in SOLGASMIX Calculations

	ΔH° (kJ/mol)	ΔS° (J/mol)
B	0	5.83
B (liq)	26.55	48.93
Zr (A)	0	38.87
Zr (B)	27.87	79.48
Zr (liq)	79.76	108.7
$ZrCl_2$	-430.95	110.04
$ZrCl_2$ (liq)	-411.60	-139.01
$ZrCl_3$	-714.21	145.6
$ZrCl_4$	-979.81	181.42
ZrB_2	-322.6	35.94
Si	0	18.82
Si (liq)	86.19	91.57
SiZr	-154.81	58.16
$SiZr_2$	-208.37	100.42
Si_2Zr	-159.41	71.54
Si_2Zr_5	-575.7	263.174
SiB_6	-59.78	-10.0
SiB_4	-54.76	-14.47

Because of the far more complete thermodynamic database of zirconium containing compounds, it was decided to model the Zr-Si-B system in place of the desired Hf-Si-B system. (There was no data available for the hafnium silicides, and the data on the hafnium chlorides was not consistent.) It is considered common practice to model a closely related system, and since zirconium and hafnium are Group IVB metals possessing similar thermodynamic and chemical properties (as shown in Table IV), this

substitution was considered to be very good. (For these elements, the densities and transition temperatures are the only properties that differ significantly.)

Table 5. Chemical Properties of Hf and Zr[76]

	Hafnium	Zirconium
Metal radius (pm)	71	72
ΔH_{fus} (kJ/mol)	571	567
ΔH_{vap} (kJ/mol)	611	612

After expanding the database to include all necessary species, the deposition parameters of temperature, pressure, gas composition, and excess hydrogen ratio were chosen to model a wide variety of possible reaction conditions. For all gas compositions, three temperatures (1100, 1300, 1500 K), three pressures (1, 0.1, 0.02 atmospheres) and three hydrogen ratios (10:1, 25:1, and 50:1 H: (B+ Cl + Zr +Si)) were investigated. Reactant concentrations were chosen such that the fractions of BCl_3 + $ZrCl_4$ + $SiCl_4$ could be plotted as a ternary phase diagrams i.e. the sum of the concentrations was a constant. (These plots of computed phase boundaries, which indicate gas compositional regions under which specific condensed phases are the equilibrium products, are the graphical representation of the raw output.)

An example of the output of the SOLGASMIX calculations is shown in

Figure 9. The input conditions are T = 1100K, P = 10^{-1} atm. (76 Torr), and a gas composition of 10 moles B, 40 moles Zr, 4 moles Si, 206 moles Cl, and 6500 moles H (giving 10 moles of BCl_3, 40 moles of $ZrCl_4$, and 4 moles of $SiCl_4$ with a H: Reactant ratio of 25:1) The output shows the partial pressure of each gaseous species, represented in Column Y, indicating that unreacted BCl_3, H_2, $SiCl_4$, and $ZrCl_4$, as well as reaction products HCl, $SiHCl_3$, and SiH_3Cl, are the equilibrium gases of significant partial pressure, and that ZrB_2 is the only stable condensed phase.

The raw data, as shown in Figure 9, was compiled and graphically represented by plotting the output at ternary deposition diagrams, also commonly termed "CVD phase diagrams" (not to be confused with true equilibrium phase diagrams). The 27 ternary CVD deposition diagrams generated for this study are the culmination of over 5000 data points. Each of the 27 diagrams show the stable solid reaction products at a particular temperature, pressure, and hydrogen ratio. The diagrams are to be read such that the corners of the diagrams represent the three pure reactant end members (BCl_3, $ZrCl_4$, $SiCl_4$). At the given reaction conditions of temperature, pressure and hydrogen ratio shown at the corner of each diagram, the combination of the reactants at any given concentration would result in the solid reaction product shown on the diagram. An example diagram is shown in Figure 10. In this diagram, it is seen that ZrB_2 is stable

T = 1100.00 K
P = 1.000E-02 ATM

	X*/MOLE	Y/MOLE	P/ATM	ACTIVITY
B	0.10000E+02	0.92619E-16	0.27922E-21	0.27922E-21
BCL	0.00000E+00	0.26757E-06	0.80663E-12	0.80663E-12
BCL2	0.00000E+00	0.42990E-06	0.12960E-11	0.12960E-11
BCL3	0.00000E+00	0.34529E-03	0.10409E-08	0.10409E-08
BH	0.00000E+00	0.81761E-14	0.24648E-19	0.24648E-19
BH2	0.00000E+00	0.18709E-06	0.56401E-12	0.56401E-12
BH3	0.00000E+00	0.23277E-06	0.70173E-12	0.70173E-12
B2	0.00000E+00	0.35849E-29	0.10807E-34	0.10807E-34
CL	0.20600E+03	0.13414E-04	0.40437E-10	0.40437E-10
CL2	0.00000E+00	0.23812E-09	0.71784E-15	0.71784E-15
H	0.65000E+04	0.83966E-03	0.25313E-08	0.25313E-08
HCL	0.00000E+00	0.57395E+02	0.17303E-03	0.17303E-03
H2	0.00000E+00	0.32210E+04	0.97101E-02	0.97101E-02
SI	0.40000E+01	0.73130E-08	0.22046E-13	0.22046E-13
SICL	0.00000E+00	0.10425E-05	0.31427E-11	0.31427E-11
SICL2	0.00000E+00	0.21015E+01	0.63353E-05	0.63353E-05
SICL3	0.00000E+00	0.32348E+00	0.97520E-06	0.97520E-06
SICL4	0.00000E+00	0.69302E+00	0.20892E-05	0.20892E-05
SIH	0.00000E+00	0.23421E-07	0.70607E-13	0.70607E-13
SIHCL3	0.00000E+00	0.57458E+00	0.17322E-05	0.17322E-05
SIH2CL2	0.00000E+00	0.57101E-01	0.17214E-06	0.17214E-06
SIH3CL	0.00000E-00	0.15044E-02	0.45352E-08	0.45352E-08
SIH4	0.00000E+00	0.16974E-04	0.51171E-10	0.51171E-10
SI2	0.00000E+00	0.19894E-12	0.59973E-18	0.59973E-18
SI3	0.00000E+00	0.11276E-13	0.33992E-19	0.33992E-19
ZR	0.40000E+02	0.65331E-25	0.19695E-30	0.19695E-30
ZRCL2	0.00000E+00	0.37044E-08	0.11168E-13	0.11168E-13
ZRCL3	0.00000E+00	0.11819E+01	0.35630E-05	0.35630E-05
ZRCL4	0.00000E+00	0.33818E+02	0.10195E-03	0.10195E-03
ZRCL	0.00000E+00	0.16862E-15	0.50833E-21	0.50833E-21

INVARIANT COMPOUNDS

B(S)	0.00000E+00	0.00000E+00
B(L)	0.00000E+00	0.00000E+00
SI(S)	0.00000E+00	0.24880E+00
SI(L)	0.00000E+00	0.00000E+00
ZR(A)	0.00000E+00	0.00000E+00
ZR(B)	0.00000E+00	0.00000E+00
ZR(L)	0.00000E+00	0.00000E+00
SIZR(S)	0.00000E+00	0.00000E+00
SIZR2(S)	0.00000E+00	0.00000E+00
SI2ZR(S)	0.00000E+00	0.00000E+00
SI3ZR5(S	0.00000E+00	0.00000E+00
ZRCL3(S)	0.00000E+00	0.00000E+00
ZRCL4(S)	0.00000E+00	0.00000E+00
ZRCL2(S)	0.00000E+00	0.00000E+00
ZRCL2(L)	0.00000E+00	0.00000E+00
ZRB2(S)	0.00000E+00	0.49998E+01
SIB6(S)	0.00000E+00	0.00000E+00
SIB3(S)	0.00000E+00	0.00000E+00

Figure 9. Output from SOLGASMIX Computer Program at 1100K and 0.01 atm.

TERNARY CVD PHASE DIAGRAM (1300K, 1 ATM, 10:1 H/(Zr+Si+B+Cl))

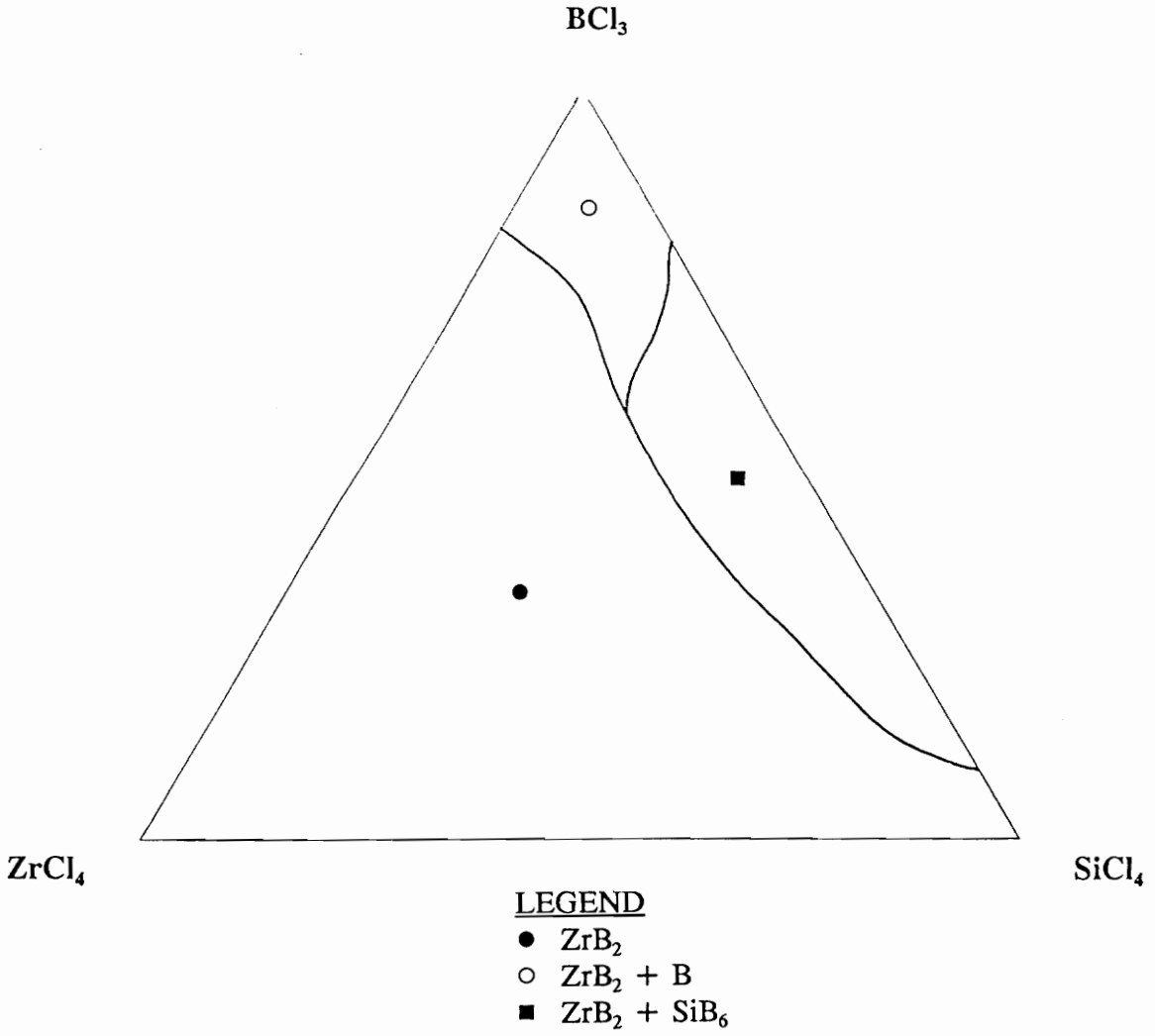

Figure 10. Ternary CVD Phase Diagram at P = 1 atm., T = 1300K, and H/(Zr + Si + B + Cl) = 10

over the entire range of gas input concentrations, with metallic boron codepositing at low $ZrCl_4$ and $SiCl_4$ concentrations. The codeposition of ZrB_2 and SiB_6 is favored at low $ZrCl_4$ concentrations over a wide range of Si:B ratios. (The other 26 ternary diagrams are shown in Appendix A.)

Overall, the ternary diagrams show that the two phase ZrB_2-SiB_6 region is stable at almost all conditions of temperature, pressure, and hydrogen ratios investigated (at $ZrCl_4$ concentrations below 15%). In every case, ZrB_2 is an extremely stable phase, forming under all conditions that $ZrCl_4$ and BCl_3 are input species. There are no input conditions that included the presence of boron in the gas phase that showed any zirconium silicide phase to be stable. Apparently, the very negative free energy of formation of the ZrB_2 makes the formation of the silicide unfavorable. SiB_6 is the preferred silicon boride at lower temperatures and hydrogen concentrations, with SiB_3 deposition favored at higher temperatures and hydrogen concentrations. Metallic zirconium is not predicted to deposit under any deposition conditions. The output data can also be graphically presented as "pseudo-binary" diagrams, with $ZrCl_4$ concentrations held constant at 5%, showing the relatively high degree of stability of the ZrB_2-SiB_6 and ZrB_2-SiB_3 phase fields as a function of temperature and $SiCl_4$ concentration, as shown in Figure 11. These diagrams make it easier to follow the trends of deposition products at varying pressures and hydrogen ratios.

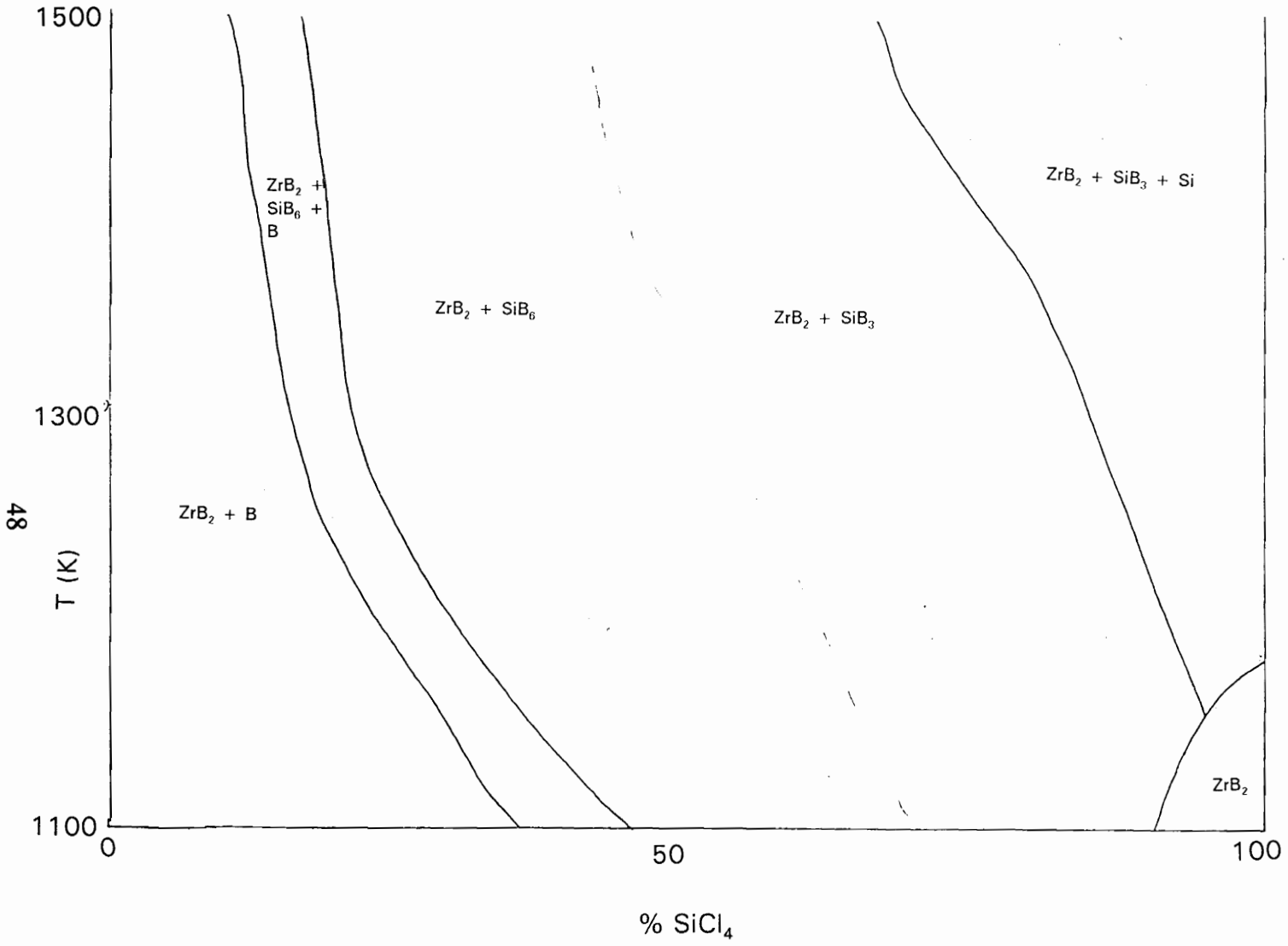

Figure 11. Binary CVD Phase Diagram at $X_{ZrCl4} = 5\%$

3.1.2 DISCUSSION OF THERMODYNAMIC MODELING RESULTS

The discussion of the results of the thermodynamic modeling will cover three areas: a review of the calculation techniques used for thermodynamic modeling, a discussion of the results of the present investigation, and an analysis of the role of thermodynamics in CVD processes.

A. Calculation Technique used in Modeling

Thermodynamic modeling calculations require a knowledge of chemical compositions and solution behavior of all possible gaseous and condensed phases that can exist over the entire temperature, pressure, and compositional ranges of interest. The input data for these calculations, taken from tabulated compendiums or published articles on specific systems, have either been measured[77], predicted, or calculated by a number of researchers, and are subject to review and revision by subsequent scientists. The largest errors in thermodynamic modeling often involve inaccurate input data or the omission of important phases or species. For example, the uncertainty in the dissociation energies of some species can lead to an order of magnitude error in the partial pressures predicted for major species. Bloem[78] has described that omitting certain sub-chloride species can yield inaccurate results because of the etching reactions that are important at high temperatures.

A number of methods have been reported for carrying out these computations, but all are based on the methods of Brinkley[79] or White[80]. Brinkley's method requires the writing of a series of chemical reactions and the computation of their respective equilibrium constants and, ultimately, the equilibrium composition. This technique, however, proves unwieldy when calculating the equilibrium state of complex systems, because hand computations make it difficult to consider all possible reaction pathways. White's slightly different approach involves the minimization of the summation of the free energies of all possible species. Eriksson[81-82] developed a computer program, based on White's technique, called SOLGAS (which he later upgraded to include non-ideal solids in SOLGASMIX) to perform the calculations for complex systems containing more than one condensed phase.

In this program, the free energy of the system represented by the relation

$$\left(\frac{G}{RT}\right) = \sum n_i \left[\left(\frac{g^o}{RT}\right)_i + \ln a_i\right]$$

is minimized with respect to n_i for constant pressure and temperature values, with mass balance constraints (n_i cannot be negative). In this equation, **G** is the total system free energy, **R** the gas constant, **T** the temperature, **g°** the

standard chemical potential, **a** the activity, and $\mathbf{n}_i$ the amount of the ith substance. (The basic equations used in SOLGASMIX are given explicitly in Reference 82.) Lagrange's method of undetermined multipliers is used for determining the constrained minimum, and the logarithmic equations obtained are expanded in a Taylor's series about initially estimated (or manually inputted) n_i values. With the linear equations representing approximations of the exact expressions, the equilibrium amounts are thus obtained by a series of iterations[81]. The program can consider all conceivable gaseous and condensed phases in one calculation, preventing the omission of an important specie. (A computer program is only as good as its programmer, so, as mentioned previously a complete database is necessary for meaningful results.) These chemical equilibrium calculations involve the computation of the system chemical composition, and are subjected to the constraints of elemental composition, constant temperature, and constant total pressure. The conservation of mass is also obeyed, with the rate of input of each element being equal to the exit rate of that element in the product gases plus any of that element in the deposition products. An additional constraint requires that the flow rate to any given region of the substrate is identical to that of any other region. This constraint thus assumes that the diffusion from the bulk gas through the boundary layer is perpendicular to the substrate, such that the concentration gradients will be

between the bulk gas and the substrate and not along the substrate surface.

B. Discussion of Modeling Results

The CVD diagrams generated using the output of the SOLGASMIX[83] calculations (Figure 10 and Appendix A) show that at higher pressures, the desired two-phase regions are stable over a wide range of temperatures and $SiCl_4$ concentrations. Lower pressures and higher hydrogen ratios seem to promote the deposition of metallic boron and silicon, agreeing with the results of Spear[84] and Shinavski[85]. The presence of hydrogen drives the chloride reduction reactions further to the right, as one would expect from LeChatlier's principal. (Metallic silicon and boron are not generally favored under these conditions, with the deposition reaction being reversible. The chloride species can preferentially react with the metal to form a different chloride species. This is why, in silicon epitaxy and polycrystalline depositions, silane is used at high temperatures and the chloride at lower deposition temperatures.) From the present study, one atmosphere pressure seems to allow the greatest latitude in temperature and reactant concentration for the preparation of ZrB_2-SiB_4 composite coatings. It is important to note, however, that there is at least some well defined region of thermodynamic stability for the deposition of this two phase material under almost all reaction conditions tested. This window of possible deposition conditions will allow for not only the control of two phase composition, but

also for the manipulation of the coating microstructure (since microstructure is highly sensitive to deposition conditions). This should allow for the tailoring of coating composition and microstructure to optimize the oxidation properties.

The results of this modeling study agree with the results of Spear and Dirkx[86,87] on the deposition of the silicon borides. They looked at reactions from 1000-1800K, 0.0263 atm, and flowrates of 30 sccm (standard cubic centimeters/min) for BCl_3, 10 sccm for SiH_4 (as opposed to the $SiCl_4$ used in the present study) and 1000 sccm of H_2. Their results seem to indicated, as does this study, that SiB_6 is the preferred deposition product at lower temperatures and hydrogen concentrations, but that SiB_3 becomes more stable at higher temperatures and hydrogen concentrations. They speculate that one reason for this is the hydrogen reduction of the silicon chlorides is more favorable at higher temperatures promoting the deposition of the more silicon-rich phase.

For this study, it was desired to determine which deposition products could be expected under a variety of reaction conditions. This information will be used to guide the experiments, helping decide what conditions are likely to lead to the co-deposition of HfB_2 and SiB_4. The partial pressure data that was generated, while very interesting, is not central to the focus of this study. A more basic understanding of the deposition process for this system

would require the diagnostic tools described previously. (The high partial pressures of a gas indicated that it is either an unreacted input specie or that it is a stable product of a disproportionation of an input gas or a product of the deposition reaction. In general, a higher partial pressure indicates an importance to the deposition process.) The high pressures of HCl indicates that it and the chlorosilanes are important in the deposition of both boride phases. (Similarly, Besmann[88-89] showed that the low stability of H_2SiCl_2 and its decomposition into silicon chlorides proved the importance of the chlorides versus chlorosilanes in the deposition reaction of Si_3N_4). The partial pressure data generated by SOLGASMIX can be used to determine the theoretical thermochemical deposition efficiency of the reaction. This quantity is defined as the fraction of reactants forming the product phase at equilibrium compared to the maximum that would form based solely on input quantities; i.e. the fraction of reactive gases that are converted to a condensed phase. Determining the efficiency of the deposition involves the calculation of the equilibrium constant, K,for the reaction (under each set of deposition conditions) using the relation

$$K = \frac{p_{products}}{p_{reactants}}$$

Since the equilibrium constant for the reaction at a given temperature is

defined as

$$K = \exp\left(\frac{-\Delta G}{RT}\right)$$

the ratio of these quantities at various pressures and gas fractions can indicate which processing conditions are the most favorable (highest efficiency) for the deposition of a certain phase and can indicate if the deposition process is practical[89].

C. The Role of Thermodynamics in CVD

Chemical vapor deposition, as defined previously, is a processing technique that utilizes chemical reactions from gaseous precursors to produce a condensed phase upon a substrate, plus gaseous reaction products. A CVD process can be described in terms of the system chemistry (thermodynamics and kinetics), mass transport (gaseous diffusion and forced convection), and gas flow behavior (flow patterns and velocities). A CVD process is very complex, owing to a network of relationships between and among controllable experimental parameters (reactor geometry, substrate temperature, input gas composition, total flow rates, total pressure, substrate surface preparation), process variables (flow behavior, gas homogeneity, high-temperature gas chemistry, nucleation density, deposition rate) and coating properties (morphology, composition, thickness, adherence, uniformity, crystallinity, stress state).

While experimental parameters can be varied in a trial and error fashion, sometimes with good results (depending on operator experience), modeling the deposition process can predict **a priori** the effect of controllable parameters on the deposition product. A complete modeling of each set of deposition reactions would require an understanding of the influence of the experimental parameters on the process variables, and the resultant influence on coating properties. Each CVD system has its own behavior, but some general rules of thumb about the deposition process can be stated without knowledge of the chemistry of the specific system. Spear[87] discusses these interrelationships in detail.

The deposition process can be described by a model developed by Spear[84]. As illustrated in Figure 12, seven sequential steps describe the mechanisms of the deposition in terms of local gas chemistry in a portion of the system. It is assumed that steady state conditions exist, i.e the properties of the systems at a given location are independent of time. It is also assumed that no chemical reactions among the gases in the bulk or boundary layer; all reactions take place at the substrate surface. Temperature and pressure are taken to be constant, and the law of the conservation of mass is also obeyed such that the amount of any element in the system either is deposited onto the substrate as a condensed phase or it

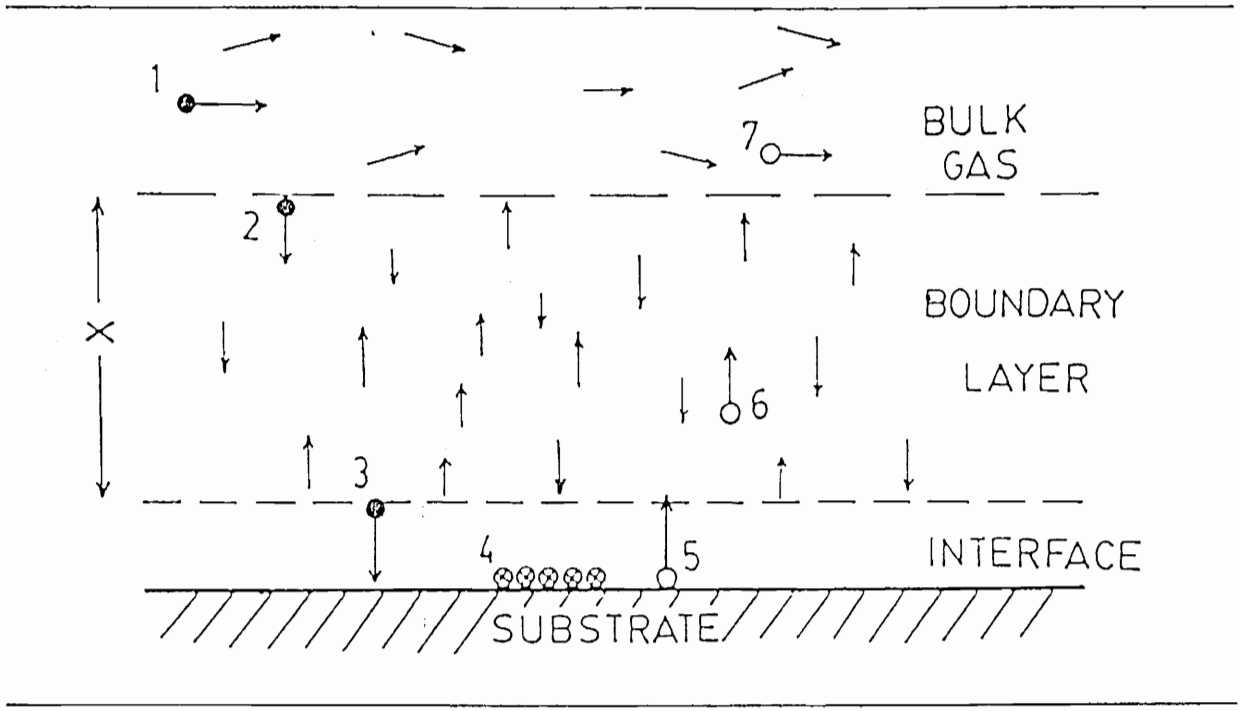

Figure 12. Schematic Diagram Illustrating Sequentially-Linked Steps in a CVD Process[73]

exits the system as a gaseous specie. The first and seventh steps represent the forced flow and exit of gases in the system. The second and sixth steps are the respective diffusion/bulk viscous flow of the reactants and product gases into and out of the gaseous concentration boundary layer to/from the substrate. Complete mixing is assumed in the homogeneous bulk gas, while the gas in the boundary layer is assumed to mix by diffusion (perpendicular to the substrate). The thickness of this boundary layer is determined by the flow behavior. The third and fifth steps are the adsorption/desorption of species at the substrate surface. The fourth step is the deposition reaction and other surface chemical processes.

While the overall CVD process is fairly well understood, the knowledge of each CVD reaction system tends to be more empirical in nature. Each mechanistic step needs to be modeled for each deposition system for a more complete understanding of that system. There has been some work recently incorporating in-situ diagnostics (Raman spectroscopy, mass spectroscopy, gas chromatography, laser diagnostics) to investigate these chemical phenomena[90,91], but much of the work is not in the general literature.

In this section, the importance of thermochemical equilibrium calculations to the modeling of CVD reactions is discussed. The prediction of reaction variables that will produce a desired coating is a very important

tool, because with the complex chemistries present in these systems, trial and error is not a practical method for developing these variables, and the complete modeling of all possible factors affecting the deposition process would be prohibitively complex. Many authors[87,92,93] have illustrated the value of high temperature thermochemical modeling techniques for CVD processes. While thermodynamic calculations will not predict all aspects of the CVD process, the role of thermodynamics in high temperature chemistry is important. Generalizations about the chemistry of reactions at room temperature often do not hold at high temperatures, with reactions not energetically favorable at low temperatures becoming important at high temperatures. Thermodynamic, rather than kinetic, limitations then tend to determine high temperature reactivity. The complexity of a system is increased by the vaporization of condensed species and by the fact that vapor species that do not conform to familiar oxidation states may form[86].

The value of thermochemical modeling of CVD reactions is often questioned, since CVD is a dynamic, nonequilibrium process. The previously defined mechanistic steps are, unlike thermodynamic equilibria, time dependent. Using this argument, equilibrium calculations should not be valid for describing the process. A CVD process will achieve steady state conditions unless there are fluctuations in temperature, total pressure, input gas concentration, or flow rates. Spear[86], however, points out that a "partial

equilibrium" will always be achieved by one or more chemical processes in a CVD system, making thermodynamic modeling quite useful for predicting and explaining the behavior of CVD systems. This type of analysis can provide limiting values for the deposition parameters of a system. For example, when temperatures are high enough for mass transport to be the rate limiting step in a coating process, as described in the kinetics section (3.8.1), the chemical reactions at the substrate surface reach equilibrium. Therefore, these calculations can indicate which species are important in the deposition reaction, and can provide partial pressure information that can be used to determine diffusion rates through the gas flow boundary layer. The difference in the bulk gas composition from the composition of the gas arriving at the substrate surface can be attributed to transport phenomena, adsorption/desorption kinetics, or surface reaction kinetics. Research of the high temperature behavior of each of the seven deposition steps would add to the thermochemical calculations to give a more complete understanding of the deposition process.

As stated previously, equilibrium calculations can provide a powerful tool for modeling CVD reactions. Its primary usefulness lies in the estimation of deposition behavior, predicting what phases are expected to be produced under a variety of reaction conditions. Thermochemical modeling can also prove useful in explaining a number of experimental observations. These

include: a) The maximum rates and efficiencies of deposition; b) The partial pressures of all gaseous species in homogeneous equilibrium before deposition or in heterogeneous equilibrium with the substrate during deposition. The identification of potentially hazardous exhaust gases can be quite important in reactor/scrubber designs.; c) The sensitivity of predictions to changes in experimental parameters (In determining which species are mechanistically important, observed kinetic data is compared to the calculated thermodynamic predictions, with rate limiting reactions thus being identified. The importance of the presence of HCl in many deposition reactions was determined in this manner.); and d) The mechanisms for explaining possible nonequilibrium behavior[86].

An example of the use of thermodynamic calculations in CVD processes is in the growth of single crystal films. According to elementary nucleation theory, a small negative value of ΔG_v (free energy per unit volume) is required to yield a low nucleation rate of critical size nuclei. In order to have a single nucleus from which subsequent growth will occur, the $\Delta G°$ value would need to be close to zero (a small interfacial energy between the film and substrate is also necessary). When this happens, large amounts of products and reactants will be present in the gas mixture. If ΔG_v were too large, the rate of heterogeneous nucleation on the substrate, or even homogeneous nucleation in the gas phase, would be increased. Thus,

for this example, a large driving force for chemical reaction will tend to produce polycrystalline films[31].

3.2 REACTOR DESIGN

3.2.1 Hot-Wall vs. Cold-Wall Systems

There are three basic components of a chemical vapor deposition system: source gas delivery system, pressure control system, and heating source. As discussed previously (Section 2.4), CVD is a processing technique that utilizes thermal energy to activate the deposition reaction. In traditional deposition systems, this energy is supplied by the heated substrate. For the present study, the two basic types of conventional CVD reactors, hot-wall and cold-wall designs, are considered. In a hot-wall system, the substrate is heated to the reaction temperature in a furnace where the surroundings are at the same temperature. A cold-wall system involves the heating of the substrate separately from its surroundings, either through inductive coupling, resistive heating by electrical current, or infrared heating. (Microwave heating is covered in another section, as a separate technique within the broad class of CVD techniques.)

Both types of systems have inherent advantages and disadvantages. In the hot-wall reactor design, all exposed hot surfaces will be coated during the deposition process. This can cause problems if these surfaces are adversely affected by the coating or source gases. This reaction with the furnace walls also causes a depletion of reactants before they reach the substrate surface. This means that the input gas-specie concentrations will

not be the same as the near-substrate surface concentrations. However, this can be compensated for by adjusting initial conditions to tailor the gas chemistry at the substrate surface, or increasing gas velocities downstream by narrowing the flow cross section. Another problem with hot-wall reactors is the possibility of reacting the input gases in the gas phase before they can reach the substrate surface. At sufficiently high gas concentrations and temperatures, the frequency of molecular collisions within the gas phase is great enough to cause homogeneous nucleation and growth of a powder product, as discussed previously. If a powder does form, and precipitates onto the substrate surface, film quality will be adversely affected, causing voids to form which lower the film density and adherence. This phenomenon is taken advantage of commericially, however, for making nanophase powders of very high melting temperatures that can later be compacted to full densities.

Cold-wall reactors allow the input reactant species to reach the substrate without depleting, either by reacting with the reactor walls or homogeneously reacting in the gas phase. This makes this type of system ideal for experimental reactors, where evaluating evolved gas species and near-surface reactions can yield important data and insight into possible intermediate reactions, and depletion will change the gas composition through the hot zone. (Cleanup tends to be difficult with hot-wall reactors,

with deposition products being deposited in the reaction zone. Additionally, since there is no problem with furnace heating/cooling cycles causing reaction tubes to crack, turnaround time is much shorter.) For large scale, industrial coating operations, however, cold-wall systems are impractical for a number of reasons. These include: a) The temperature gradients, or hot spots, that can arise in the substrate from uneven coupling (due to irregular substrate shapes or variations in coil spacing or separation from the substrate) compared to the large hot zones in traditional furnace systems; b) Reaction depletion will still be a problem for large substrate or multiple-sample batches; c) Small cross sections and high resistivity materials are necessary for resistive heating; d) Temperature control is difficult, because the coating being applied changes the electrical properties during deposition, making it a time dependent process; e) If the substrate is non-conductive, coupling in an rf field or direct electrical resistance heating is not possible, the use of a conductive substrate holder or large graphite susceptor will be necessary; and f) Infrared heating is not capable of producing high substrate temperatures.

3.2.2 Reactor Design

For the present research, a hot-wall reactor design was chosen for its suitability for scale-up or transition into chemical vapor infiltration (CVI) systems. (A lack of available induction furnaces at NSWC also contributed to this decision.) A CM Series 1700 Horizontal Tube Furnace (with a Eurotherm Type 815 Controller/ Programmer and Kanthal 1800°C $MoSi_2$ heating elements) was used for the basic temperature control system. Mullite tubes (36" long, 2" OD), from Vesuvius McDanel Refractories were used for the reactor chamber. (While it has higher temperature capabilities, the combination of lower thermal shock resistance and higher thermal conductivity of alumina could lead to tube cracking and end-seal degradation.) The large thermal gradient that occurs as the tube emerges from the hot zone has been found to cause cracking after just a few heating cycles, even with additional insulation placed around the tube outside of the furnace shell. While longer heating\cooling cycles and water-cooled end-plates could alleviate some problems with alumina, tube lifespan and safety concerns made mullite a better choice.

The 2" mullite tube is smaller than the furnace shell opening, so alumina refractory brick rings were made to fill the gap and center the tube in the hot zone. The weight of the vacuum end-plates plus that of the protruding (8" at each end) mullite tube has been found to cause fairly large

bending stresses on the tubes in the hot zone, so a support system consisting of two laboratory jacks with refractory brick and alumina fiber insulation were used to support this weight outside the hot zone.

The flat rubber-gasket seals supplied by CM (through McDanel) for vacuum/pressure sealing were found not to be adequate for maintaining a good mechanical vacuum. An ultimate chamber vacuum of 80 mtorr should be possible with this type of pump (with the vapor pressure of the vacuum pump oil being about 5-10 mtorr). To assure a leak-free reactor, the vacuum is tested before each experiment. This is highly important due to toxic and explosive gases used and generated during this process. A new, more reliable end-seal system was designed using a viton o-ring in a stainless steel compression fitting. (The 2" OD Mullite tube was chosen because a 2" ID coupling from Metra, Inc. was the largest available commercially, without having one machined to larger specifications.) The mullite tubes (having been extruded and hung vertically to dry and fire) were found to have different outside diameters at the tube ends, and were out of round. They were machined to tolerance at NSWC by Mr. Al Cade. Before each experiment, the interior surfaces of the mullite were lined with Graphoil® sheets. This helped to reduce exposure of the mullite to the corrosive chlorides, and also served as a sacrificial surface for deposition buildup.

3.2.3The Gas Delivery System

A.Original Design

The initial design for the gas injector system is shown in Figure 13. The concentric injector is comprised of two stainless steel tubes, 1/4" and 1/2" in diameter and 12" long, were welded together at the cold end. The inner injector had holes drilled along its length, and was welded closed at the end closest to the hot zone. This forced the gas from the inner tube into the stream of the outer injector gas, providing good gas mixing. These concentric tubes extended 6" into the mullite tube.

B.Hafnium Chlorinator

A stainless steel pipe (12" long, 1/2" diameter), with a 1/4" tube fitting welded on one end and pipe threads cut into the other (allowing a pipe to tubing adapter to be used as a removable cap for loading/unloading) was used for the $HfCl_4$ generating reactor. The pipe was placed in a Hevi-Duty Inc. Shell Furnace, with a Variac power supply controlling applied voltage and an Omega Type K Thermocouple Thermometer measuring the temperature. Chlorine gas was metered through 1/4" tubing to the heated hafnium sponge. The specific reaction pathways will be discussed in Section 3.7.4. (The difficulty of controlling the sublimation of $HfCl_4$ powder, and its water sensitivity made direct metal chlorination much more desirable.) The $HfCl_4$ gas generated in this pre-reactor was flowed to the concentric injector,

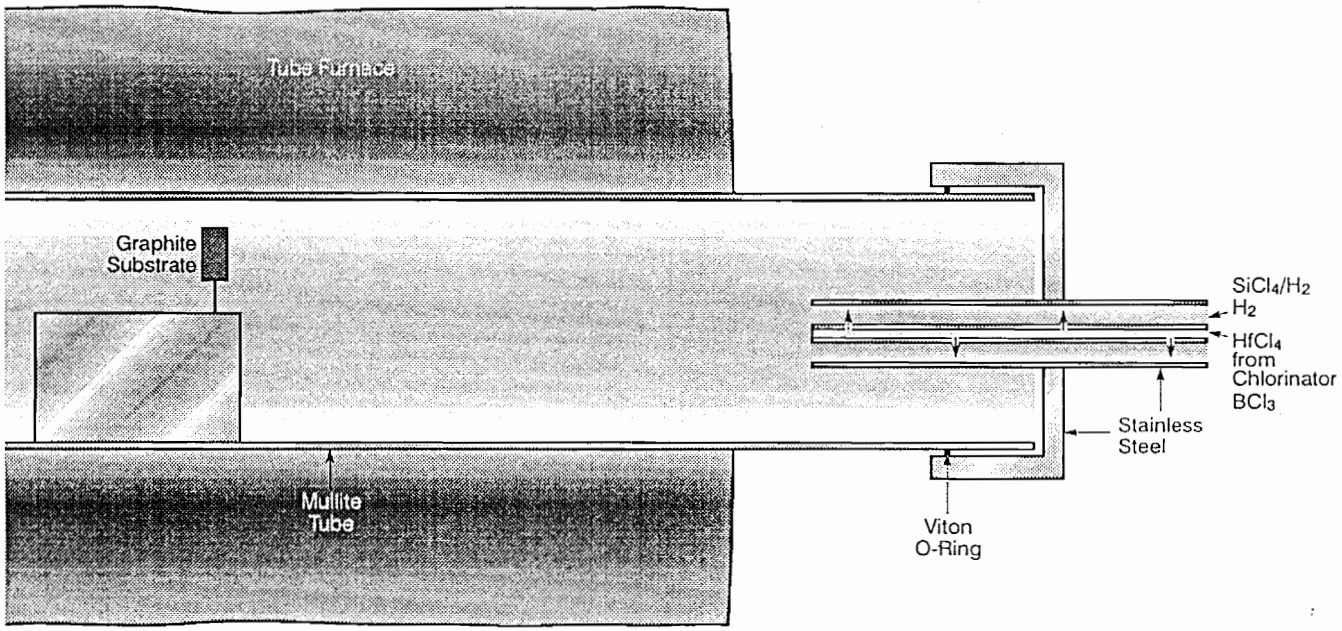

Figure 13. Original Design for the Hot-Wall CVD Reactor

where it was mixed with the BCl_3 at the inner injector port. Heating tape was wrapped around the tubing from pre-reactor to injector to maintain elevated temperatures, because the $HfCl_4$ was previously found to precipitate at lower temperatures.

C. $SiCl_4$ Bubbler

The choice of $SiCl_4$ as the silicon source over SiH_4 was a matter of safety and economics. While SiH_4 is widely available commercially and commonly used in the electronics industry, it is fairly expensive, but most importantly, it is pyrophoric. Unreacted SiH_4 needs to be either re-used, post-reacted, or scrubbed to eliminate explosion hazards. This is especially important in the planned experiments, where excess hydrogen is going to be used. Therefore, $SiCl_4$ was deemed much safer and easier to handle without expensive gas delivery and scrubber systems. While it is corrosive, it can easily be neutralized with a soda-lime scrubber already planned for use with the other chlorides.

$SiCl_4$ is a liquid at room temperature and pressure, and its vapor pressure is sufficiently low to require the use of a bubbler system to carry the vapor to the reactor or direct injector to transfer the liquid to the reactor. As commercially available liquid injectors (available from MKS Instruments or Tylan) cost > $3000, a liquid bubbler system, shown in Figure 14, was designed and constructed. A stainless steel canister (7"h X 6"d, 3000 ml

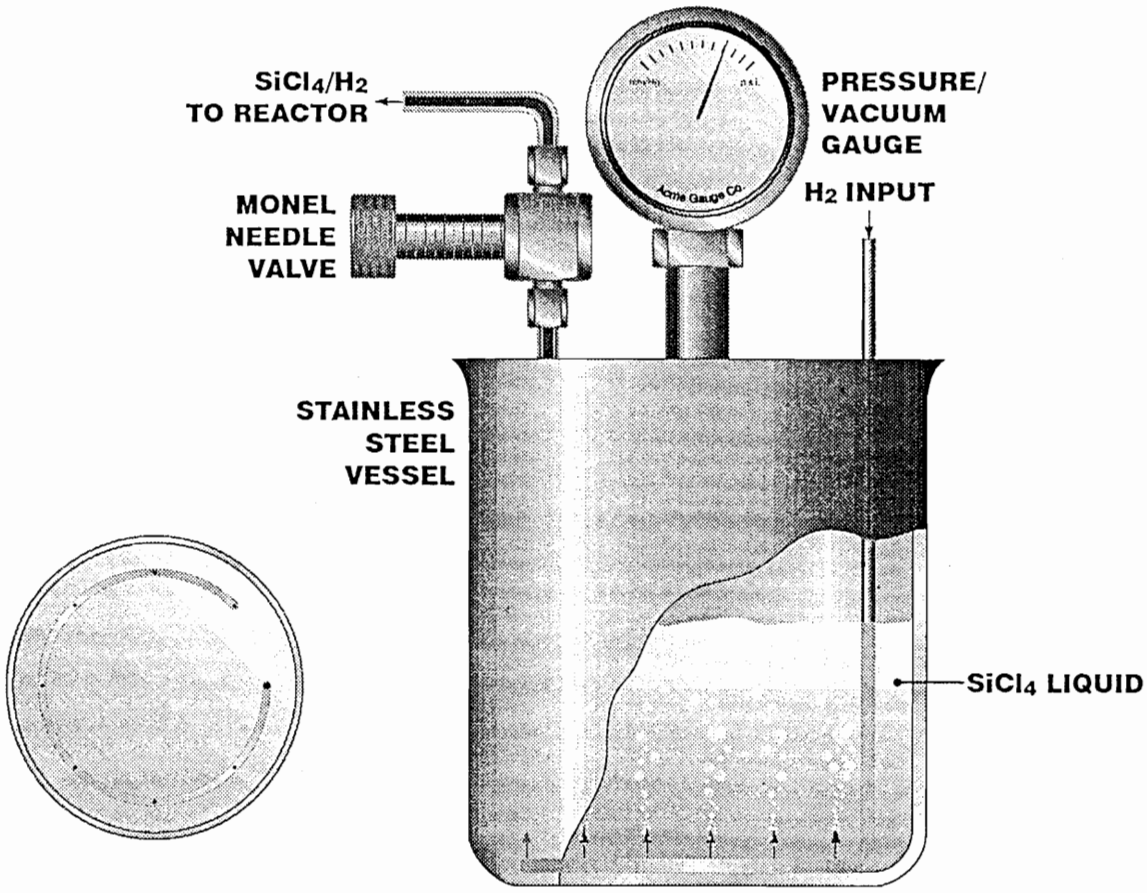

Figure 14. $SiCl_4$ Bubbler

capacity, from Polar Ware Co.) with a stainless steel plate welded at the lip was used for the basic vessel. The three main features of the bubbler are the injector, needle valve, and pressure/vacuum gauge. The injector is a 1/4" s.s. tube, fed to the bottom of the vessel and wound around its inner circumference, as shown in the cross section in Figure 14. With holes drilled along the top surface of the circumferential length and welded at its tip, the injector allows the carrier gas (hydrogen, metered before reaching the injector) to be bubbled through the $SiCl_4$ liquid. The hydrogen gas carries some of the $SiCl_4$ vapor with it through the exit tube to the hot zone. The monel needle valve (Nupro Co.) allows gas to flow through it without the entire vessel contents being exposed to the vacuum (and thus being sucked into the hot zone). The s.s. pressure/vacuum gauge allows the internal pressure of the canister to be monitored and manually adjusted (with the needle valve) to keep the contents at a positive pressure. In this manner, variations in carrier gas flow rates from run to run can be balanced to maintain the same internal pressure in the bubbler. The $SiCl_4/H_2$ mixture was forced to the hot zone through the outer injector, where it was combined with the excess H_2.

$SiCl_4$ Flowrate Calibration

Before the deposition experiments were begun, the amount of $SiCl_4$ carried to the reactor by the H_2 gas was calculated. The $SiCl_4$ bubbler was

weighed before and after each 30 minute run. The total volume of gas removed was calculated using the ideal gas law $PV = nRT$, with $P = 3$ psi for the bubbler, $T = 298K$, $R = 86.02 cm^3$ atm/mole K, n = weight of $SiCl_4$/169.9 g/mole. The results, plotted in Figure 15, show a fairly linear increase in $SiCl_4$ flow with increasing H_2 flow. The higher values (>30 cm^3/min H_2) were more reproducable than the lower flowrates, so these were used in the deposition experiments.

D.Gas Control System Re-design

Initial experiments showed that there are difficulties with using a pre-reactor for $HfCl_4$ generation. At low temperatures, the chloride was found to precipitate from the gas phase, clogging the tube to further gas flow. The chlorinating furnace was thus shelved, and further metal chlorination was conducted in the mullite tube in the CM Furnace. A temperature profile of this tube showed that the desirable chlorinating temperature of 400°C exists where the tube exits the furnace shell (at a hot zone temperature of 1200°C), 10" from the hot zone, or 8" from the tube opening. In this configuration, the chlorine injector is 2" from the hafnium sponge. (This problem with the chlorinating pre-reactor would have been difficult to overcome in a cold-wall reactor, making the hot-wall system necessary for in-situ hafnium chlorination.)

Another set of experiments, however, soon showed that a different

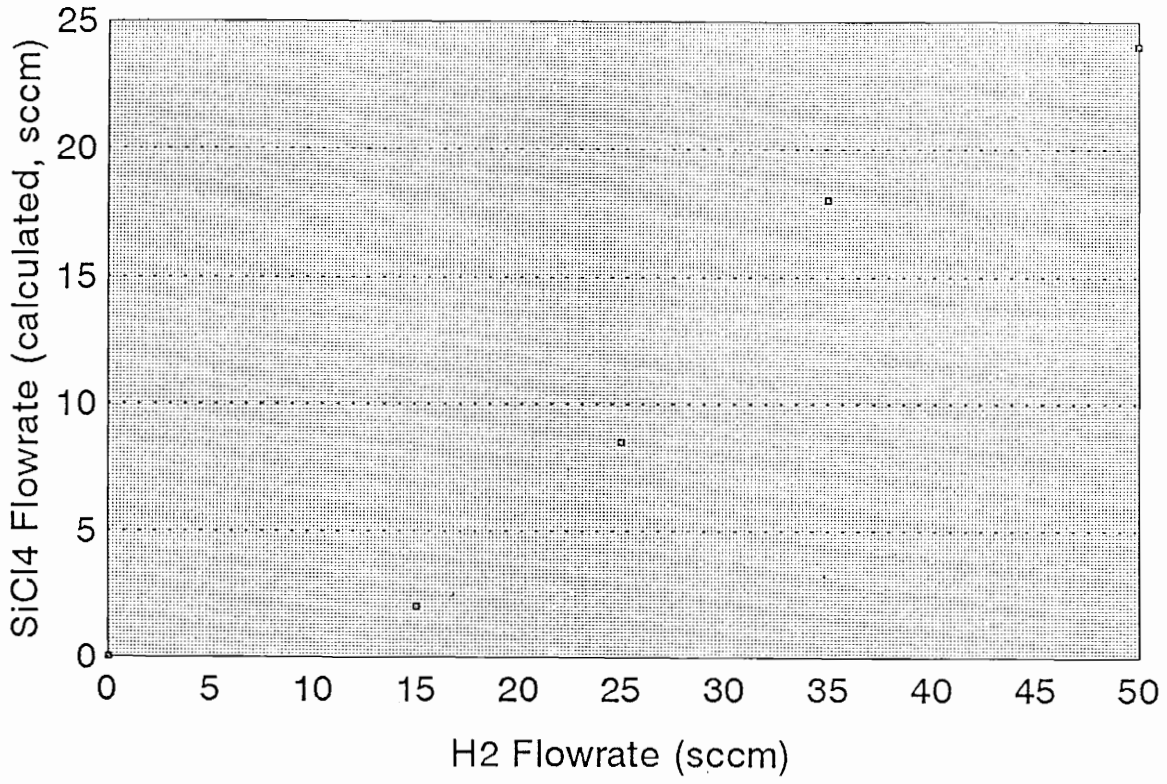

Figure 15. Calibration Curve of $SiCl_4$ Flowrate vs. H_2 Flowrate

precipitation reaction was still interfering with the deposition process. A final re-design of the injector coupling was made after two potential problems with the initial design were identified. First, with all the reactants entering the reactor through the same injector (done to ensure intimate gas mixtures), the presence of BCl_3 and $SiCl_4$ were determined to possibly be interfering with the chlorination of the hafnium sponge[94]. Secondly, BCl_3 is known to have some affinity for silicon[94]; it could be reacting with both the $SiCl_4$ gas and the silicon in the mullite tube. (The desiliconization of mullite has been shown to be primarily a surface phenomenon, with the reaction slowing after a surface alumina layer has been formed[95].)

To prevent these gases from interfering with the $Hf + 2Cl_2 \rightarrow HfCl_4$ reaction or from reacting with each other, alumina rods (24" long, 1/4" diameter) were used to deliver each gas separately to the hot zone, 1" from the substrate surface. Since Swagelok compression fittings cannot be used on the alumina rods for maintaining a good vacuum seal, an o-ring to compression fitting union was designed, with Metra, Inc., Linthicum, MD fabricating the desired component. This union was used to join the alumina rods to the 1/4" stainless steel tubing from the mass flow meters, and an o-ring fitting was welded to the injector end-cap to feed the alumina rod into the mullite reactor tube. The final injector system design is shown in Figure 16.

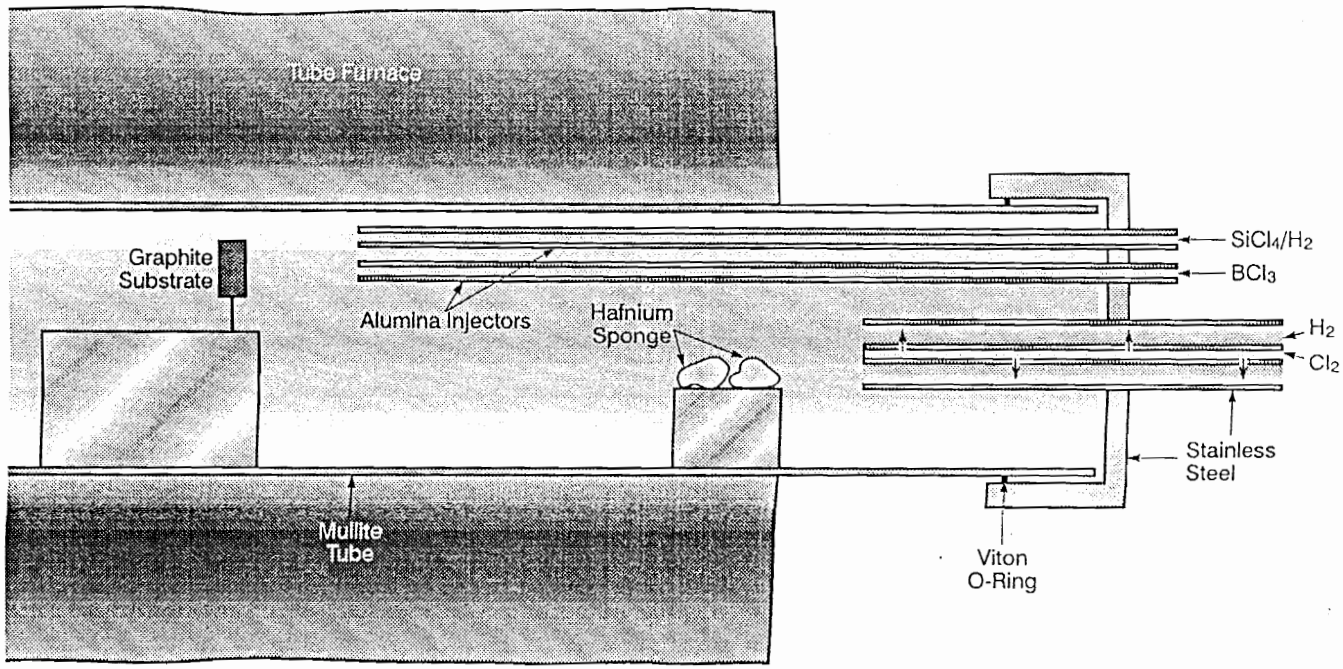

Figure 16. Final Design of Hot-Wall CVD Reactor

The gases used in these experiments, H_2, Cl_2, BCl_3, and argon, were high purity (>99.999%) Air Products reagents. The gas delivery system used to meter precise amounts of Cl_2 to the hafnium sponge, H_2 to the $SiCl_4$ bubbler, excess H_2, and BCl_3 was composed of four MKS Type 1259 Mass Flow Controllers coupled into an MKS Type 247 Digital Readout/Controller. These highly accurate electronic mass flow meters are calibrated using N_2, so standard flow rates for the reactant gases were calculated based on the size of the flow controller, gas density, and specific heat[96]. Corrosion-resistant regulators and check valves were used to control gas flow from the cylinders. Stainless steel or Teflon tubing (with stainless steel Swagelok® compression fittings) was used to deliver the gas from the bottles to the flow controllers, and the flow controllers to the vacuum coupling on the reactor tube.

3.2.4 Pressure Control and Exhaust System

To maintain the desired total chamber pressure and handle the reaction product and unreacted gases, a pressure control and exhaust system was designed. The heart of the pressure control system is the mechanical vacuum pump, a Leybold-Heraeus Trivac® D8A Rotary Vane Pump, with a pumping speed of 5.3 ft^3/min. For ultimate vacuum measurement, an MKS Series 315 SensaVac Digital Pirani Gauge System, with temperature compensated sensor tube and leak detection alarm capabilities was mounted near the vacuum pump. The total system pressure must be below 80 mtorr to ensure that no leaks are present before any experiment is initiated. This ensures the elimination of ambient air from entering the system. The importance of this is not only for the purity of the desired deposition reaction, keeping oxides and nitrides from forming, but with the explosive limits of H_2-O_2 gas mixtures at reaction temperatures being roughly 5%, even small leaks can be extremely dangerous.

To monitor and adjust the reactor pressure during the experiment, a gas-ballast technique was employed. An MKS Baratron Pressure Transducer was placed in the exhaust port line as close to the reactor as possible. This capacitance manometer measured the total system pressure, and sent a signal to an MKS Type 250C Pressure Controller, where the pressure readout is located. This controller, hooked to an MKS Type 248A Control Valve,

raised and lowered the pressure to the desired level by opening and closing the valve, dumping variable amounts of argon directly to the vacuum pump.

The gas exhaust system is a fairly basic design. An ice-water cold trap, placed immediately past the exhaust side o-ring coupling, lowered the temperature of the gases before they went into the vacuum pump. This trap also removed some of the chloride gases by precipitation on the outer surface of the cold trap wall. This helped alleviate any hot corrosion of the vacuum pump housing, as well as reducing environmental problems associated with corrosive gas venting. Chlorides remaining in the gas stream were neutralized by a soda-lime scrubber placed in the exhaust line between the pump and the fume hood. All remaining gases were then vented through the fume hood to the atmosphere.

An overall view of the chemical vapor deposition system showing the pressure control and exhaust features is seen in Figure 17. A custom-built fume hood, with a chemical-resistant wood-top bench as its base, and an aluminum-framed plexiglas paneled walls and ceiling is vented into an existing air-handling unit in Building 26 at NSWC.

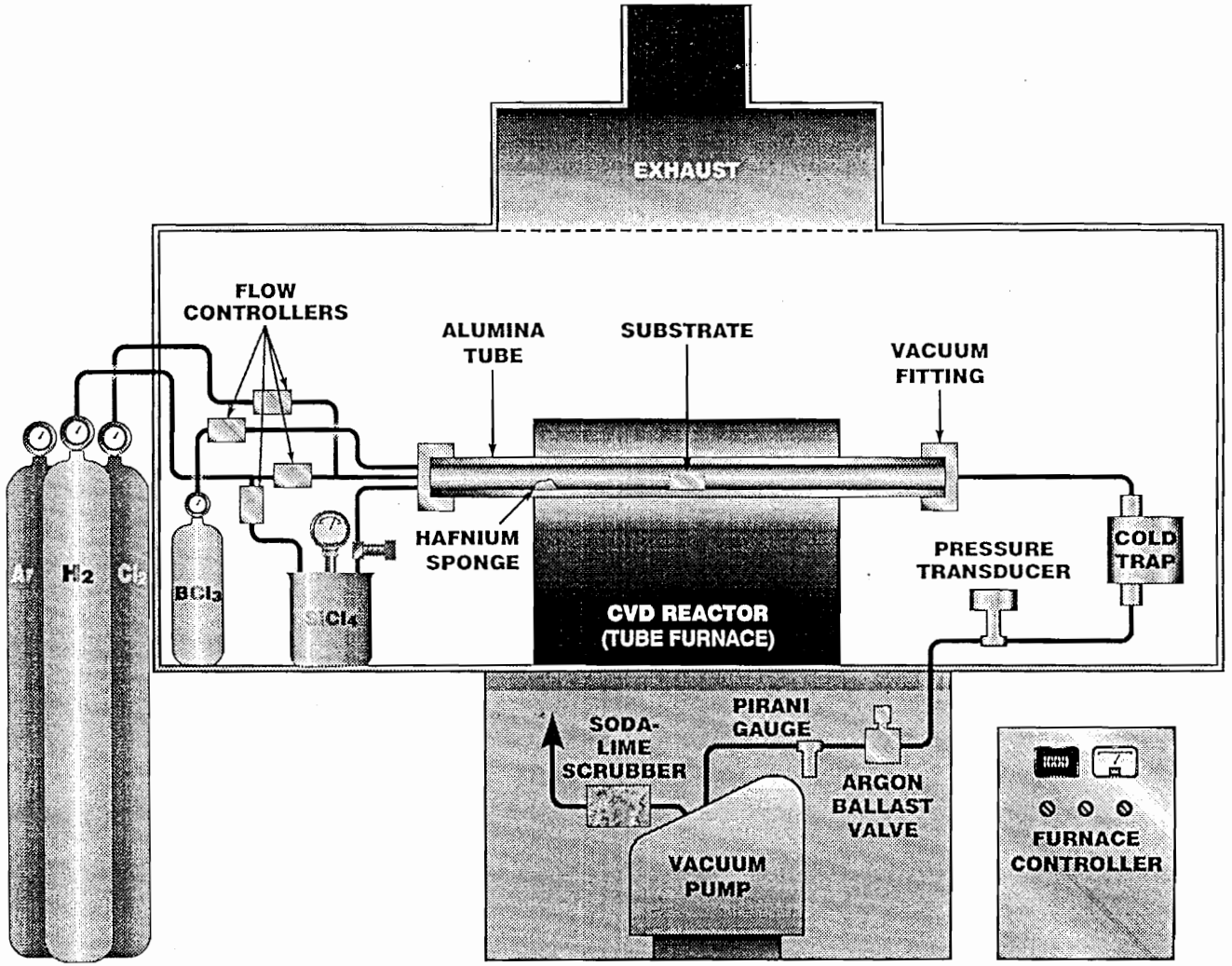

Figure 17. Schematic of Complete Chemical Vapor Deposition System

3.3 Source Materials

The gases used in this study, BCl_3 (electronic grade), Cl_2 (electronic grade), and H_2 (ultra high purity) were purchased from Air Products Specialty Gas Division. The hafnium sponge (97% pure, balance zirconium, -75 + 20 mesh) and silicon (IV) chloride ($SiCl_4$- 99% pure) were purchased from Johnson Matthey/Alfa Products. Reagent-grade indicating soda-lime pellets from Baker Scientific was used to scrub effluent gases before venting through the fume hood. Unocal-76 POCO Graphite rods, 1/2" diameter and 6" long, Grade AXF-5Q (5μm grain size, 0.8 μm pore size, 20% porosity) were purchased as the substrate material.

3.4 Experimental Procedure

The graphite substrates were cut (approximately 1/4" thick) and sanded to a 600 grit finish. A 1/8" hole was drilled on the circumferential surface to allow vertical mounting in the reactor furnace. The substrates were then ultrasonically cleaned in methanol and dried. The substrates were then weighed, mounted on an alumina rod, and placed on the graphite pedestal, as shown in Figure 16. This fixture was positioned in the center of the tube furnace hot zone, 18" from the tube end.

A small amount (2-5 grams) of hafnium sponge was placed on a graphite block, which was then placed in the tube furnace 10" in front of the substrate. (This step was omitted when pure SiB_4 coatings were produced.) The gas injector/vacuum coupling was then carefully positioned on the tube end such that the alumina gas feed tubes straddled the hafnium sponge in the near-end of the reactor tube. After vacuum grease was applied to the Viton o-ring, the compression coupling was tightened by hand to ensure a good seal. An ice-water mixture was put into the cold trap, and fresh soda-lime was added to the exhaust gas scrubber.

The $SiCl_4$ bubbler was weighed, and all gas delivery lines were fastened. Lastly, the exhaust port coupling, pressure transducer, and cold trap seals were all connected. After checking all the fittings, the vacuum pump was engaged, and allowed to run for 30 minutes. The total system

pressure (ultimate vacuum) was then measured with the Pirani gauge. If the vacuum was not below 100 mTorr, then the entire system was leak checked. This was done by first closing off the vaccum chamber at the pump, and working forward through the exhaust port lines to the reactor tube and injector system to the gas bottles until the source of the leak was pinpointed.

Once the system passed the leak check, the furnace was programmed to heat (and cool) at a rate of 150°C/hour to the deposition temperature. This slow cycling was done to ensure small thermal gradients in the tube, keeping the tube from cracking during service. The heatup was done under vacuum, and a final leak check was performed when the furnace reached the deposition temperature to ensure safety and atmosphere purity in the reactor. The electronic mass flow controllers were activated, allowing any residual gas in the supply lines to be removed.

Next, the valve at the Pirani hot-cathode gauge was redirected to the exhaust line flow, allowing the argon gas ballast line to be evacuated. After the total system pressure equilibrated at the desired level, the reactant gas flow rates (for BCl_3, Cl_2, H_2 through the $SiCl_4$ bubbler, and excess H_2) were set on the MKS Type 247C Flow Controller, the cylinder valves were opened sequentially.

First, the excess H_2 was started, and the total system pressure

allowed to equilibrate (necessary due to the high flow rates used and the slow response time of the transducer and control valve). Next, the BCl_3 bottle was opened slowly, with care taken to properly adjust the cylinder and control valves such that the BCl_3 didn't condense in the feed lines or in the mass flowmeter. (Since it is a low pressure gas, a regulator can't be used. The electronic mass flowmeters will not function properly when the gas condenses to a liquid, and disassembly and cleaning are not trivial problems.) After a steady flow of BCl_3 is achieved, the Cl_2 cylinder is opened next. Lastly, the H_2 bypass valve at the top of the bubbler is turned, and $SiCl_4$ vapor is carried to the reactor. Depending on the H_2 flowrate, system pressure, and ambient temperature, the monel needle valve is adjusted to maintain a 2-3 psi pressure inside the bubbler. Since the bubbler pressure, BCl_3 flowrate, and total system pressure have often been found to vary throughout the experiment, they are constantly monitored to ensure steady reaction conditions and proper safety.

After the deposition is complete (typical runtimes were 40-90 minutes, resulting in coating thicknesses of 10-50μm), the BCl_3 and Cl_2 bottles are first shut off (because it takes 6-15 minutes to purge the tubing between the gas cylinder and the flow controller). The H_2 bottle is shut off last. After the furnace has cooled down under vacuum, the coated sample and unreacted hafnium sponge are removed from the reactor and weighed.

3.5 Characterization

The as-deposited coatings were characterized for phase composition using a Siemens Theta-Theta Series D-500 Diffractometer. Typical scan rates were two degrees (2θ) per minute at a 0.01 degree stepsize over the 20-60 degrees 2θ (to include the three main peaks of each phase). Peak identification was determined from the JCPDS[22] database. The surface microstructures were studied using an Amray Model 1000-A Scanning Electron Microscope. A JEOL Model 1000 Electron Microprobe was employed to determine the chemistry of microstructural features.

3.6 Deposition and Characterization of CVD Coatings

Before attempting to deposit the two-phase HfB_2-SiB_4 coating, the deposition of single-phase HfB_2 and SiB_4 coatings was studied to define the effects of processing variables on the deposition of each material. While the thermochemical modeling provided some insight into the processing conditions necessary to deposit each material, the influences of chemical kinetics and reactor design make an empirical study necessary. Once the desired compound has been successfully deposited, varying the deposition conditions can influence the microstructure and properties of the coating. In this Sections 3.6.1 and 3.6.2, the deposition experiments used to produce each pure boride will be reviewed, and the characterization of the coatings will be presented. In Section 3.6.3, the deposition and characterization of the two-phase HfB_2-SiB_4 will be described.

3.6.1 SiB_4 Deposition and Characterization

From the thermochemical modeling described previously in Section 3.1, it was expected that four condensed phases (B, Si, SiB_4 and SiB_6) could deposit from the precursors ($SiCl_4$, BCl_3, and H_2) used in the present study. The deposition reactions can be written as follows:

$$SiCl_{4\,(g)} + 2H_{2\,(g)} \rightarrow Si_{(s)} + 4HCl_{(g)}$$

$$BCl_{3\,(g)} + 3/2H_{2\,(g)} \rightarrow B_{(s)} + 3HCl_{(g)}$$

$$SiCl_{4\,(g)} + 4BCl_{3\,(g)} + 8H_{2\,(g)} \rightarrow SiB_{4\,(s)} + 16HCl_{(g)}$$

$$\text{and } SiCl_{4\,(g)} + 6BCl_{3\,(g)} + 11H_{2\,(g)} \rightarrow SiB_{6\,(s)} + 22HCl_{(g)}.$$

In the initial experiments, the original furnace design was used that allowed all gases to be mixed at the concentric injector port. The experimental conditions were similar to those defined in the thermochemical modeling (temperatures from 875 to 1100°C, pressures from 10 to 180 Torr), with low total gas flows (>700sccm) used for these runs. These first experiments were not successful in producing any coatings that could be detected by x-ray diffractometry. (This is probably due to a combination of factors. SiB_4 is a weak diffractor, while the substrate material, has high diffraction intensities. A fairly thick coating is thus required to make the SiB_4 "visible" above the graphite pattern.)

An interesting anomaly was observed during these initial experiments. While no thick dense coatings were produced under any of these conditions,

very low (>2 sccm) $SiCl_4$ and low (15sccm) BCl_3 flowrates and a H_2:reactant ratio of 20:1, a black and brown colored coating was found to deposit on the surface. This coating didn't appear to be dense and adherent, and x-ray diffraction did not reveal the presence of any crystalline phase. However, microscopic characterization show the presence of a tangled, wooly layer on the surface. As seen in Figure 18, the fibers appear to be somewhat translucent in nature, and are approximately 0.2 μm in diameter and over 20μm in length. EDAX analysis indicates that the fibers contain silicon, but light element detection is not possible with this unit, so the presence of boron cannot be determined.

While this deposition of whiskers is an interesting phenomenon, the original design of the reactor was determined to be inadequate for producing thick coatings due to gas phase reactions and precipitation in the exhause lines. As described in Section 3.2, the gas delivery system was re-designed to separate the chloride input gases until they reach the hot zone, increasing the diameter of the exhaust port, and installing a cold trap (to precipitate unreacted chlorides before they reach the vacuum pump). After these changes, the silicon boride deposition experiments resumed. Based on the experience gained in the previous experiments, the deposition conditions were narrowed to lower pressures (10-50 Torr), higher temperatures (1100-1300°C) and higher hydrogen concentrations, with the B:Si ratio ranging

from 6:1 to 1:1. Typical total flowrates were 650-700 sccm, but were as high as 1900 sccm for the highest hydrogen ratio. A listing of experimental conditions used for the deposition of SiB_4 is shown in Table 6. Under these conditions, the weight gained by the substrate during deposition was greater than in the initial experiments. X-ray diffraction of these samples (with a coating thick enough to be measured) revealed that SiB_4 was the only crystalline phase deposited under all deposition conditions[112]. Figure 19 shows a typical XRD pattern for SiB_4 on a graphite substrate.

After the phase composition determination was completed, the surface morpholgies of the as-deposited films were analyzed by scanning electron microscopy. Figures 20, 21 and 22 show three distinct morphologies of SiB_4. Figure 20 shows a fairly thin coating that still seems to be in the early stages of growth, with the grains not completely touching. These grains have domed morphology, which is typical of CVD coatings. In Figure 21, an exaggerated growth of some of the grains seem to have resulted in a non-uniform deposition surface. A faceted columnar structure is shown in Figure 22.

In some samples, both domed and faceted morphologies were observed. The proximity of the separate $SiCl_4$ and BCl_3 injectors to the substrate, necessary to prevent gas phase reactions, has caused regions of high and low supersaturation of each specie at different points across the

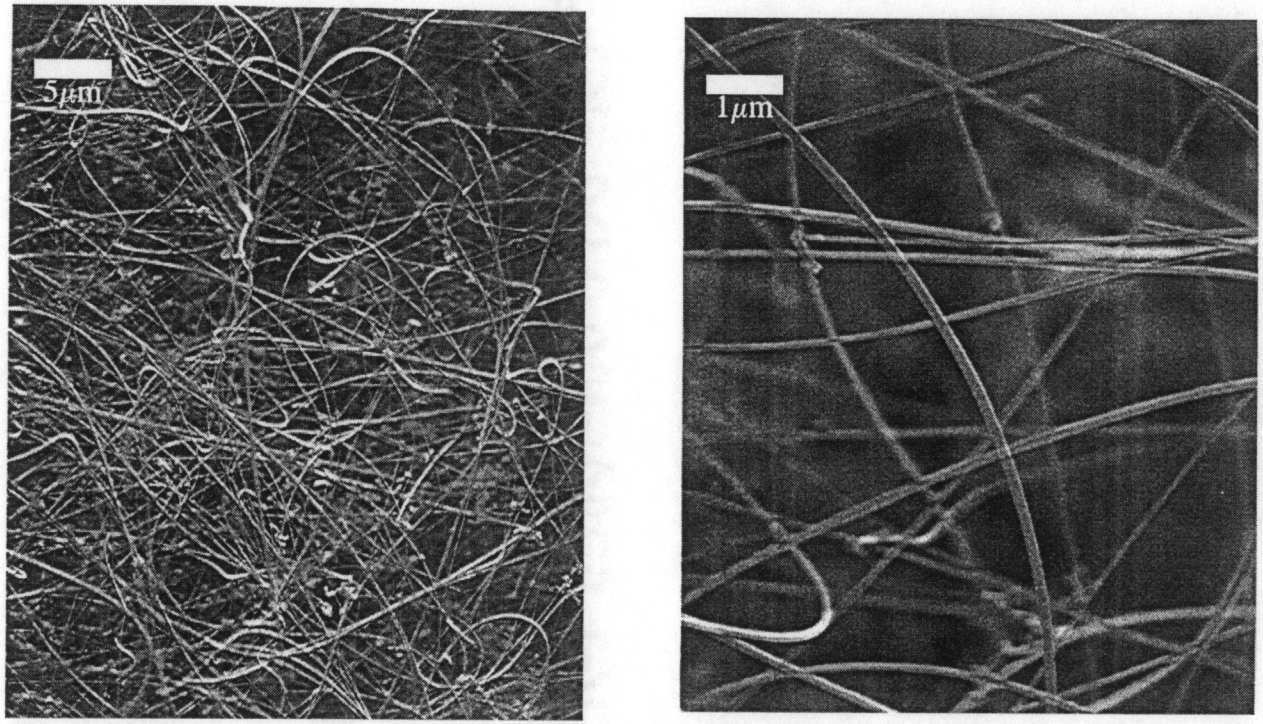

Figure 18. Scanning Electron Micrographs of Fibrous Coating

Table 6. Experimental Conditions for SiB_4 Deposition

T (°C)	875	1000	1000	1000	1025	1075	1100	1100	1100	1100	1100	1150
P (Torr)	180	50	170	25	50	50	50	50	50	25	25	25
H_2 Ratio	20	10	15	10	15	15	10	15	10	10	15	10
Total Flow	1000	500	650	650	800	800	450	800	500	500	1300	450

T (°C)	1200	1200	1200	1200	1200	1200	1200	1200	1200	1300
P (Torr)	50	25	25	250	25	10	50	25	25	25
H_2 Ratio	15	10	10	20	15	10	10	10	20	10
Total Flow	350	650	650	1000	500	650	650	700	1900	650

substrate surface due to poor gas mixing. In an attempt to solve this problem, the BCl_3 injector was moved a few inches away from the substrate surface to increase mixing. This placement, however, caused that injector to become clogged by boron deposited at that outlet at the lower temperature, shutting off further BCl_3 flow to the substrate. After that experiment, both injectors were returned to their original positions near the substrate surface.

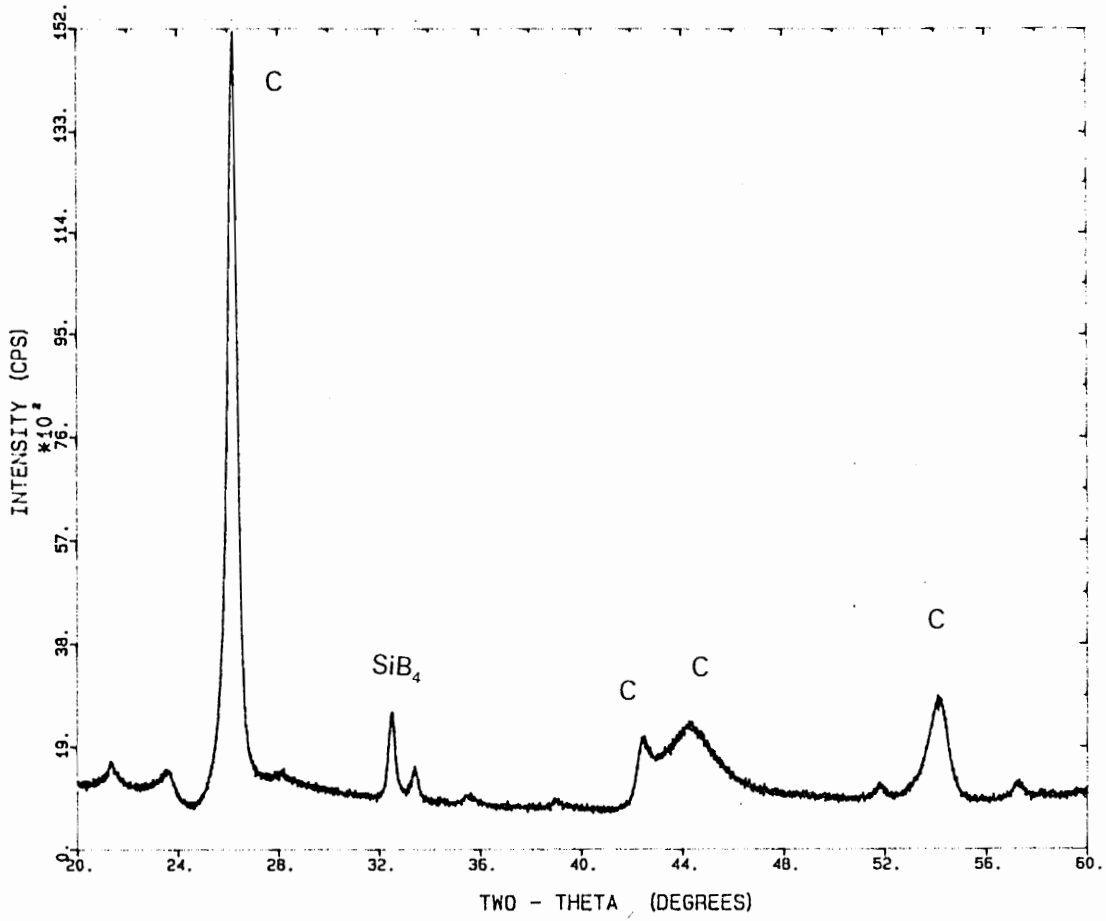

Figure 19. X-Ray Diffractogram of SiB_4 Coating on Graphite

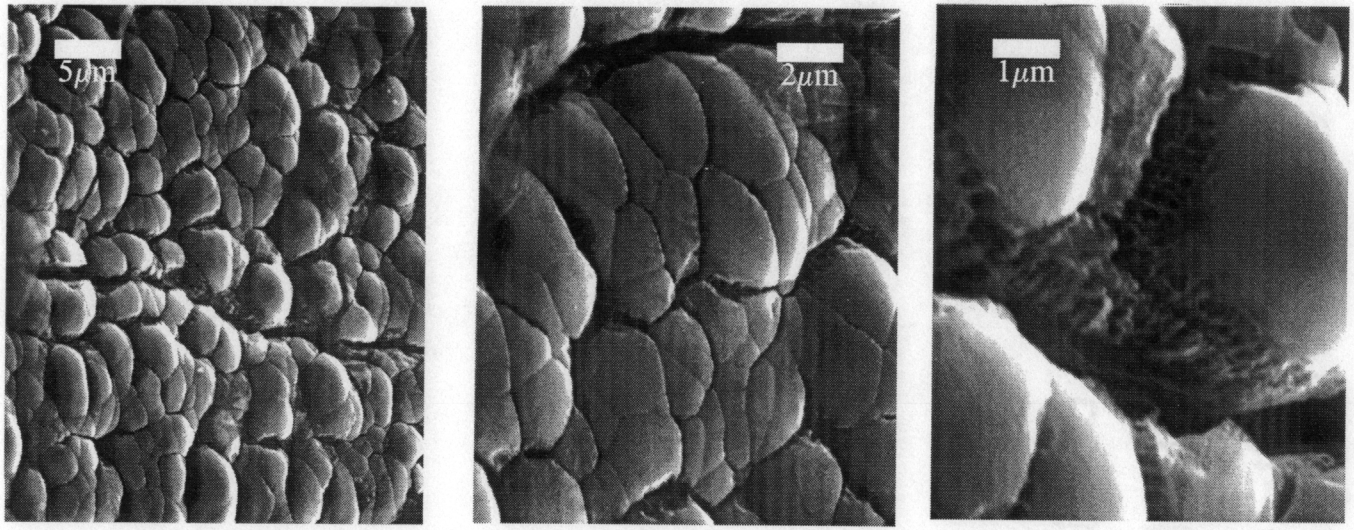

Figure 20. Scanning Electron Micrographs of SiB_4 Coating Showing Domed Morphology

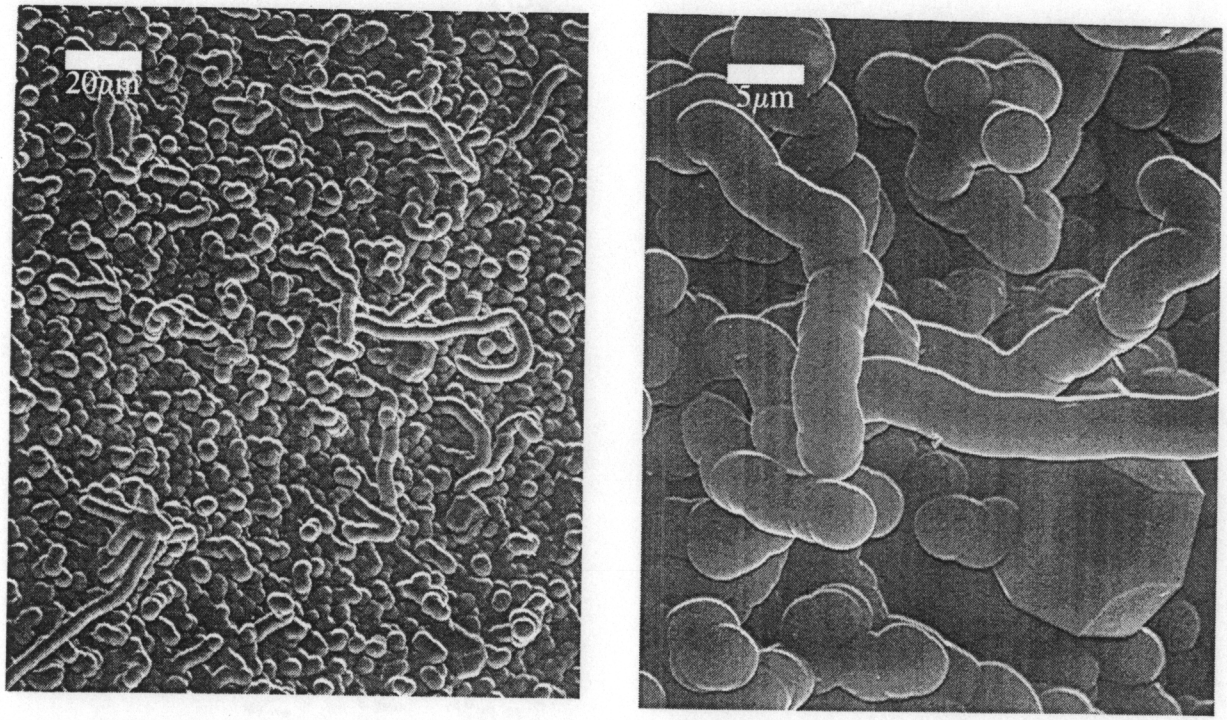

Figure 21. Scanning Electron Micrographs of SiB_4 Coating Showing Preferred Growth of Some Grains

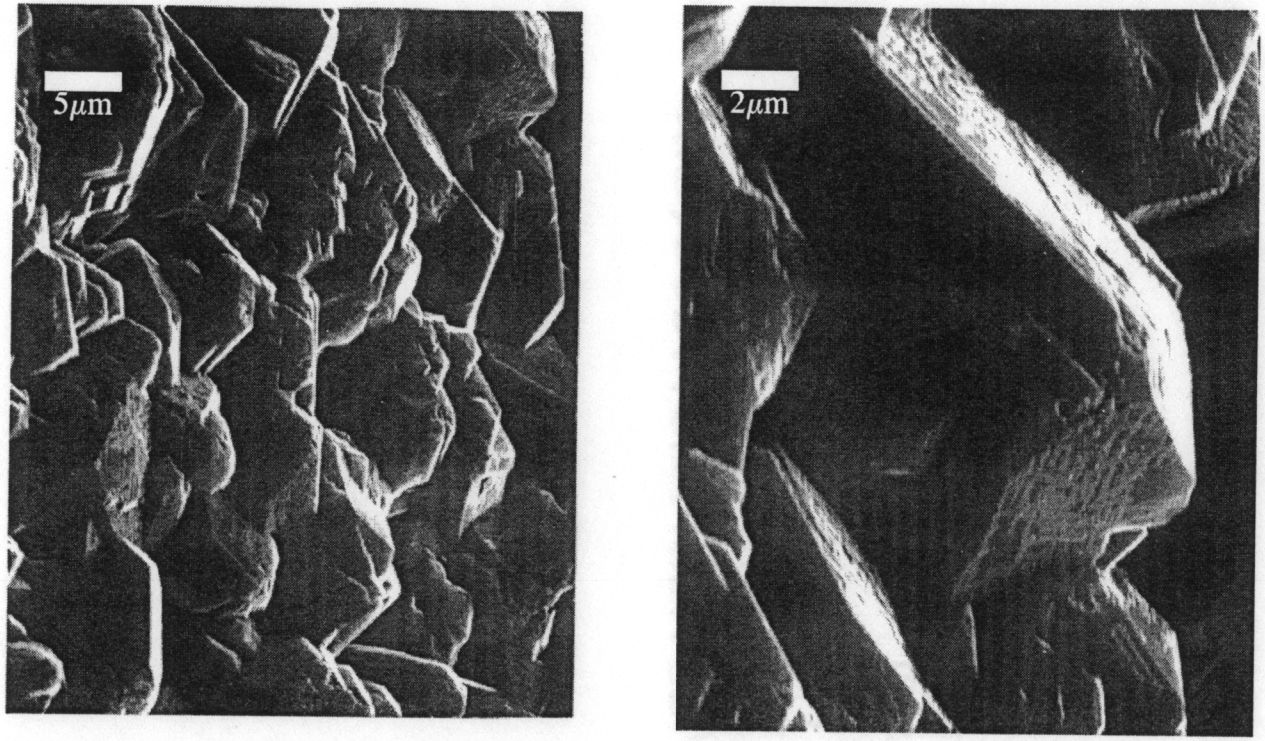

Figure 22. Scanning Electron Micrographs of SiB_4 Coating Showing Faceted Morphology

3.6.2 HfB_2 Deposition and Characterization

The deposition of HfB_2 is assumed to proceed via the reaction

$$HfCl_{4\,(g)} + 2BCl_{3\,(g)} + 5H_{2\,(g)} \rightarrow HfB_{2\,(s)} + 10HCl_{(g)}.$$

The in-situ production of $HfCl_4$ (described in Section 3.2) proceeds from the direct chlorination of hafnium metal sponge according to the reaction

$$Hf_{(s)} + 2Cl_{2\,(g)} \rightarrow HfCl_{4\,(g)}$$

at temperatures above 200°C.

As discussed in Section 3.2, the initial experiments involving $HfCl_4$ generation in a pre-reactor furnace were not successful. While the separate chlorination furnace allowed excellent temperature control for the reaction to produce $HfCl_4$, the stability of the chloride gas was not good. White chloride powder precipitated in the feed lines, clogging further flow to the deposition furnace. Heating tape was wrapped around the stainless steel lines to keep the temperatures above 250°C, but this problem still remained. Therefore, the in-situ design was introduced, and the separate injection of BCl_3 past the chlorination zone (to keep from interfering with the chlorination reaction) allowed the deposition experiments to proceed.

The experimental conditions used for the deposition were in the same ranges as those used for SiB_4 deposition, as shown in Table 7.

Table 7. Experimental Conditions for HfB_2 Deposition

Run	31	32	33	34
T (°C)	1200	1200	1100	1100
P (Torr)	25	50	50	25
H_2 Ratio	10	10	10	10
Total Flow	850	850	850	850

The B:Hf ratios were not easily determined for these experiments due to the difficulty of controlling the hafnium chlorination reaction, as well as measuring the weight loss of the hafnium sponge after the reactions (due to the formation of chloride compounds on the surface).

The thermodynamic modeling described in Section 3.1 concluded that metallic Hf should not be a stable condensed phase, and at high temperatures and high BCl_3 concentrations, boron should deposit. X-ray diffraction analysis of all coatings produced during these experiments were found to be in agreement with these predictions, with no crystalline B deposited with the HfB_2 coatings. This was also the case for the SiB_4 deposition described above. Figure 23 shows a typical diffraction pattern for HfB_2 deposited on graphite.

Scanning electron microscopy was employed to study the surface morphology of these coatings. At high deposition temperatures and low hydrogen concentrations, a porous coating was produced, as shown in Figure 24. Figure 25 shows a familiar domed morphology of CVD coatings, while in Figure 26, a more faceted surface is seen.

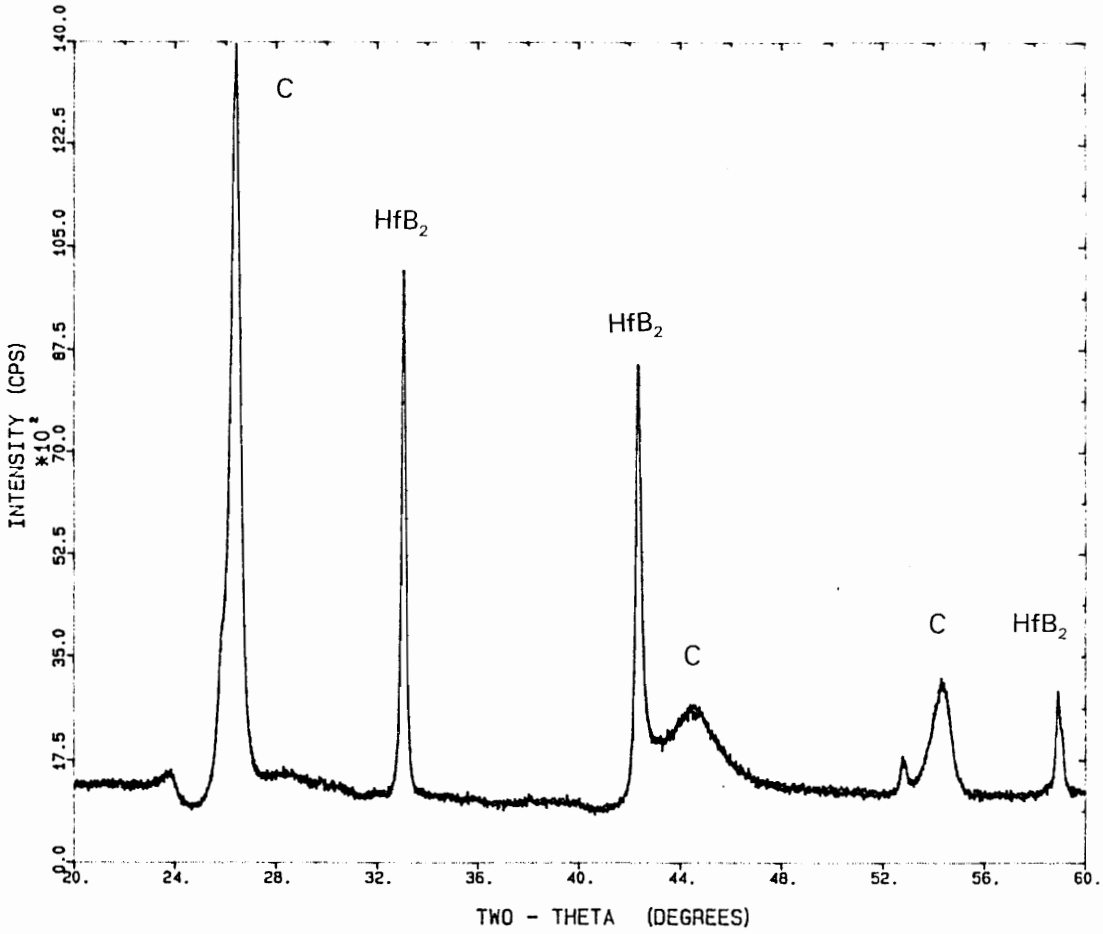

Figure 23. X-Ray Diffractogram of HfB_2 Coating on Graphite

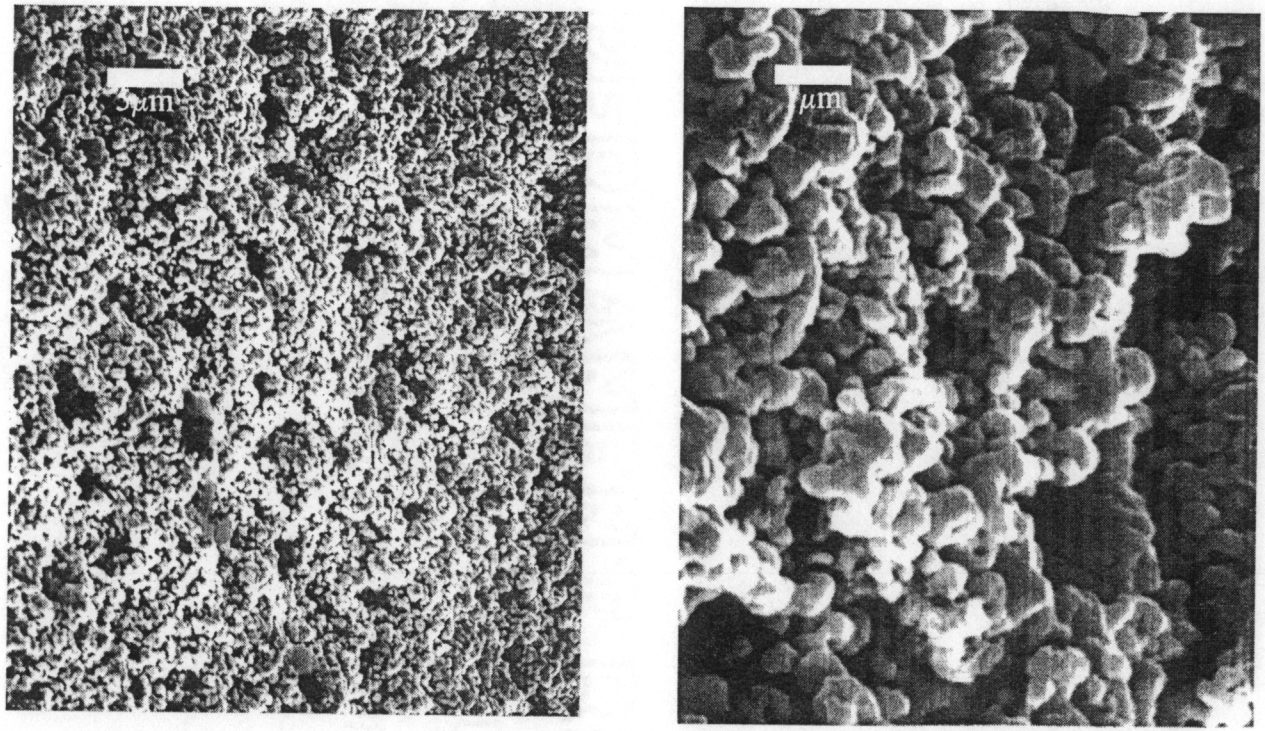

Figure 24. Scanning Electron Micrographs of HfB_2 Coating Showing Porous, Spherical Morphology.

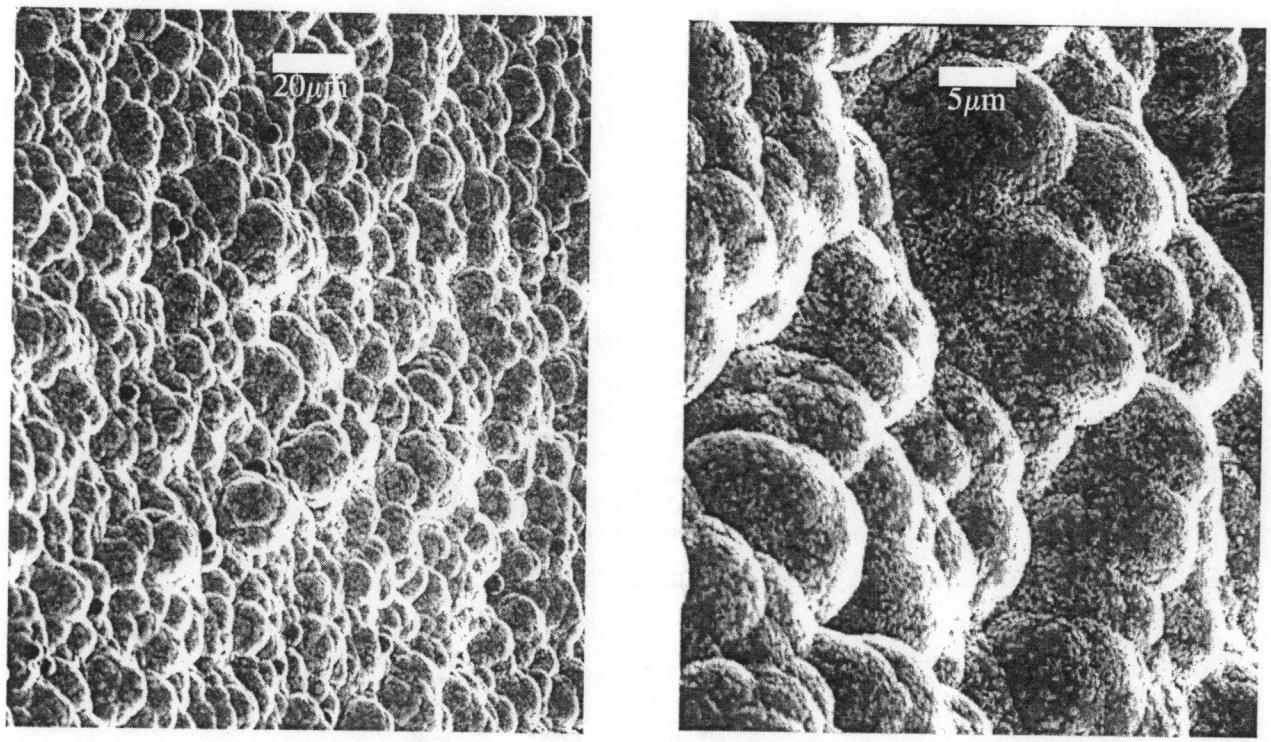

Figure 25. Scanning Electron Micrographs of HfB_2 Showing Domed Morphology

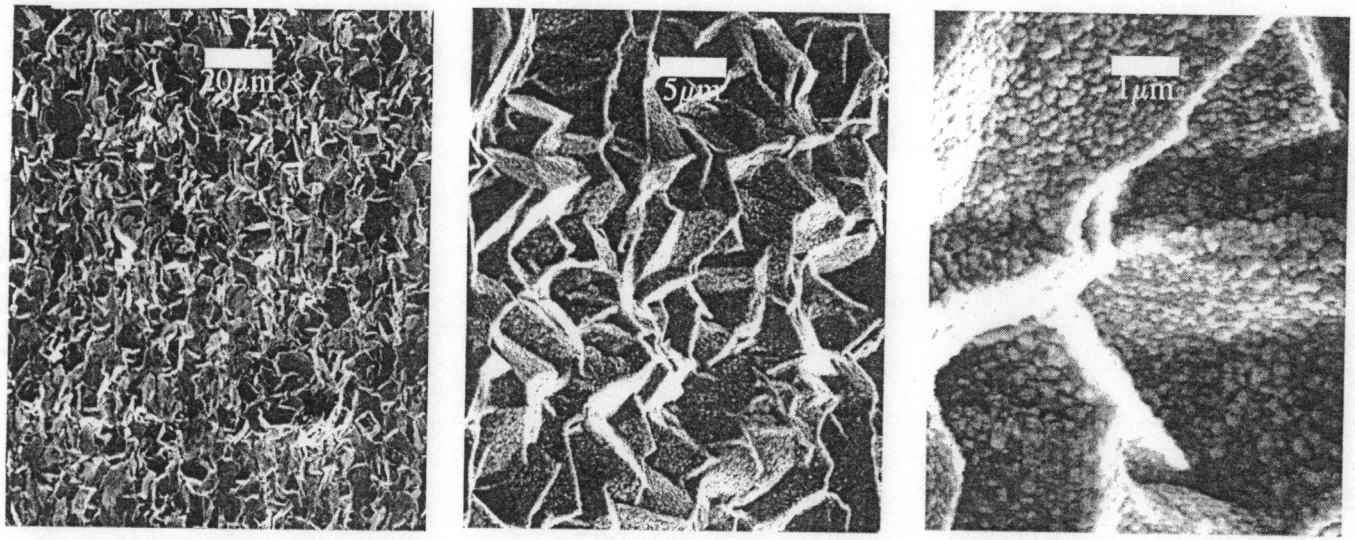

Figure 26. Scanning Electron Micrographs of HfB_2 Coating Showing Faceted Morphology

3.6.3 HfB_2-SiB_4 Codeposition and Characterization

After successfully depositing both HfB_2 and SiB_4 separately, with each phase shown to exhibit a variety of microstructures, the co-deposition of these materials was next studied. The conditions chosen for the codeposition was based on the results of the end-member deposition studies, since both end members were deposited under similar conditions. The range of processing conditions that should produce the best coatings (based on the end-member depositions) was determined to be:

Temperature: 1100-1200°C

Pressure: 20-50 Torr

H:(Hf + Si + B + Cl) = 10:1 - 30:1

The B:Si ratio was greater than 3, since extra B would be required to form HfB_2. The H_2 flowrates necessary to produce the ratios necessary to form both compounds resulted in total gas flowrates of 1000-2200 sccm. The deposition conditions used for some of the two-phase experiments are shown in Table 8.

An internal standard calibration method[98-100] was used to perform quantitative analysis on the two-phase coatings. To produce the calibration curve, mixtures of HfB_2 and SiB_4 powders (-325 mesh, both purchased from Cerac, Inc.) containing 10, 20, 30, and 40% HfB_2 were blended in a mortar and pestle.

Table 8. Experimental Conditions for Two-Phase HfB_2- SiB_4 Deposition

T (°C)	1100	1100	1100	1100	1100	1100	1100	1100	1200	1200	1200	1200	1200	1200	1200
P Torr	20	20	40	20	40	40	20	20	20	40	40	40	40	20	40
H_2	10	10	10	20	20	20	20	20	10	10	10	20	20	10	20
Tot Flow	900	1050	1300	2100	2100	2100	2100	2100	1050	1000	1300	2100	2100	1250	2100

These powders were placed on single-crystal quartz background slides, and scanned under the same conditions used to analyze the end-member coatings, as described in Section 3.5. It is seen in Figure 27 that HfB_2 is a much stronger diffractor than SiB_4, and SiB_4 cannot be detected when the amount of HfB_2 is greater than 40%. This technique, therefore, is not going to be able to quantify the phase composition of HfB_2-rich coatings, and will have limited utility in this study. The calibration curve that is based on the ratio of the measured peak heights of the two phases is shown in Figure 28.

An example x-ray diffraction pattern for a two-phase coating is shown in Figure 29. According to the correlation curve, this sample is approximately 15% HfB_2, and 85% SiB_4. No other phases, such as B, Si, or SiB_6, were detected during this part of the analysis, which agrees with the results described in Sections 3.6.1 and 3.6.2 for the end-member characterizations. The lack of any hafnium silicide formation agrees with the thermodynamic modeling results, which indicated that the silicide should not deposit when boron is present.

A wide variety of microstructures were produced during the two-phase deposition experiments. During this analysis, certain morphologies were observed that were similar to those seen in the single phase HfB_2 and SiB_4 coatings, while others had not been previously reported. Figure 30 shows three stages in the growth of the microstructure. In Figure 30a, the

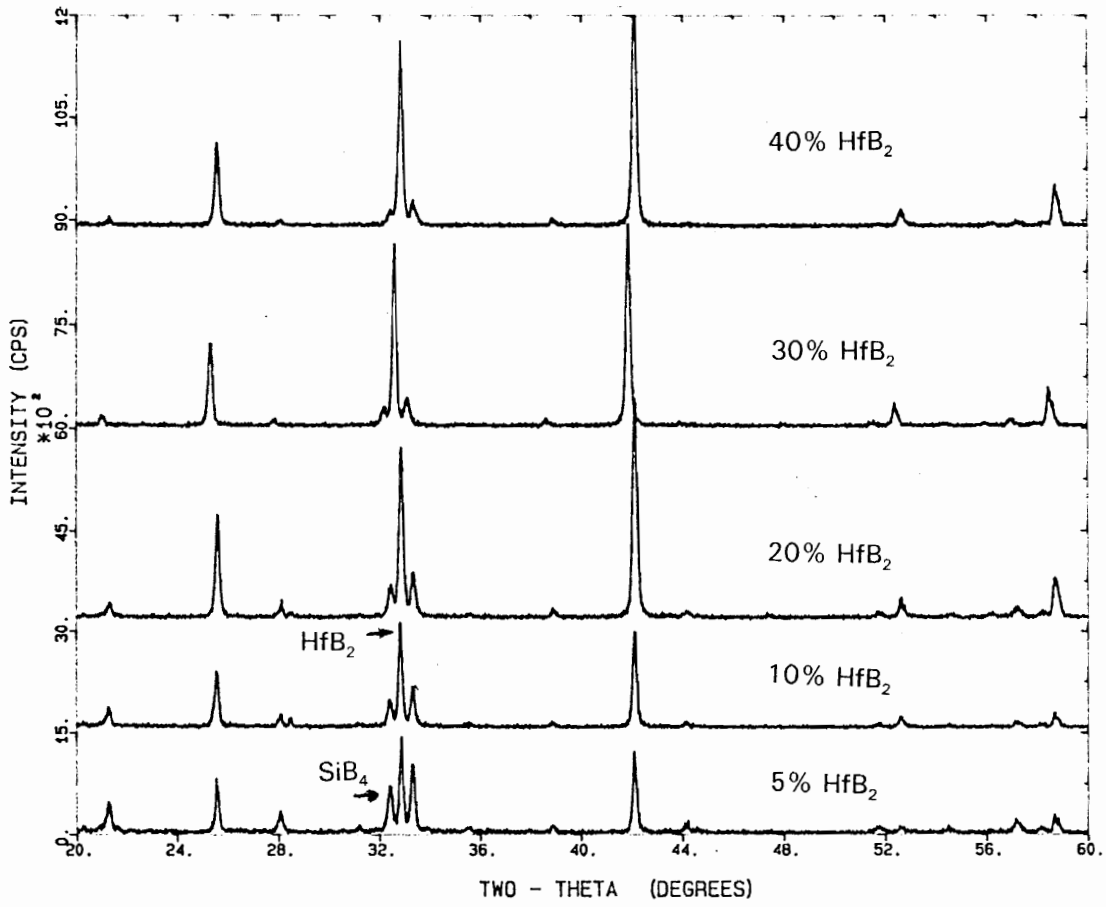

Figure 27. X-Ray Diffractograms of HfB_2-SiB_4 Powder Mixtures for Quantitative Analysis

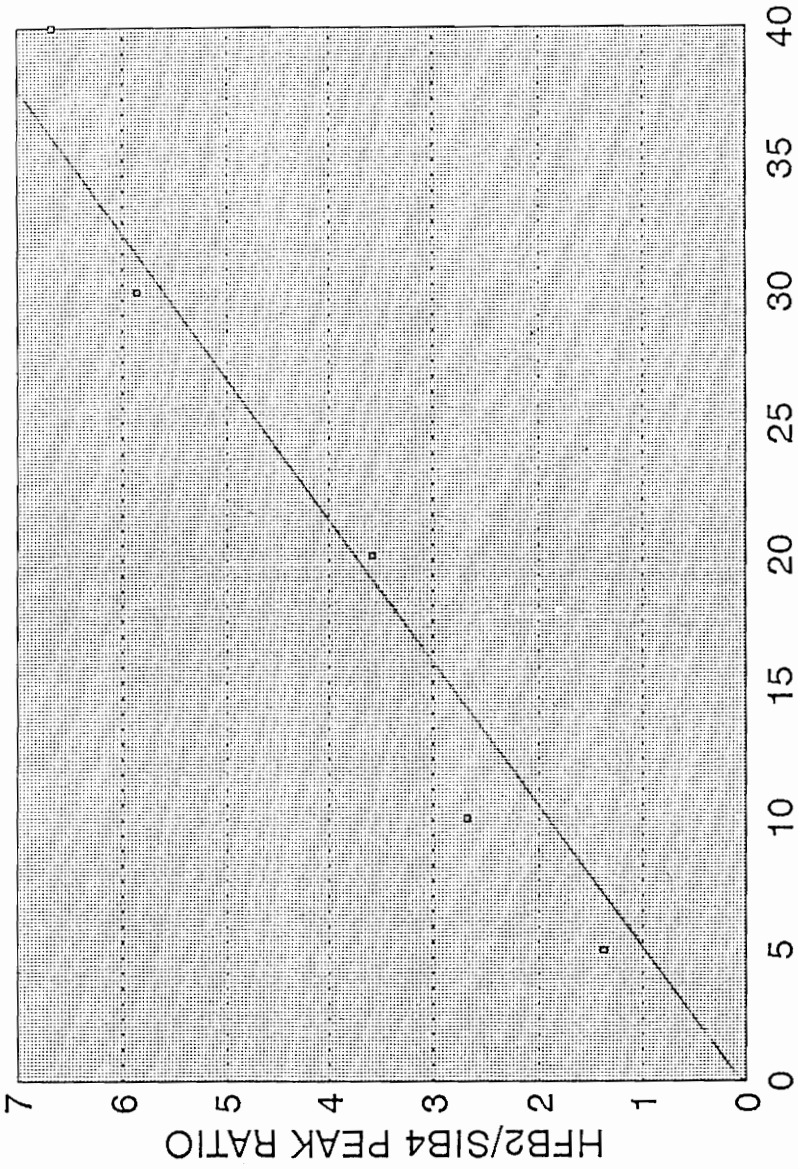

Figure 28. X-Ray Calibration Curve

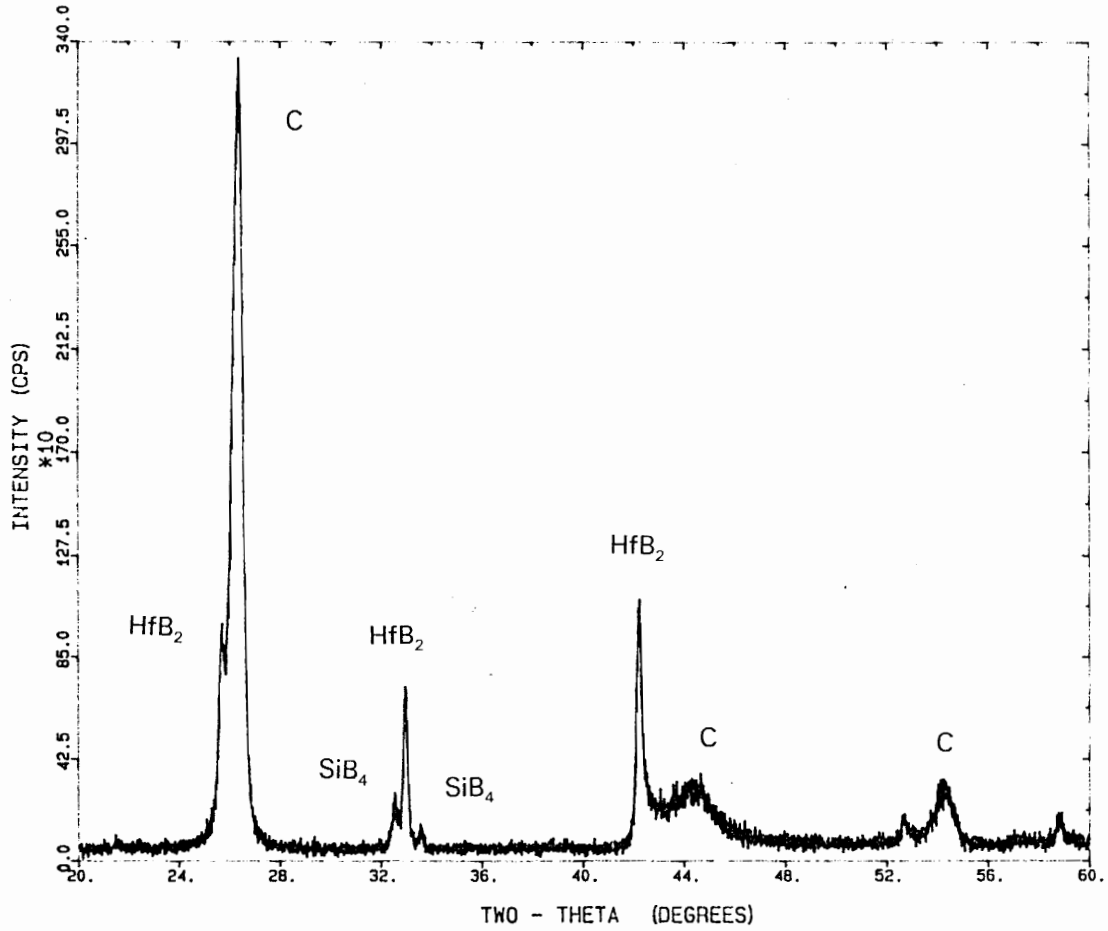

Figure 29. X-Ray Diffractogram of HfB_2-SiB_4 Two-Phase Coating on Graphite

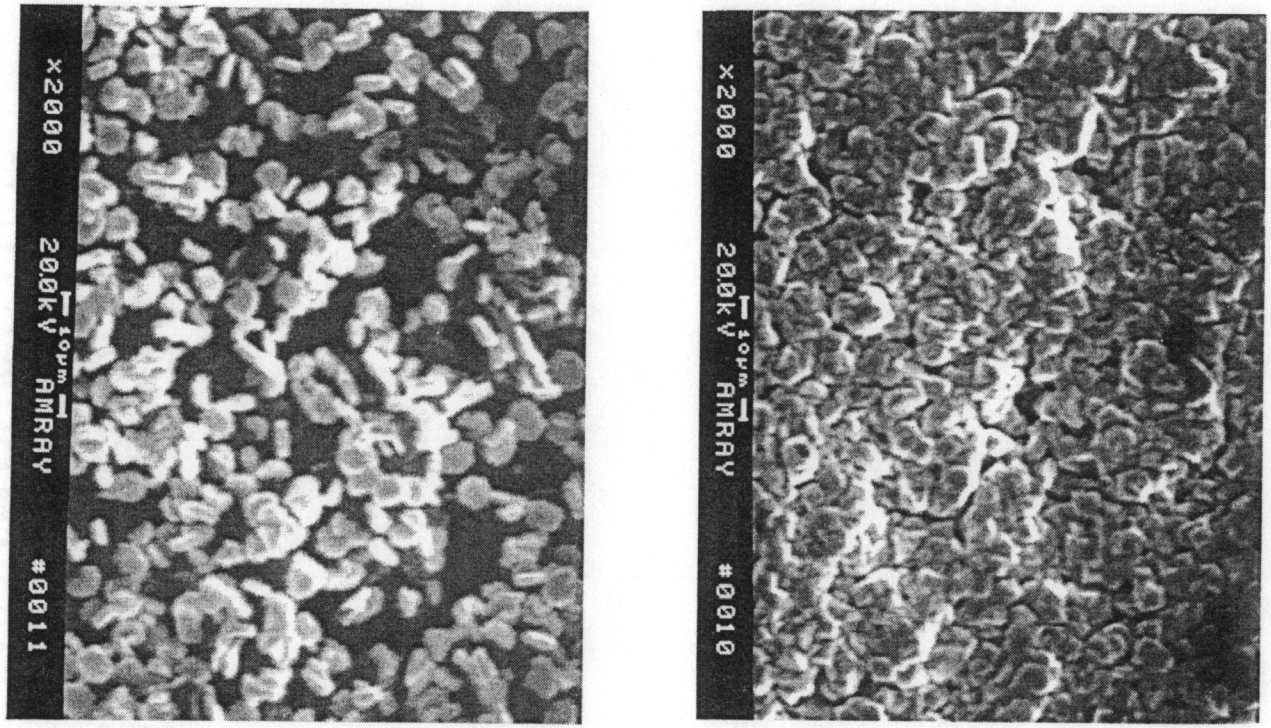

a b

Figure 30. Scanning Electron Micrographs of HfB_2-SiB_4 Coating Showing a) Separate Faceted Crystals, b) Crystals Impinging Upon Each Other

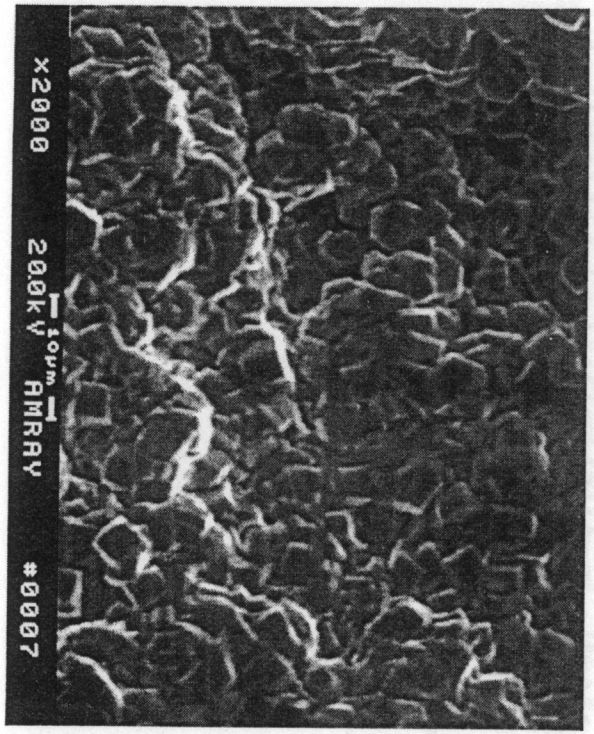

c

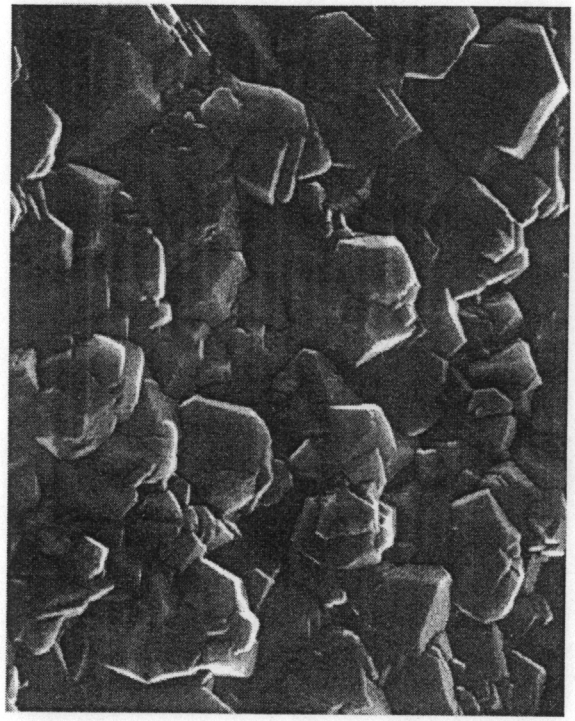

d

Figure 30 (continued). c and d) Continuous Dense Coating

film has not completely covered the substrate surface, with faceted crystals of the coating sitting on the substrate surface. In Figure 30b, the faceted grains have impinged upon one another to begin forming a dense coating. In Figure 30c, these crystals have formed a dense coating, and 30d is a higher magnification of these faceted grains showing the high density of the film. Figure 31 looks much like the single phase SiB_4 coating shown in Figure 20, exhibiting domed grains that are just beginning to form a continuous layer (seen in Fig. 31b). Figure 32 strongly resembles the SiB_4 coatings seen in Figure 21. Figure 33 seems to show a sequential growth of clusters of these "worms", with the grains growing more rapidly looking brighter in the SEM images because of charging caused by them being elevated from the substrate surface. Figure 34 shows a porous coating that is quite similar to that exhibited by the HfB_2 film shown in Figure 24. The grains in Figure 34a have a more spherical morphology, while 34b seems to exhibit a more needle-like appearance.

The two-phase microstructures presented in Figure 35 show very small (1-2 μm) grain sizes in comparison to anything shown previously (except the spherical particles in Figure 24 that are likely a product of gas phase nucleation). Figure 35a shows what appears to be submicron grains clustering together as they grow out from the substrate surface. In Figure 35b, it is seen that some of these grains seem to be forming "cauliflower"-

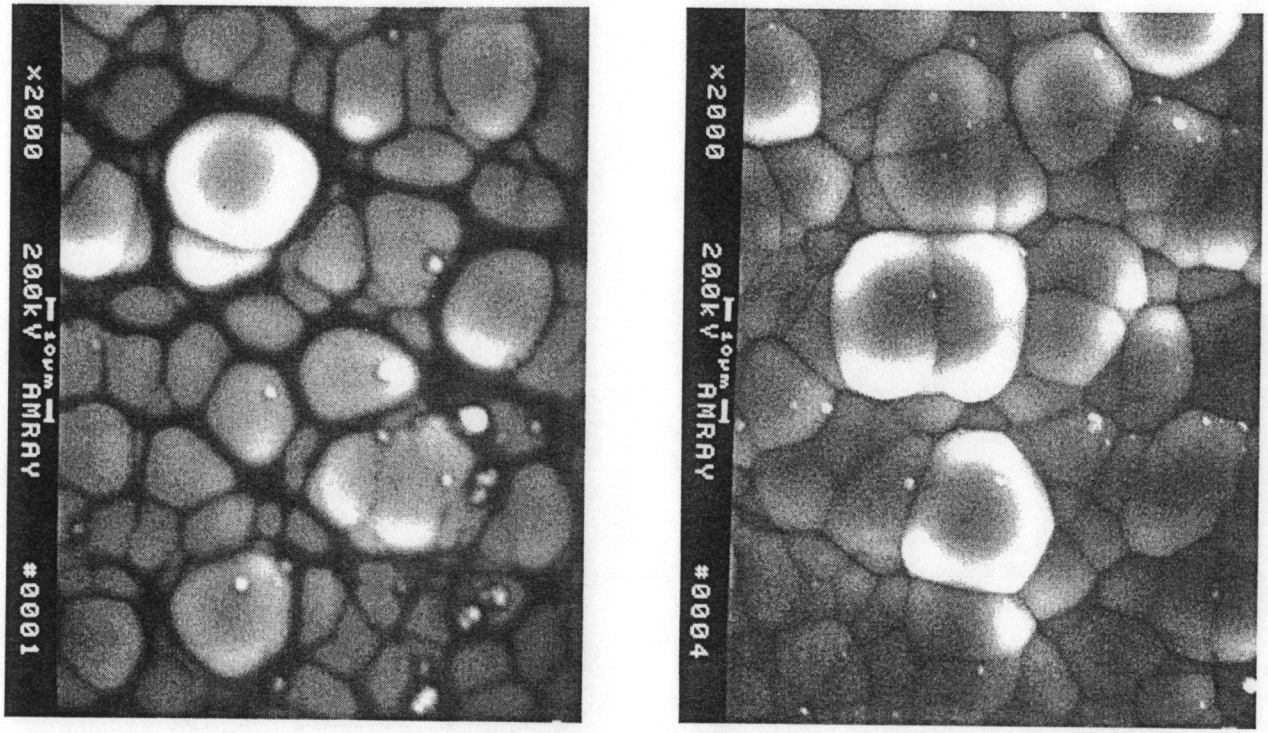

a b

Figure 31. Scanning Electron Micrographs of HfB_2-SiB_4 Coating Showing a) Discontinuous, and b) Continuous Domed Grains

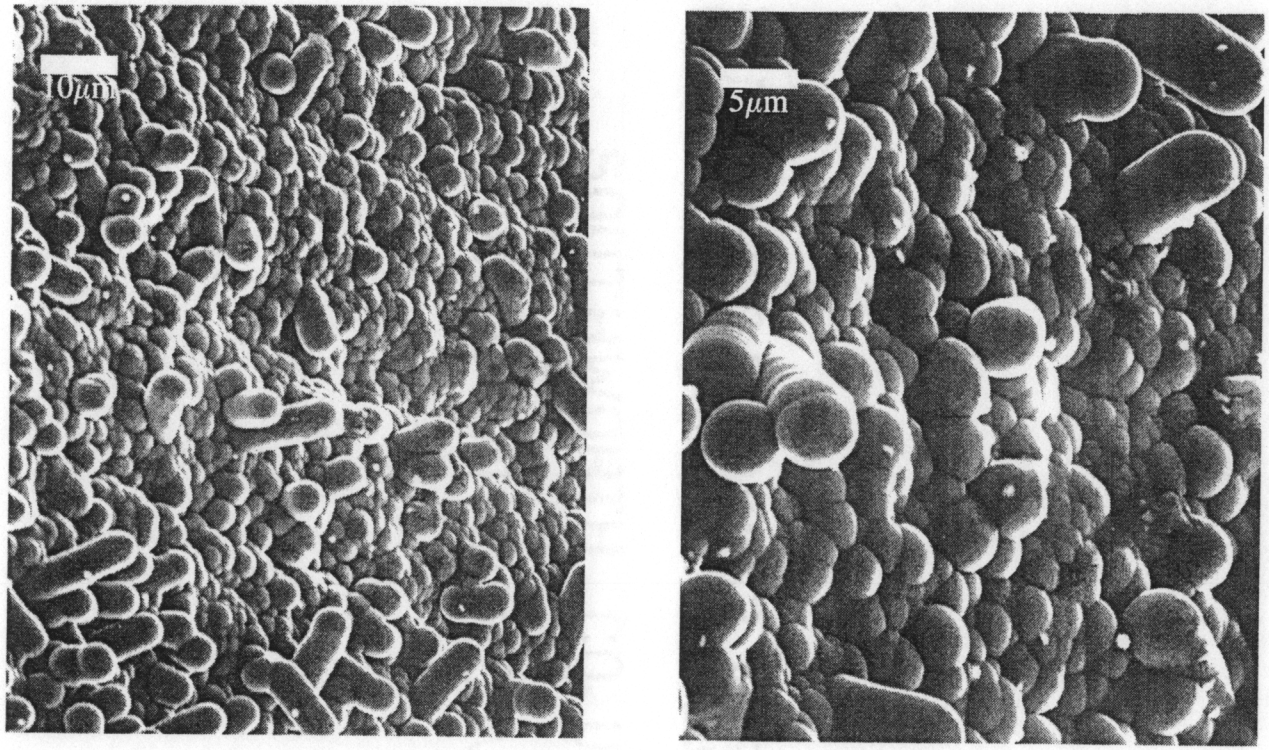

Figure 32. Scanning Electron Micrographs Oof HfB_2-SiB_4 Coating Showing Preferred Grain Growth

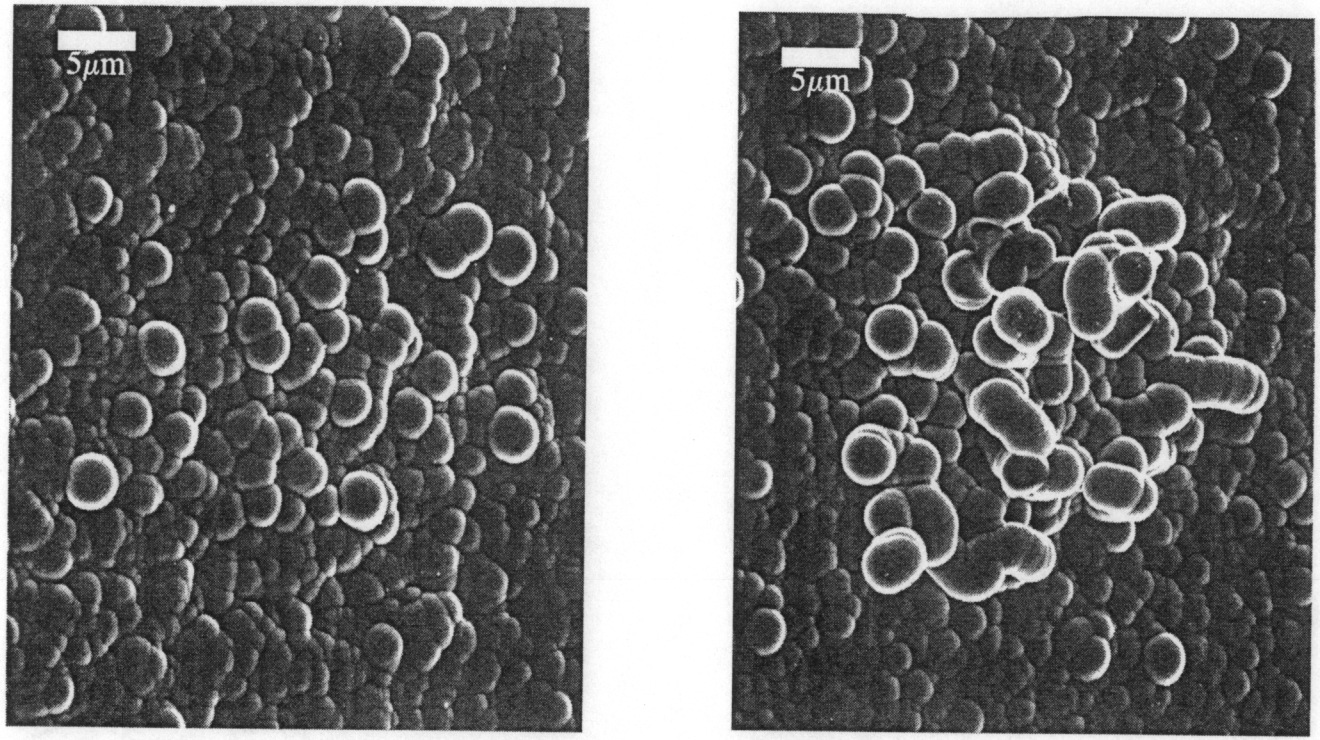

Figure 33. Scanning Electron Micrographs of HfB_2-SiB_4 Coating Showing Development of Clusters of Preferred Growth Sites

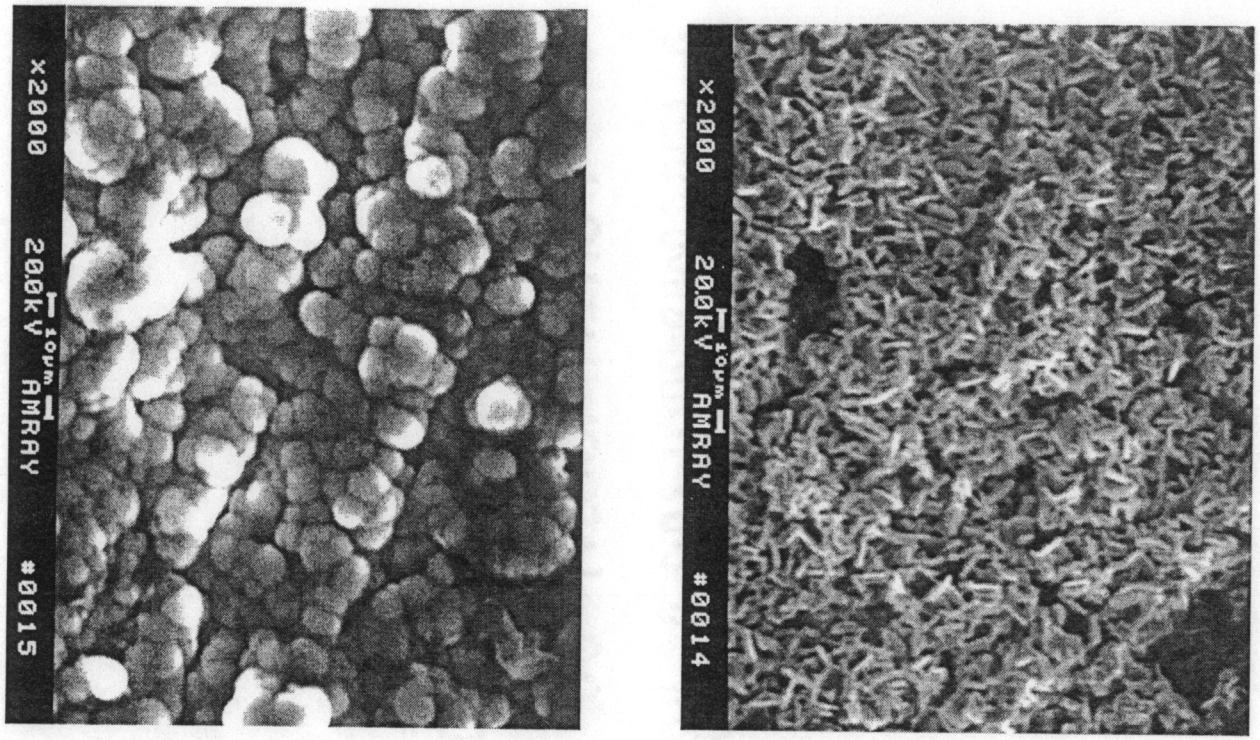

a b

Figure 34. Scanning Electron Micrographs HfB_2-SiB_4 Coating Showing a) Spherical, and b) Platelet Morphology

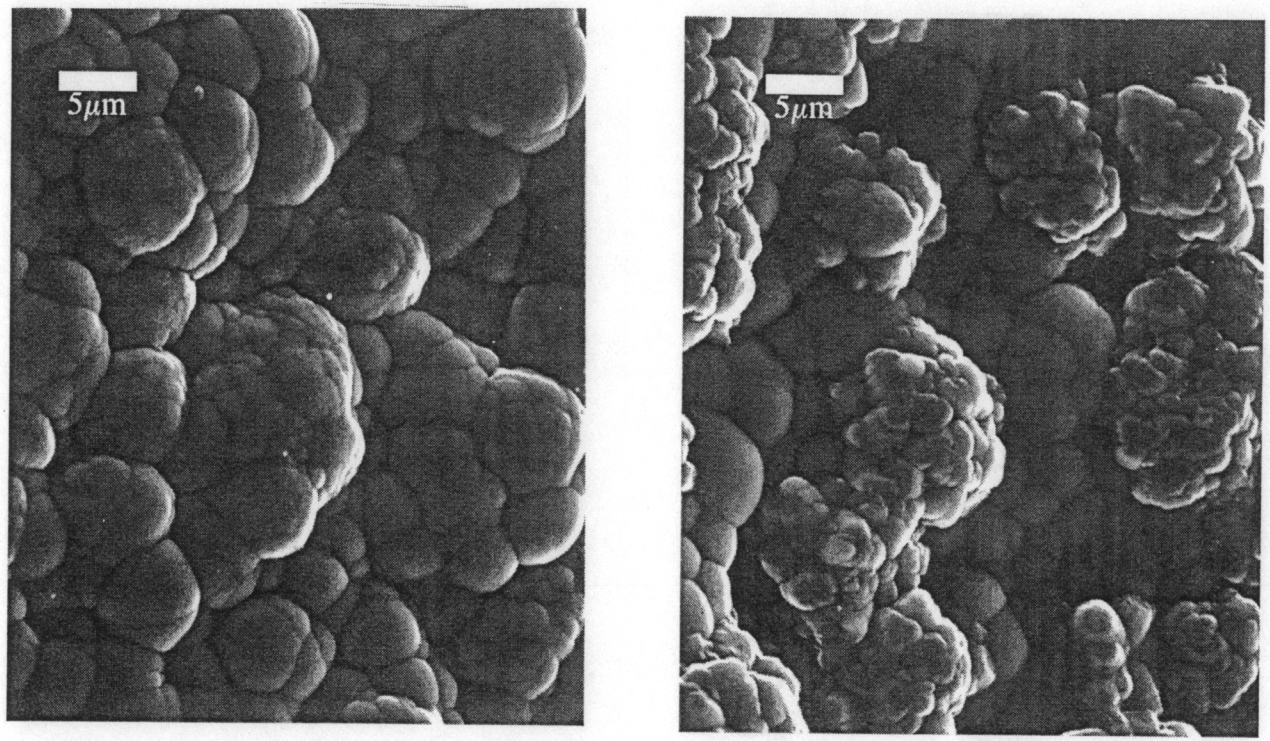

Figure 35. Scanning Electron Micrographs of HfB_2-SiB_4 Coating Showing Development of Second Phase Clusters

type growths. Figure 36 shows the presence of faceted and domed grains that are assumed to be HfB_2 and SiB_4, plus a third type of morphology not previously identified. Figure 37 shows that these "fuzzy" growths appear to be associated with the faceted crystals on these coatings.

The concentration gradients described previously can produce not only microstructural variations across the substrate, but during two-phase deposition, compositional gradients were also observed. Figure 38a shows a distinct color change at low magnification. At higher magnification in 38b, the transition region between the two areas shows that small "islands" of the darker phase rapidly coalesce, eventually forming a continuous layer of this phase. (Micro-Raman spectroscopy performed at the Naval Research Laboratory has indicated that the darker regions were SiB_4 and the lighter areas HfB_2.) Figure 39 shows the development of the (SiB_4) in this transition region. The x-ray maps in Figure 40 (from the electron microprobe at ORNL) prove that the faceted crystals are SiB_4 and the domed regions are HfB_2.

Figures 41 is the best example of two distinctly different morphologies existing together. The sharper, faceted grains have been tentatively identified as SiB_4, while the domed grains appear to be HfB_2. A higher magnification backscattered image of the faceted crystal is shown in Figure 42. The light and dark regions on the crystal surface seem to indicate that it could be a two-phase structure (as opposed to a ternary compound).

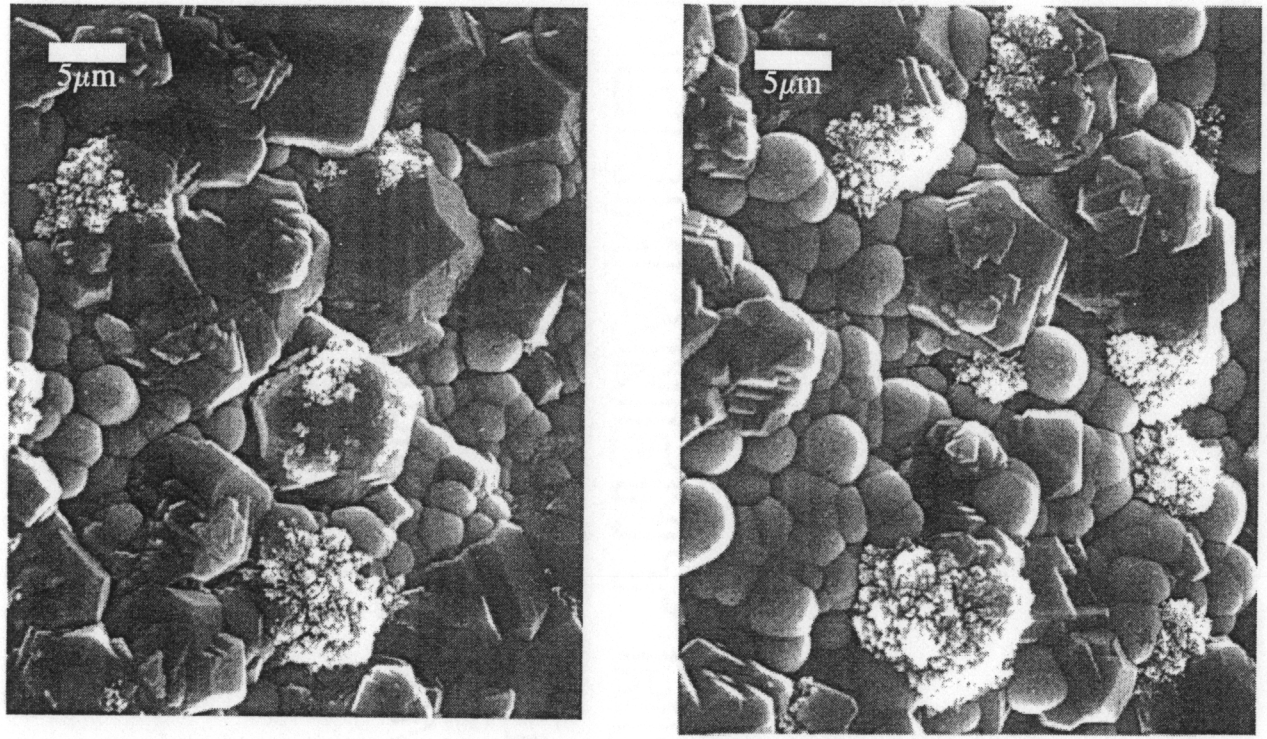

Figure 36. Scanning Electron Micrographs of HfB_2-SiB_4 Coating Showing Coexistence of Faceted and Domed Cluster Morphologies

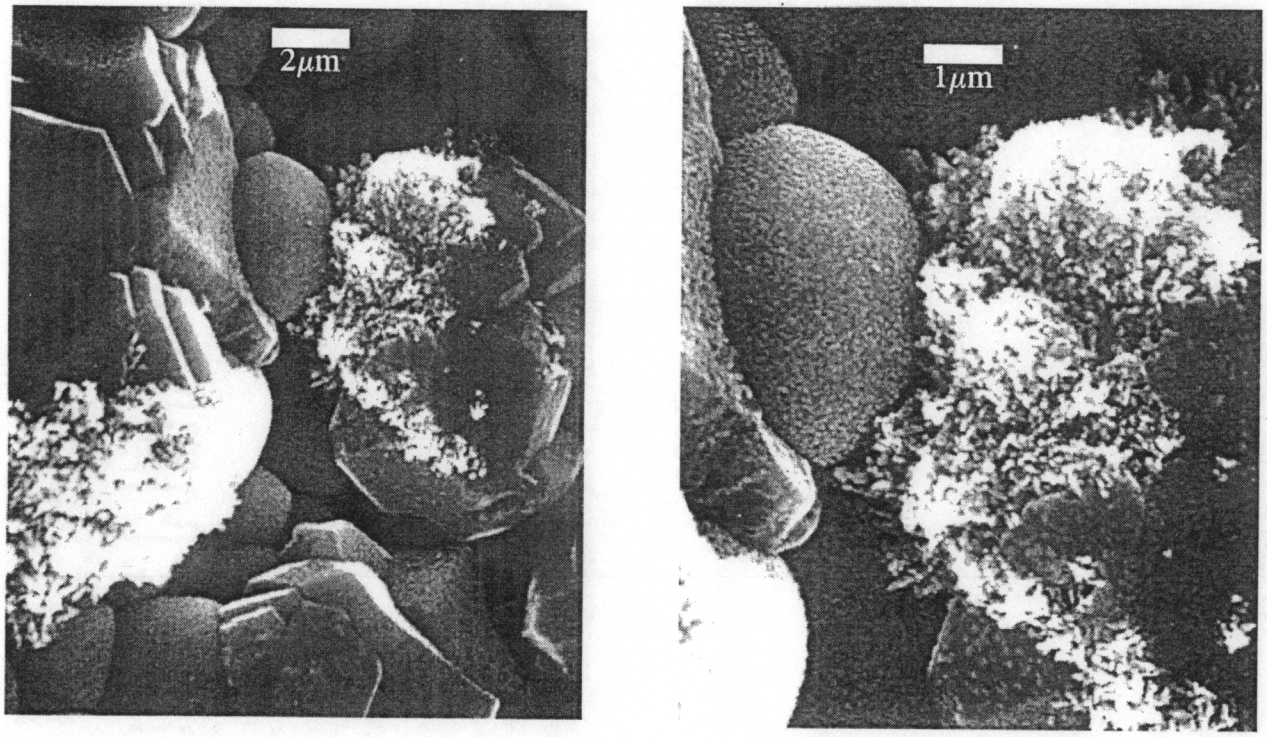

Figure 37. Scanning Electron Micrographs of HfB_2-SiB_4 Coating Showing Clusters Growing from Faceted Grains

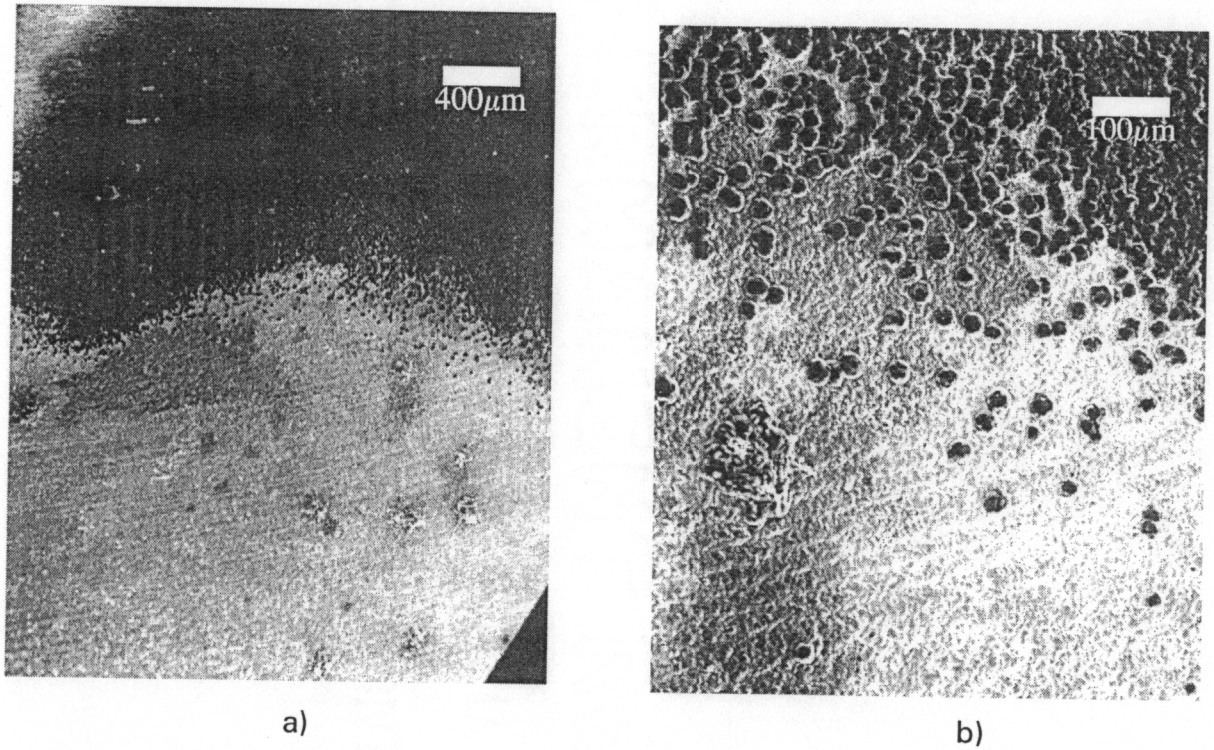

Figure 38. Scanning Electron Micrographs of HfB_2-SiB_4 Coating Showing a) Dark and Light Colored Surfaces and b) Transition Region at Higher Magnification

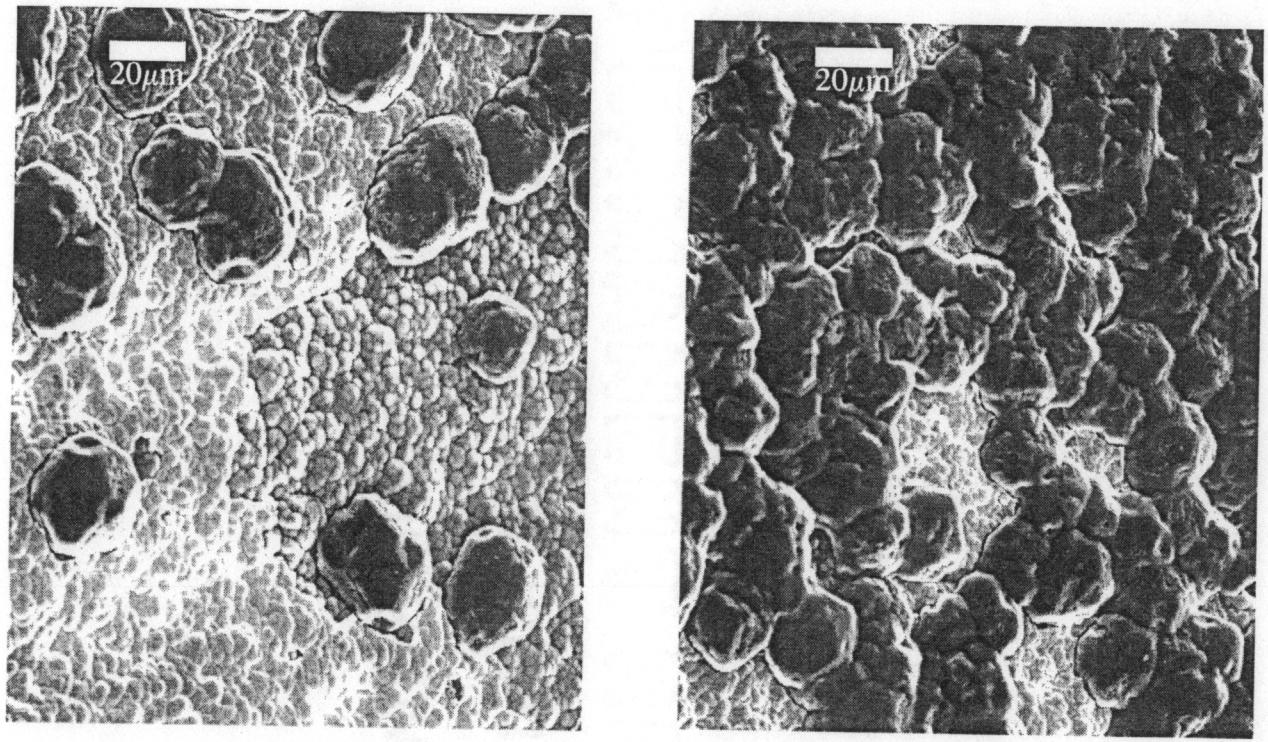

Figure 39. Scanning Electron Micrographs of HfB_2-SiB_4 Coating Showing Development of Darker Phase

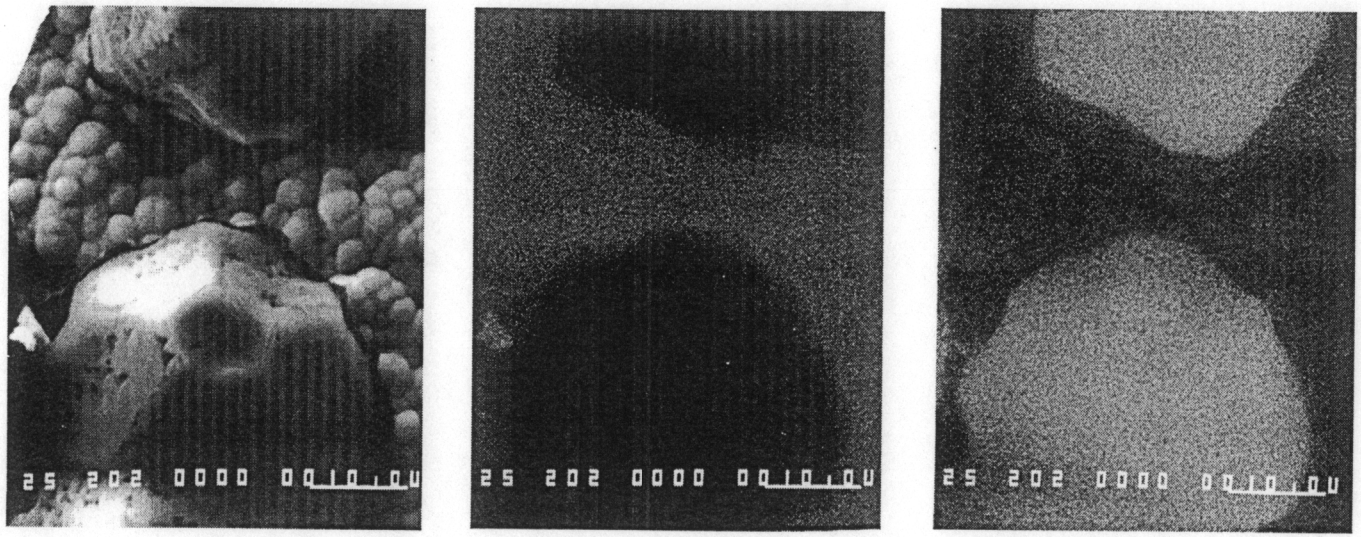

a) b) c)

Figure 40. a) SEM image, b) Hf x-ray map, and c) Si x-ray map of HfB_2-SiB_4 coatings

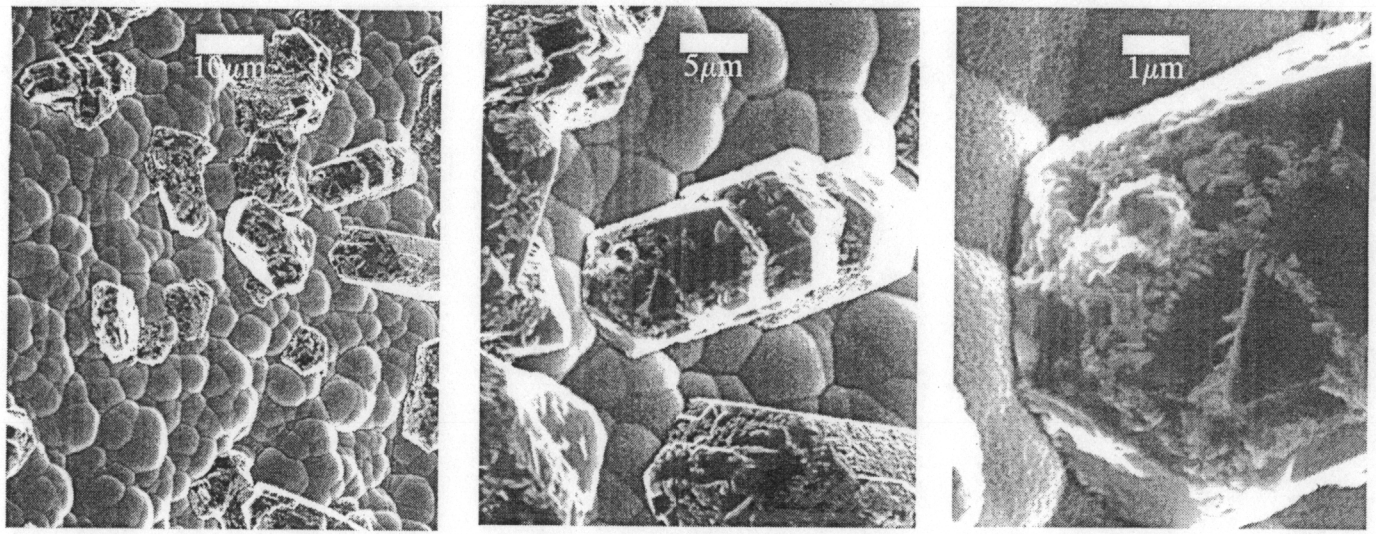

Figure 41. Scanning Electron Micrographs of HfB_2-SiB_4 Coatings Showing Coexistence of Faceted SiB_4 and Domed HfB_2 Morphologies

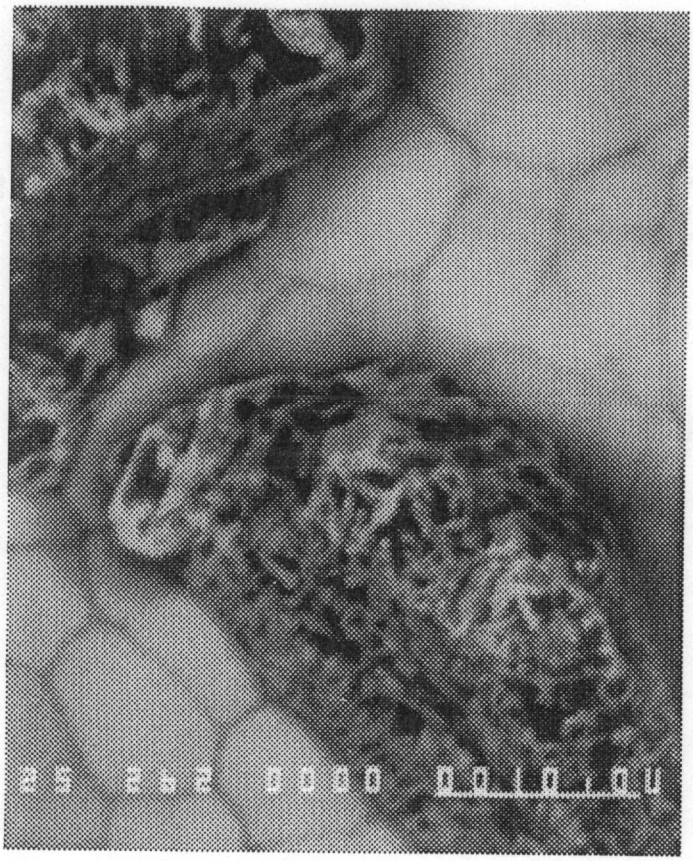

Figure 42. Backscattered Electron Image of Faceted Crystal on Domed Primary Coating, from HfB_2-SiB_4 Coating

Electron microprobe x-ray maps indicate that both Hf and Si are present, but quantitative analysis was inconclusive. Figure 43 shows yet another example of a two-phase structure. In this case, micon-sized platelets of a lighter second phase are growing from the underlying coating. Figure 44 shows this coating at higher magnification, where the base material seems to have a scaly surface, and the smaller platelets appear to be embedded in that material. The results from the electron microprobe x-ray maps, shown in Figure 45 show that the lighter colored platelets are HfB_2, and the darker base coating is SiB_4.

A final example of multiphase structures produced in this study is shown in Figure 46. Two different-sized second phase crystals are seen to be on a domed-morphology primary phase. Figure 47 shows this larger growth (about 100 μm across, with a spiral-dislocation growth surface) both as an individual grain and growing with other grains. The Si x-ray map from the electron microprobe show that these crystals are more Si-rich, and are likely SiB_4. Figure 48 shows the smaller second-phase crystal at higher magnification. A highly faceted growth surface is seen, indicating that it is not the same as the larger growths shown in Figure 47. Quantitative analysis using the electron microprobe showed that a smaller amount of silicon is present. This leads to the speculation that the balance is boron (no hafnium was detected), suggesting that this phase might be SiB_6.

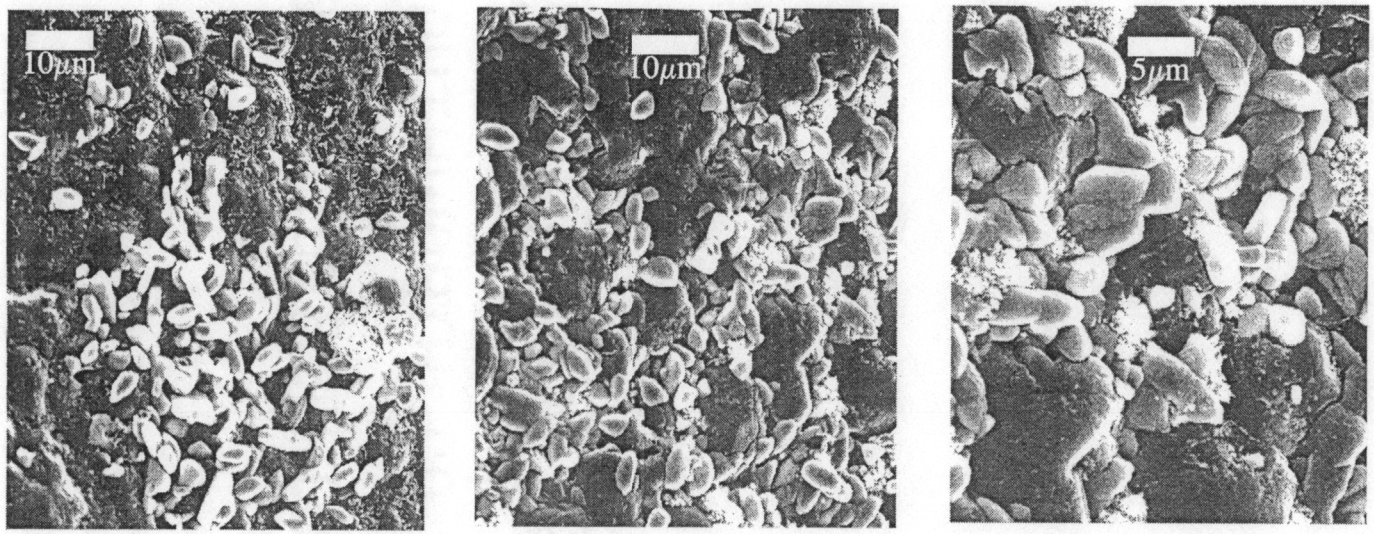

Figure 43. Scanning Electron Micrographs of HfB_2-SiB_4 Coatings Showing Two Different Morphologies

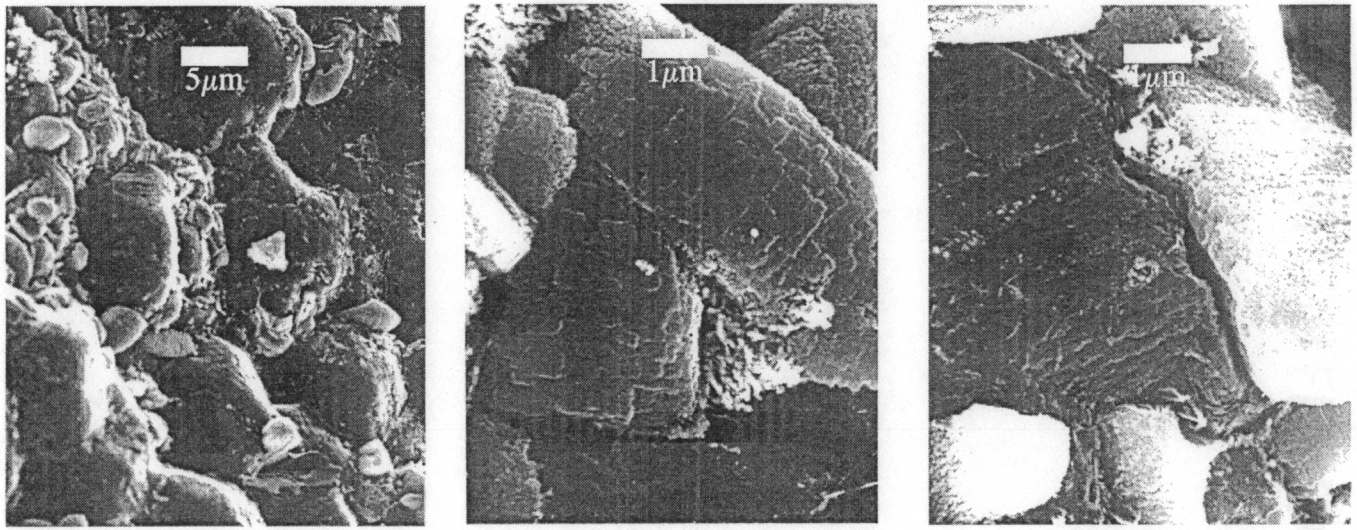

Figure 44. Scanning Electron Micrographs of HfB_2-SiB_4 Coating Showing Coexistence of Two Different Morphologies

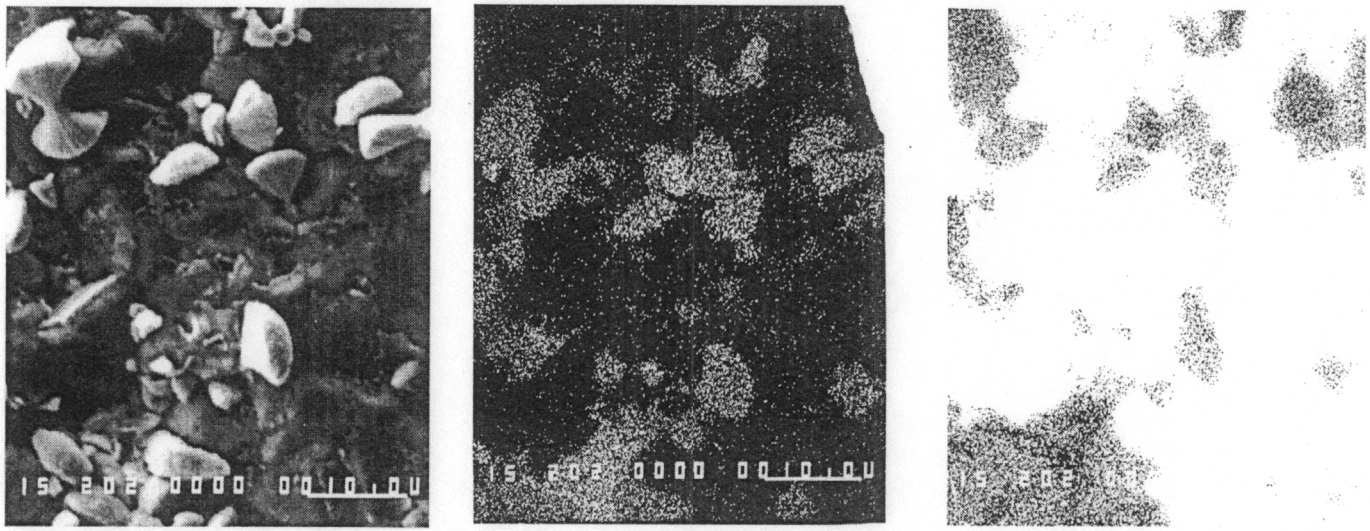

a) b) c)

Figure 45. a) Scanning Electron Micrograph, b) Hf X-Ray Map, and c) Si X-Ray Map of HfB_2-SiB_4 Coating Showing that Small, White Crystals are HfB_2, and Continuous Dark Phase is SiB_4

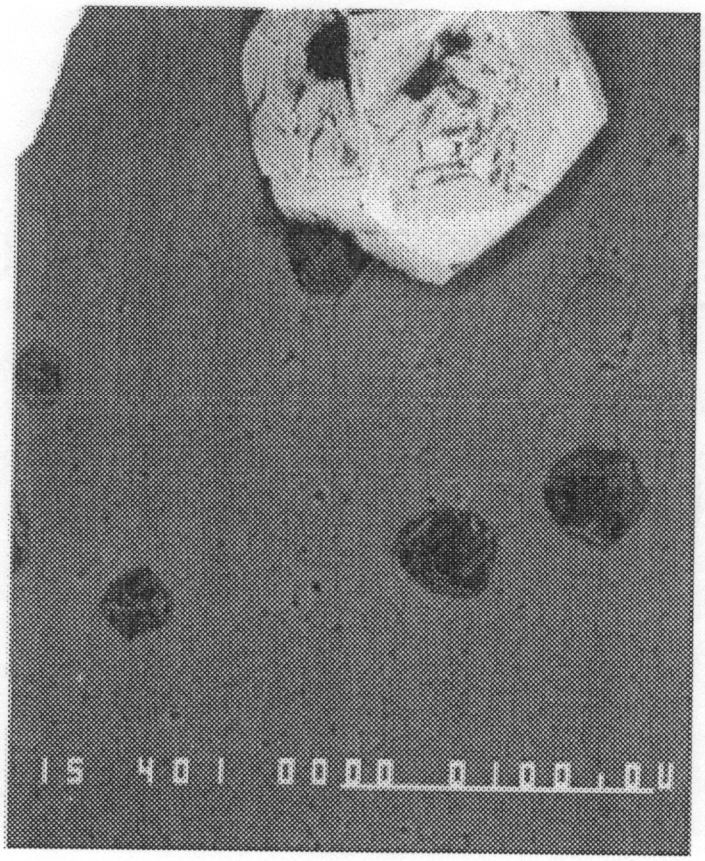

Figure 46. Backscattered Electron Image of HfB_2-SiB_4 Coating Showing Two Different-Sized Faceted Crystals on the Domed Primary Phase

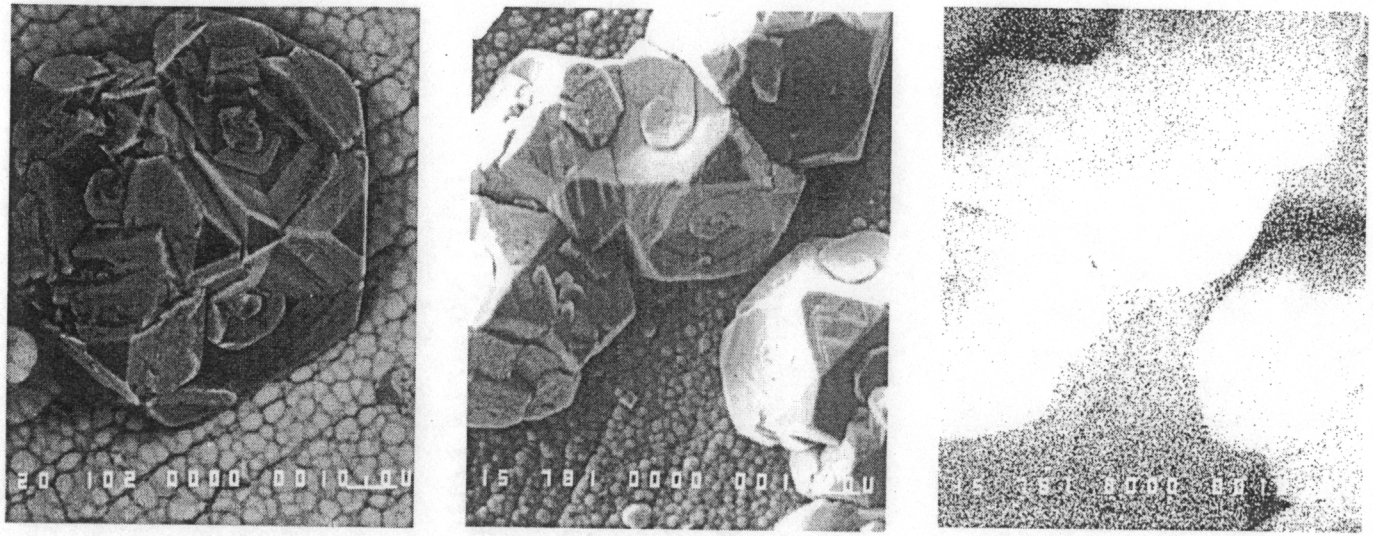

a) b) c)

Figure 47. a), b) Scanning Electron Micrographs and,c) Si X-Ray Map of HfB_2-SiB_6 Coating, Showing Faceted Second Phase on a Columnar, Domed Continuous Phase

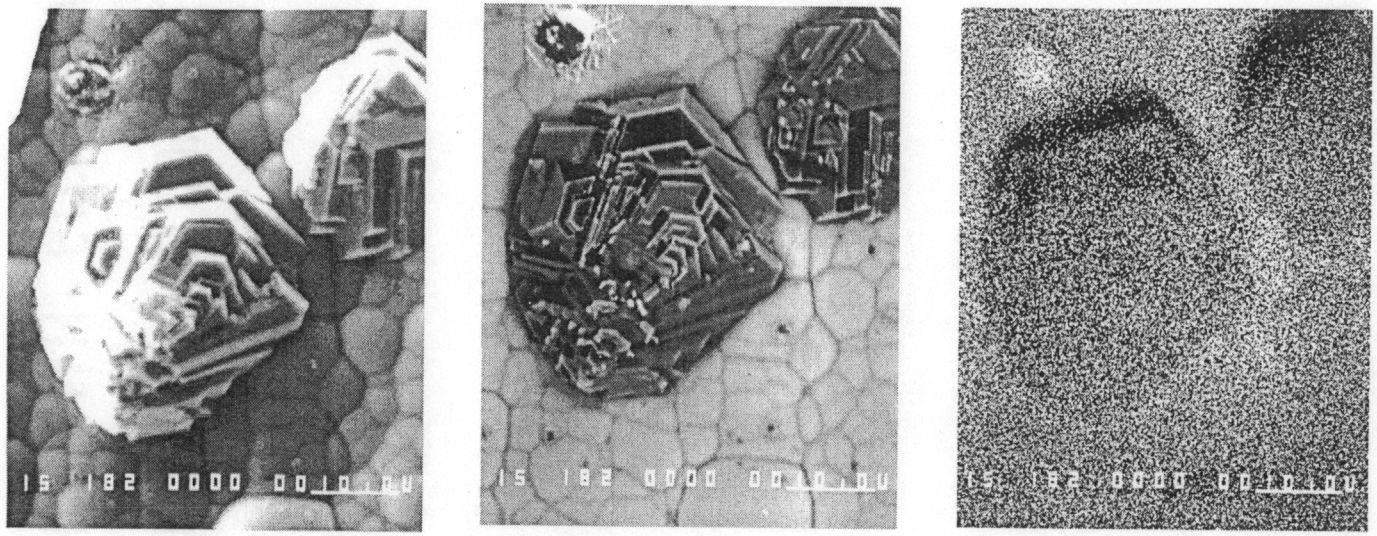

a) b) c)

Figure 48. a) Scanning Electron Micrograph, b) Backscattered Image, and c) Si X-Ray Map of HfB_2-SiB_6 Coating, Showing Highly Faceted Second Phase on a Columnar, Domed Continuous Phase

3.7 Discussion of CVD Results

In addition to the role of thermodynamics in CVD reactions covered in Section 3.1.2, a more complete understanding of CVD reactions requires a basic knowledge of fluid flow, mass transport, chemical kinetics, and crystal nucleation and growth. In Section 3.7.1, the effects of mass transport and chemical kinetics on the rates of deposition processes will be discussed. With one of the main focuses of this research being the study of the microstructural features of the deposit, the processes of nucleation and growth during the CVD process, along with the influences affecting microstructural development will also be reviewed in Section 3.7.2. Uniformity and adherence issues will be discussed in Section 3.7.3. Finally, in Section 3.7.4, the results from the present deposition studies will be analyzed based upon the the knowledge gained from the literature review, thermodynamic modeling, and the discussion of factors affecting the coating microstructure and properties reviewed in the first three parts of this section.

3.7.1 Kinetics and Mass Transport Issues During CVD

The study of diffusion and chemical kinetics in CVD reactions is grounded in classical mass transport and reaction rate theory. The importance of diffusion principles in CVD was demonstrated in the 1950's, while Arrhenius-type correlations in CVD reactions had been established in the early 1900's. The application of these principles is greatly aided by the

boundary layer model described previously.

It is well established that the slowest step of a sequential process will control the rate of that process. From Spear's model, there are two possible rate limiting mechanisms in the CVD process; the diffusion of gases to and from the substrate through the boundary layer (Steps 2 and 6), or the rate of the chemical reaction at the substrate surface (Steps 3,4, and 5, since adsorption and desorption are not uncoupled from the actual chemical reaction for this analysis). The deposition rate is thus influenced by the presence and thickness of this boundary layer, whose characteristics are controlled by the temperature, total system pressure, input gas concentrations and flow rates. The deposition kinetics for producing compounds, alloys, and mixtures are commensurately more complex due to the multiple reaction paths possible.

Under equilibrium conditions, all reactant species are consumed during the deposition reaction, resulting in a perfectly efficient deposition process[101]. At equilibrium, the thermodynamic calculations accurately predict the phases, rates, and efficiencies of the deposition process. This limit (maximum rate and efficiency) is enhanced by a prolonged residence time for the gas in the reaction zone, in comparison to the diffusion or chemical reaction rates.

Growth rates in CVD processes depend, in general, on temperature, as

shown in Figure 49. Two temperature regions can be identified; a high temperature region with a weak temperature dependency, and a low temperature region with a strong temperature dependency. At the lower temperatures, the deposition rate is found to be controlled by slow chemical reaction rates. As a result, increasing temperature has a strong influence on the deposition rate. For endothermic deposition reactions (with the reverse exothermic reaction), the relationship between temperature and growth rate, **G**, can be represented by the Arrhenius equation,

$$G = G_0 \exp(-\frac{\Delta E}{kT})$$

where G_0 is a pre-exponential factor, ΔE the activation energy, k the Boltzmann constant, and T the substrate temperature[102]. At some temperature, the slope of the line (ln rate vs. 1/T) changes, indicating a change in rate-controlling mechanism. Because the diffusion coefficient varies slowly with temperature in comparison to the chemical kinetics, any reactant that is transported to the substrate reacts immediately, limiting the increase in growth rate with temperature. The result is a smaller temperature dependence, viewed graphically on the Arrhenius plot as a less steep slope[103].

At a given temperature, these control mechanisms are differentiated by their dependence on reactant flow rates. While diffusion limited reactions

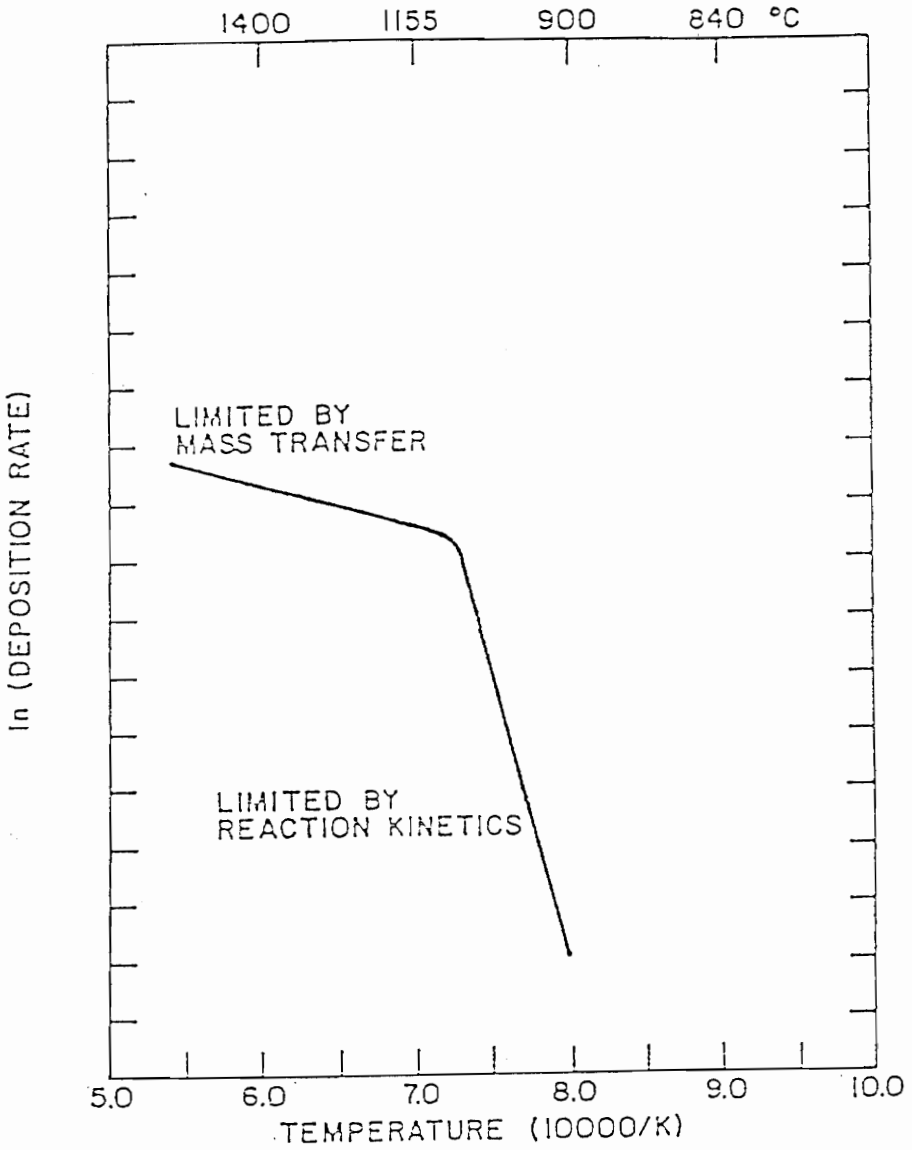

Figure 49. Typical Temperature Dependence of Deposition Rate

are found to have a weak dependence on temperature, they have a stronger dependence on flowrate. Figure 50[104] shows that increasing the flowrate at low flows produces an increase in the deposition rate. At higher flowrates, further increases in flow do not change the deposition rate, indicating a change in rate controlling mechanism from diffusion to kinetic control.

The effects of temperature and pressure on CVD reactions are not easily separated, so generalizations about extreme cases will not hold at intermediate values, where these effects are more interrelated. Simplistically, at low temperature and pressure, the reaction at the surface is slower than the diffusional steps. Under these conditions, the large diffusion coefficients and thin boundary layer contribute to the building up of a surplus of reactants at the substrate surface, which causes the reaction to be kinetically controlled[30,59]. Increasing the temperature influences the interface reaction more dramatically than it does diffusion, so the reaction becomes transport limited. Diffusion limited behavior is very sensitive to total system pressure. At high pressures and high gas velocities, the boundary layer is thicker, making it more difficult for reactants to reach the surface. The diffusivity of a gas is related to its pressure. Lowering pressures from one atmosphere to one Torr increases the diffusion rates by two orders of magnitude. (The longer mean-free-path is the reason CVI is done at low pressures, to allow the complete infiltration of the fiber preform before

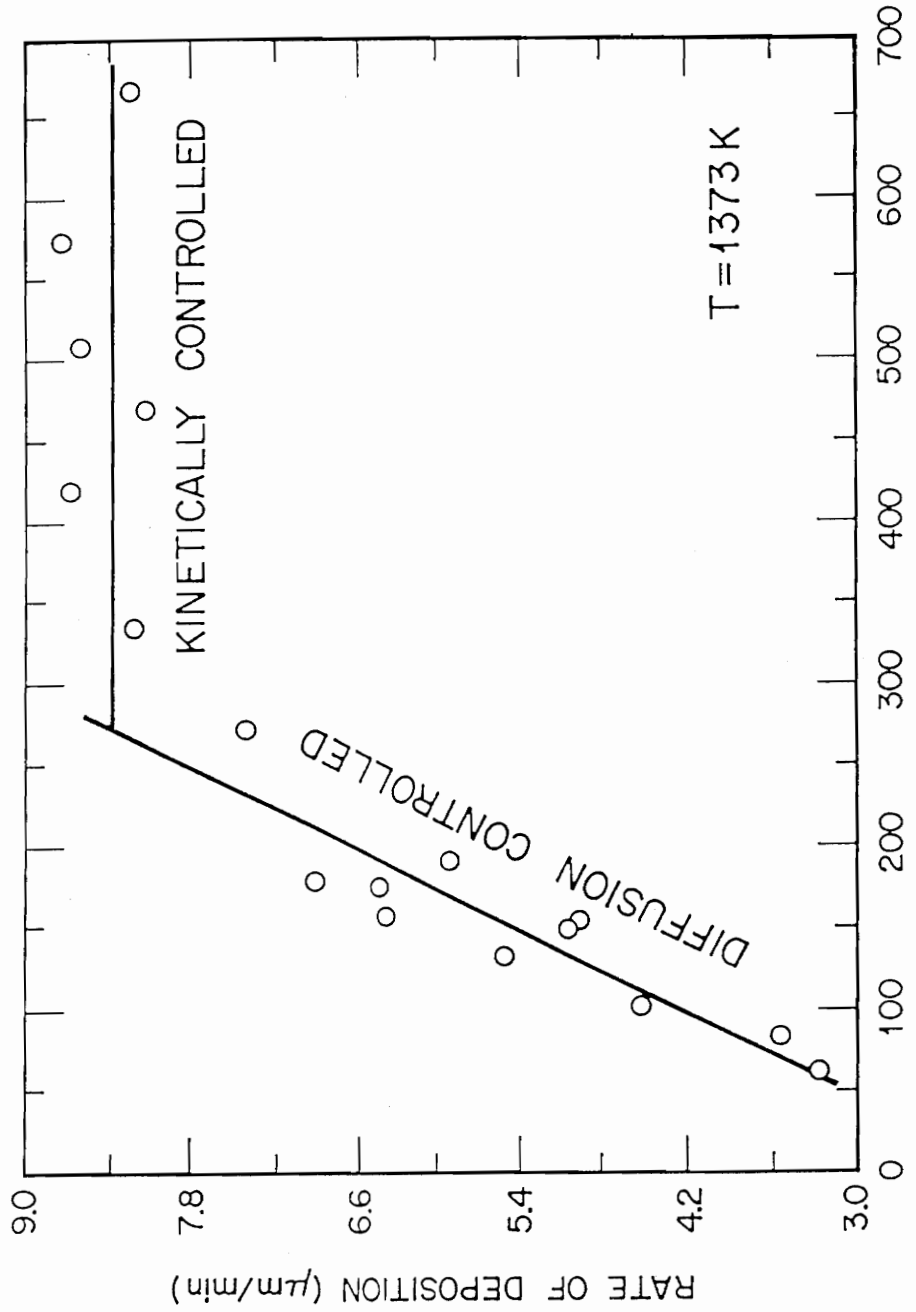

Figure 50. Typical Flow Rate Dependence on Deposition Rate[82]

deposition takes place.) The gas flux through a stagnant boundary layer of thickness δ can be defined as

$$J = -D \frac{P_i - P_{io}}{\delta RT}$$

where P_i is the vapor pressure of the ith species in the bulk gas, P_{io} is its vapor pressure at the substrate surface, R is the gas constant, T is temperature, and D is the diffusivity[31]. Since D varies inversely with pressure, gas mass-transfer rates can be increased by reducing pressure. By lowering the total system pressure, mass transport issues become less critical. The decomposition of the reactant gases is also higher at high temperatures, so any molecule that makes it to the substrate surface will react immediately.

3.7.2 Microstructural Development - The Nucleation and Growth of Films

For a large majority of phase transformations, the factors that control the kinetics of the reaction can be described by two processes - nucleation of the new phase and growth of the nuclei. At the equilibrium temperature, the free energies of the phases are equal. The formation of the new phase is caused by fluctuation due to thermal excitation or concentration gradients, which force the atoms to new positions corresponding to the product phase. When a sufficient number of atoms have combined to reach a critical size, they become stable and are termed nuclei of the secondary phase. Some nuclei do not reach critical size and disappear[105]. This is known as nucleation, and is common to all types of phase transformations, including solid-solid polymorphic transformations, as well as solid-liquid, liquid gas, and solid-gas transformations. Therefore, the formation of thin films from a gaseous precursor will follow a nucleation and growth process.

Nucleation can be homogeneous or heterogeneous. Homogeneous nucleation is rare in solid state transformations because of the many heterogeneities in composition and structure that are present. However, in gas phase reactions, like CVD, high gas concentrations and temperatures increase the frequency and energy of collisions between the atoms and molecules. Homogeneous formation of the reaction product, in the form of a

solid precipitate, is not desired for depositing a film onto a substrate. To produce a film on a substrate, heterogeneous nucleation utilizes the lower free energy offered by forming the nuclei on a surface. In this manner, the number of atoms needed to form a critical nucleus smaller than for homogeneous nucleation. After the initial nuclei are formed, impinging atoms are incorporated into the growing clusters to form a film[31].

Three basic growth modes have been postulated to describe film growth, and are shown in Figure 51. Island growth occurs when the nuclei grow in a three dimensional fashion to form islands, which eventually impinge upon one another to form a continuous film. This type of growth occurs when the arriving atoms are more tightly bound together than to the substrate. During Layer growth, nucleation has been suppressed, and a planar sheet grows two-dimensionally from the nucleus. The most important example of this type of growth mode is the single-crystal epitaxial growth of semiconductor films. The Stranski-Krastanov mechanism is a combination of the island and layer theories[31]. Figure 52[106] shows the initial stages in the development of an SiC film, from the nucleation of small clusters, through the coalescence into a continuous film.

The same conditions that control the rate of deposition (temperature, pressure, reactant partial pressures, boundary layer thickness) also influence the microstructural development of films. The two most important factors

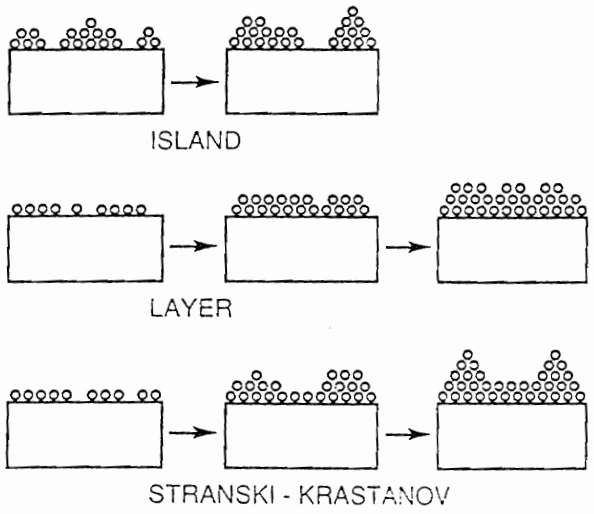

Figure 51. The Basic Modes of Film Growth[31]

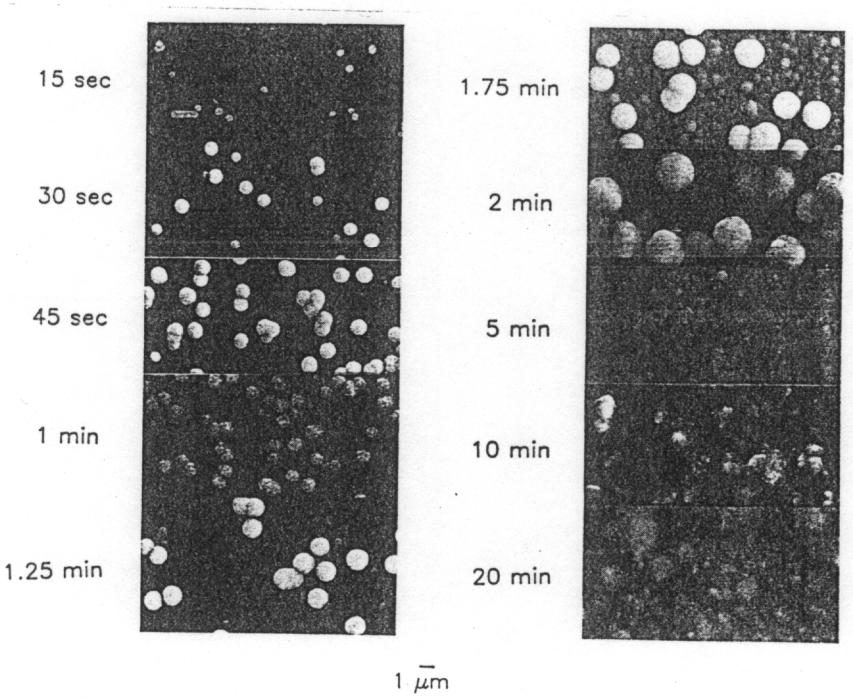

Figure 52. Scanning Electron Micrographs Showing Development of Morphology of SiC Films[84]

controlling the structure of the film, however, are vapor supersaturation and temperature. Supersaturation is defined as the ratio of partial pressure of the reactant gas adjacent to the substrate surface to its value in equilibrium with the substrate[32]. There is a wide variety of deposit structures obtainable by CVD. In Section 1.5, continuous films (amorphous, single crystal, and polycrystalline), whiskers, and powders were discussed as the macroscopic morphologies attainable by CVD reactions. The conditions favorable for formation of these structures have been reviewed by Blocher[93] and Bryant[32], and are shown schematically in Figure 53. In general, it is seen that the effects of supersaturation and temperature are opposite; increasing one has the same effect as decreasing the other. Ohring[31] shows that when depositing silicon from silane, temperatures below 600°C favor amorphous film formation, slightly higher temperatures produce columnar deposits, with larger crystallites developing at greater temperatures, where at 1200°C, epitaxial growth is produced. The conditions necessary to produce these structures will be discussed in greater detail.

Epitaxial growth is the extended single-crystal film formation on top of a crystalline substrate. The structural perfection of single crystal films is needed for electronic device applications, where stacking faults, twins, and dislocations have adverse affects on device performance. For most CVD reactions, the form of the substrate does not have a major effect on the

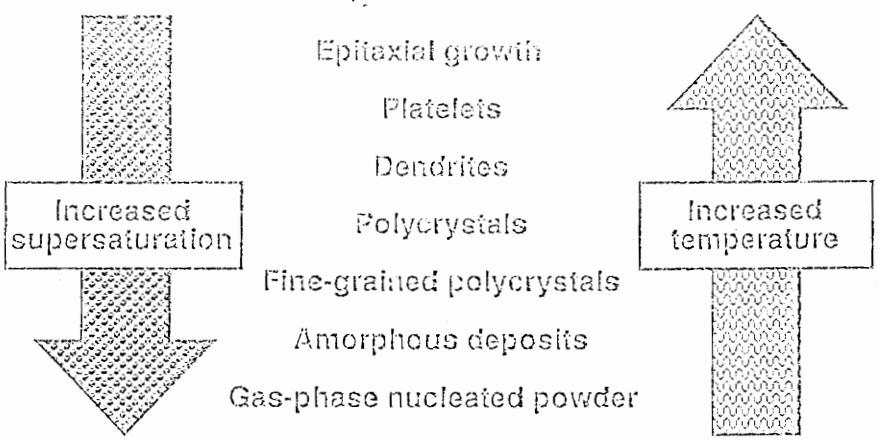

Figure 53. Effect of Processing Conditions on Microstructure[32]

structure of the film produced during deposition, but in epitaxial growth, there needs to be some lattice coherency between the film and substrate that results in a lower interfacial energy for that orientation than for randomly oriented crystals. Homoepitaxy refers to the growth of a film on a substrate of the same material. Heteroepitaxy refers to the growth of a film on a different material that has similar lattice parameters to the desired film. The formation of a single-crystal film is enhanced by high temperatures and low gas supersaturations. The film grows by lateral step movement, where the incoming atoms can diffuse to preferred low energy positions at lattice sites. The high temperatures allow atom diffusion to the preferred sites, while the low supersaturation suppress the formation of additional nuclei. With an increase in growth rate or temperature, the atoms do not have time to diffuse to the lower energy sites, causing the nucleation of new crystals. The thermodynamic aspects of nucleation have been covered in Section 3.1.

For polycrystalline deposits, there are three basic types of microstructures possible. As seen schematically in Figure 54, these include columnar, faceted, and equiaxed grains. For large supersaturations, large amounts of reactants are available at the substrate surface, so nucleation is rapid. This produces a fine, randomly oriented grain structure, with growth rates determined by diffusion and kinetic considerations.

At high supersaturations and high system pressures, polycrystalline

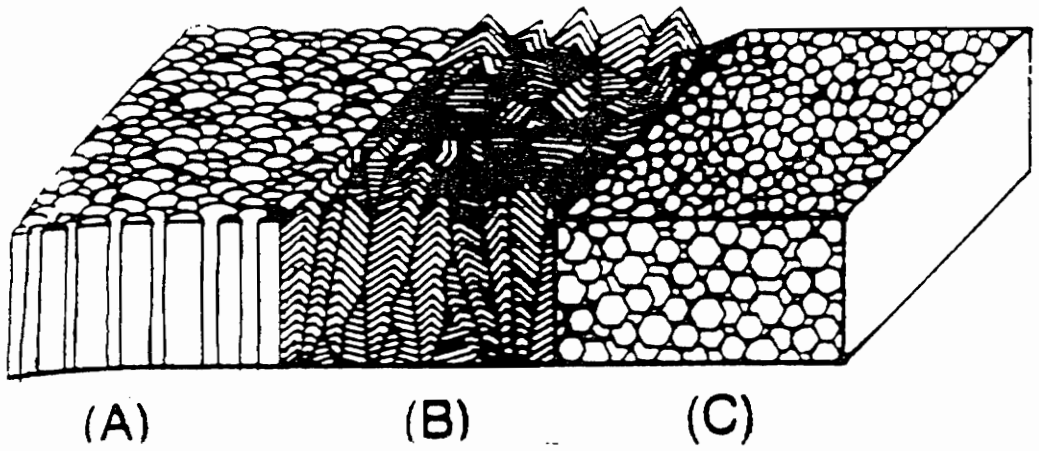

Figure 54. Schematic Representation of Coating Microstructures Deposited by CVD a) Columnar Grains with Domed Tops; b) Faceted, Columnar Grains; and c) Equiaxed Grains[34]

deposits are formed at low temperatures. Columnar grains, with some preferred orientation, develop with further growth, even though the original substrate and initial nuclei were randomly oriented. This is due to the preference of certain low-energy, close-packed planes during growth. Therefore, while randomly oriented crystals are commonly produced by CVD for very thin films, thicker films tend to develop a columnar morphology, making it the most common CVD microstructure. The columnar morphology can have a domed (Fig. 54a) or faceted (Fig. 54b) surface, with the domed structure resulting from low supersaturations and rapid surface diffusion, and the faceted surface develops from higher supersaturations and limited surface diffusion. In extreme cases, the preferred orientation can be such that the last layers to form are practically single crystal. Figure 55[107] shows how these large grains can develop from an originally fine-grained structure. The mobility of the adsorbed species increases with increasing temperature, producing a decreased nucleation density and increased growth rate. These factors cause a coarser grain structure to be deposited.

For some instances, where high strengths in the plane of the coating are desired, the columnar morphology would be detrimental. To reduce the development of this microstructure, very high supersaturations are required to reduce surface diffusion and thus keep the atoms from finding preferred lattice sites. If the supply of new atoms is rapid enough to renucleate

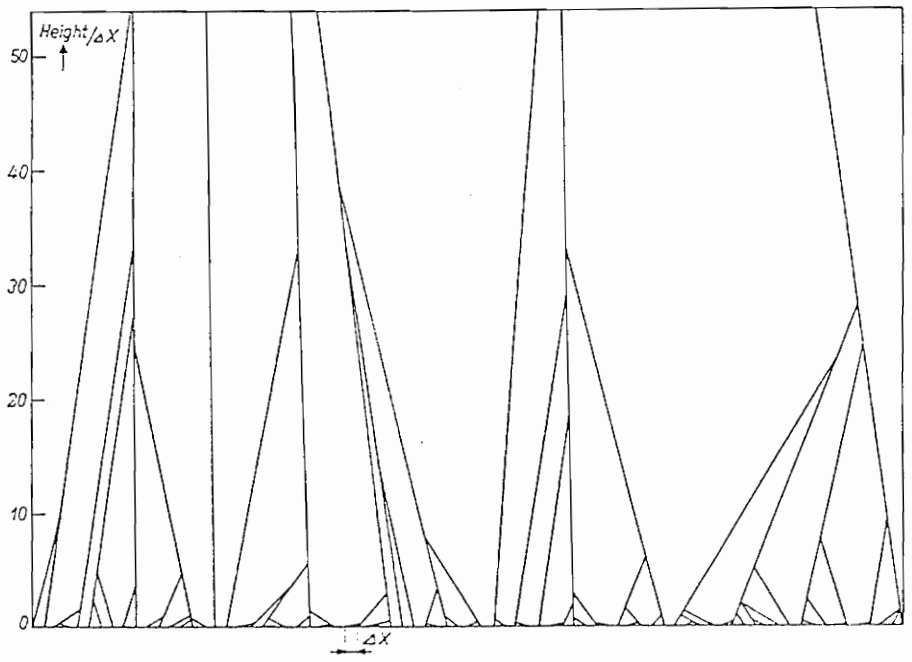

Figure 55. The Evolution of Columnar Microstructures During CVD[85]

grains, a finer, equiaxed crystal structure (Figure 54c) can result. If temperatures are low enough where mobility is lowered but supersaturation is large, the atoms tend to "stay where they are" instead of moving to more favorable sites, causing amorphous deposits to result.

A number of approaches have been tried to enhance the renucleation of grains in growing films. The controlled precipitation of powder incorporated into a growing film[108], Figure 56, can cause renucleation, but growth rate and porosity are adversely affected. Mechanically distorting the surface during deposition (by brushing or scratching[39]) supplies energy to the surface to lower the activation barrier for new nucleation, but isn't practical for commercial applications. The co-deposition of a second phase, however, has been successfully demonstrated to enhance renucleation, and is one of the reasons that two-phase deposits are the focus of the present investigation.

There are two possible cases where non-uniform film growth can be the desired outcome of the deposition reaction. These are powder production and whisker (or platelet) growth. The gas-phase formation of powders results from high reactant concentrations and gas temperatures. The greater frequency of collisions result in homogeneous nucleation in the gas phase, as mentioned previously. While this is desirable if the production of powders is the goal, this can be a problem when trying to make uniform

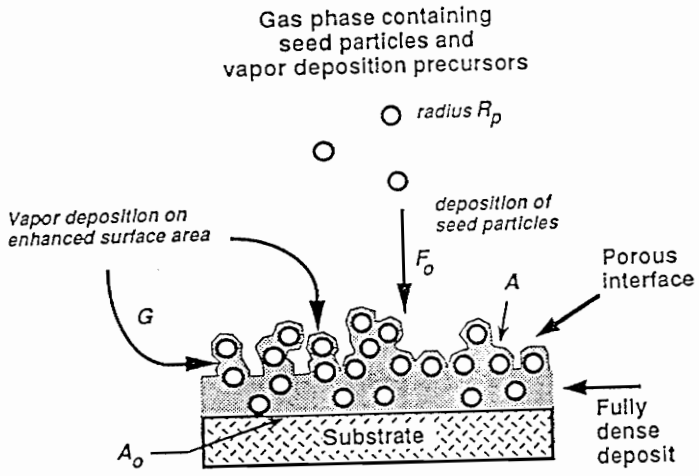

Figure 56. The Integration of Descrete Particles into the Growing Film[Ref]

coatings. Equipment maintenance problems can also result.

The second case is the growth of whiskers or platelets on a substrate. When film growth is controlled by the diffusion of atoms through the boundary layer, a reactant concentration gradient exists perpendicular to the substrate surface. This gradient is not a problem when the boundary layer thickness is constant across the substrate. However, when some irregularities exist on the substrate surface, protrusions into this gradient will experience preferred growth due to the greater flux of reactant atoms available[30,78], producing an non-uniform growth from the substrate at surface irregularities . The whisker-like growth can be the result of design[67,109], or due to unclean or unpolished substrates[110]. The orientation of the whiskers has been modeled by Sears, showing (Fig 57) how the growth direction can constantly change to produce the felt-like growths seen by some researchers. The growth of these whiskers are enhanced by thinner boundary layers, with higher pressures and lower flowrates also enhancing exaggerated growth[110]. The growth of non-uniform coatings, such as the platelets and whiskers shown in Figure 58, can have performance benefits, such as the reduction of surface reflectivity and emmisivity[111].

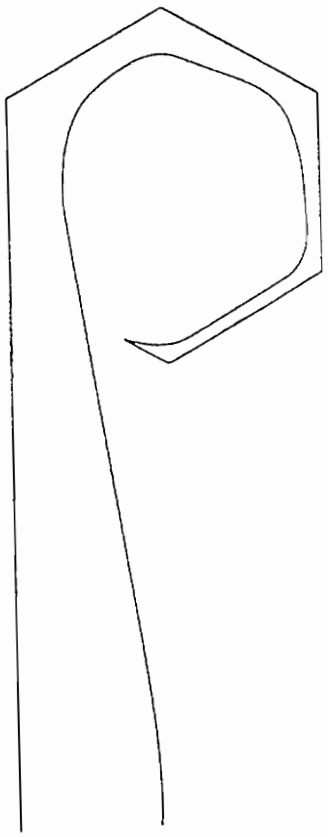

Figure 57. Hook-Shaped Whisker Formed by Repetitive Change in Growth Direction[89]

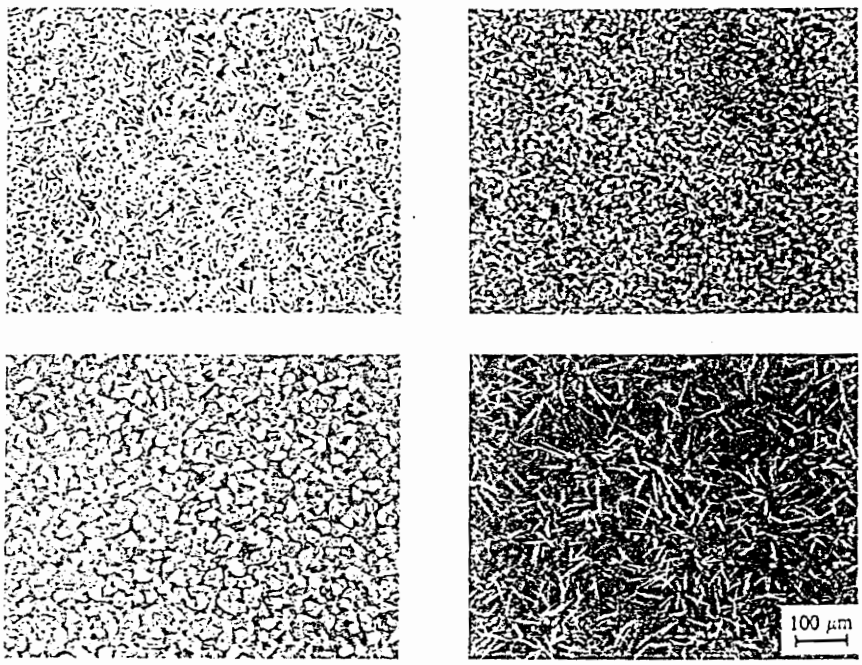

Figure 58. Scanning Electron Micrographs of Textured Surfaces Deposited by CVD[91]

3.7.3 Uniformity and Adherence of CVD Coatings

As introduced above, coating uniformity can be a problem that needs to be addressed. While controlling the deposition parameters and polishing the substrate will help to avoid the formation of large disperities, highly uniform coatings require special techniques. Since the substrate area closest to the gas injector port will receive the greatest flux of unreacted gases, a number of techniques have been developed to compensate for the concentration gradient to obtain uniform coatings. These include modification of the gas flow by mixing, stirring, or pulsing[112], limiting reactant conversion per pass (which will hinder efficiency and deposition rate), compensation for concentration gradient with a temperature or flow cross section gradient (the latter will increase gas velocity), or mechanically rotating the substrate during deposition. The control of deposition rate and uniformity is especially important for electronics and composites applications. During infiltration of fiber preforms to produce composites, high deposition rates or uneven deposition will close the pore channels through the fiber preform, stopping the infiltration process and leaving large pores in the structure. The different diffusivities of the gas species for each element in the compounds and mixtures make uniformity difficult to achieve.

The adherence of the coating to the substrate is also critical to coating performance. If the coating spalls or cracks, it can no longer fulfill its

function. The ability to withstand both in-service mechanical and thermal cycling stresses is affected by the condition of the interface between the coating and substrate and the thermal expansion mismatch between the materials. The formation of voids or a powder deposit due to gas phase nucleation or rapid deposition rates will weaken the interface between the film and substrate. The corrosion of the substrate surface by the reactant or product gases can also be a problem. To assure thermal cycling stability and good mechanical performance, interfacial films of one or more layers, or graded coatings can enhance bonding and reduce stresses due to thermal expansion coefficient mismatch.

3.7.4 DISCUSSION OF CVD RESULTS

The results of the x-ray diffractometry, showing that SiB_4 is the stable condensed phase in the Si-B-Cl-H system at the conditions used in these experiments, seem to suggest that the thermodynamic modeling predictions described in Section 3.1 were incorrect. One might conclude that the equilibrium calculations were erroneous due to either the omission of important species, inaccurate thermodynamic data, or some nonequilibrium process controlling the deposition reaction. The deposition of metallic silicon or boron, as predicted for the low pressures, high temperatures, and high hydrogen concentrations used in the experiments, was not seen at any deposition condition. Additionally, the preferred deposition of SiB_4 over SiB_6 is also not expected from the thermodynamic modeling. A discussion of the reasons for SiB_4 (instead of the predicted B, Si, and SiB_6 depositions) is given below.

$SiCl_4$ is stable up to only about 1000°C[113], above which the reaction

$$SiCl_{4\,(g)} + Si_{(s)} \rightarrow 2SiCl_{2\,(g)}$$

will eliminate the free silicon deposited on the substrate[114]. This subchloride can in turn react with either excess H_2 or HCl according to the reactions

$$SiCl_{2\,(g)} + H_{2\,(g)} \rightarrow Si_{(s)} + 4HCl_{(g)}$$

or

$$SiCl_{2\,(g)} + HCl_{(g)} \rightarrow SiHCl_{3\,(g)}.$$

The results of the thermodynamic modeling that predict a high partial

pressure for the chlorosilane suggest that the latter reaction is in equilibrium at the substrate surface. The deposition of elemental boron, as given previously, might also not be favored as written. Carlton[115] noted that in excess H_2, the reaction

$$BCl_{3\,(g)} + H_{2\,(g)} \rightarrow HBCl_{2\,(g)} + HCl_{(g)}$$

describes all the major gas species in equilibrium at the gas surface. He also noted that the rate limiting step for boron deposition was based upon this reduction reaction.

The fact that $SiCl_2$, $SiHCl_3$ and $HBCl_2$ would be the favored gas species at high temperatures during the deposition of elemental Si and B would agree with the analysis of Spear and Dirkx[86] for the deposition of the silicon borides. They found that $SiCl_2$ is the dominant silicon-bearing gas species at higher temperatures, while $SiHCl_3$ predominates at lower temperatures. $BHCl_2$ was found to be the main boron-containing gas species in the bulk gas up to 1500K, while BCl_3 predominates at the deposition surface at temperatures less than 1200K.

The deposition experiments of Spear and Dirkx[66] also produced the preferential deposition of SiB_4 over SiB_6, with higher temperatures needed to deposit the hexaboride. They suggest that in forming the compound, Si and B deposit "independently" and then react to form the boride. This suggests that equilibrium at the SiB_4 deposition surface cannot occur until the

temperature is high enough for equilibrium to be achieved in both the Si and B deposition reactions. An Arrhenius plot of their data showed that this occurs at 1400K. They conclude that at $T < 1400K$, the deposition of SiB_4 must be limited by the reaction kinetics of B deposition, which causes the boron-poor SiB_4 phase to be favored over SiB_6. At temperatures above 1400K, changes in local gas chemistry caused by the rapid depletion of B at the deposition surface (since SiB_6 is 86% B) produces a high concentration of $SiCl_2$ at the substrate surface. Therefore, in order to maintain enough B at the deposition surface, the diffusion rates of that specie would need to be much higher than that of $SiCl_2$ (in this diffusion-limited regime). They modeled the effects of $SiCl_2$ buildup, showing that the deposition will indeed shift from SiB_6 to SiB_4. (With the present investigation, using $SiCl_4$ instead of SiH_4 as the silicon-bearing reactant, this result is even more highly favored.) The deposition of free silicon and boron in the deposits was also found to be kinetically limited in their studies.

The deposition of whiskers, as described in Section 3.6.1 (Figure 18), while not a main focus of this work, provides some useful insights into the nucleation and growth topic. The very low flow rates used in that experiment, combined with the high pressures, probably caused low gas velocities through the hot zone. Depleted of reactants, there was probably not enough atoms of Si and B available after initial nucleation, causing the

few grains that had nucleated to grow at the expense of new nuclei. The morphology of these fibers is strikingly similar to that reported by Motozima[67], and it is therefore theorized that these fibers, like his, are SiB_4.

The deposition of both domed and faceted crystals, as shown in Figures 20 and 22, are common to CVD produced materials. As described in the previous section, higher gas concentrations and limited surface diffusion result in a faceted morphology, while low supersaturations and high surface diffusion rates lead to domed morphologies. The exaggerated growth of certain grains, shown in Figure 21, is likely due to an unclean or uneven substrate surface. As described previously, when an irregularity exists on the surface, it extends into the gas boundary layer at the growth surface. This protrusion will experience a greater flux of atoms, producing the irregular growths seen in Figure 21.

The deposition of HfB_2 required the in-situ generation of $HfCl_4$, where temperature and pressure control are critical for producing the desired specie. Several researchers have studied these reactions, and their results, as described below, were used in the present study.

Troyanov[116] and Ismailovich[117] have studied the formation of the hafnium chlorides, and found that at temperatures above 240°C, a reaction of hafnium tetrachloride with metallic hafnium to form hafnium trichloride occurs according to the reaction

$$2HfCl_{4\,(g)} + Hf_{(s)} \rightarrow 4HfCl_{3\,(g)}.$$

This species decomposes at 420°C by the reaction

$$2HfCl_{3\,(g)} \rightarrow HfCl_{4\,(g)} + HfCl_{2\,(g)}$$

to form the dichloride. Shinavski[118] determined that an average composition of $HfCl_{3.14}$ was produced at 350°C. In the present study, high flowrates of H_2 carrier gas reduce the exposure of $HfCl_4$ to the hafnium sponge and the low reaction temperature (400°C) likely keeps the lower chlorides from forming.

The analysis of the HfB_2 coatings produced similar results to that found in the SiB_4 deposition studies. Both domed and faceted microstructures (Figures 25 and 26) were produced in a similar fashion to that described for the SiB_4 coatings. Figure 24, however, is different to any SiB_4 coating produced during this study. This type of porous, powdery microstructure can result from a gas phase nucleation phenomenon. The resultant precipitate could fall onto the substrate surface and be incorporated into the growing film, as described previously (Fig 56). Another possibility for forming this type of microstructure is an extremely rapid deposition that doesn't allow the atoms to move into low energy lattice sites, producing the large intergranular voids. The extremely fine size of the spherical grains, however, would probably suggest that a gas phase reaction has taken place.

An analysis of the two-phase coatings show many of the same

features found in the single phase coatings, and are the result of the same factors influencing the microstructures of those deposits. Again, the difference between the domed and faceted crystals results from supersaturation gradients along the substrate surface. These concentration gradients are the product of the system design. Since the BCl_3 and SiB_4 need to be separated past the hafnium chlorination zone to the substrate surface, there is insufficient gas mixing necessary to produce uniform coatings. These gradients became especially noticeable during the two-phase deposition studies. Figure 38 shows that one side of the substrate is mostly SiB_4, while the other is mostly HfB_2. These microstructures thus reflect the concentration gradients both by having compositional and morphological changes across the substrate surface. These gradients might be eliminated by other furnace designs, or by physically rotating the substrate.

A narrower range of deposition conditions was used during the deposition experiments than employed during the thermochemical modeling. While the original plans of the investigation included high temperature and high pressure experiments, the limitations of the furnace tube (1300°C), as well as gas phase reactions and chloride precursor instabilities, made these extreme conditions unfavorable for deposition studies. Lower temperatures were found to produce prohibitively slow deposition rates.

3.8 Summary

- Two-phase HfB_2-SiB_4 coatings for high-temperature structural service in oxidizing environments were successfully deposited using chemical vapor deposition techniques from $HfCl_4$, $SiCl_4$, BCl_3, and H_2 precursors. There were no previous reports of this in the literature. (A patent for this work has been filed - Navy case # 77,033).
- Single phase HfB_2 and SiB_4 coatings were deposited under a variety of processing conditions from these precursors.
- A hot-wall chemical vapor deposition reactor was designed and constructed specifically to perform deposition reactions in this system.
- The special features of the CVD reactor include: a $SiCl_4$ bubbler, in-situ generation of $HfCl_4$, electronic pressure control using an argon ballast technique, electronic mass flow controllers, and an ice-water cold-trap and soda-lime exhaust scrubber.
- Thermochemical modeling of reactions in the Zr-Si-B-Cl-H system was performed using the SOLGASMIX computer program. The results of these calculations were used as a guide for the deposition of HfB_2-SiB_4 coatings.

3.9 CONCLUSIONS

- Scanning electron microscopy and electron microprobe analysis revealed a variety of microstructural features for the two-phase HfB_2-SiB_4 coatings. Several morphologies (fibrous, powdery, domed and faceted) were identified as being characteristic of HfB_2 or SiB_4. The differences in composition and morphology were determined to be greatly influenced by reactant supersaturations at the substrate surface, while temperature and total pressure effects were less sharp.
- A variety of microstructures were also produced for the single phase HfB_2 and SiB_4 deposits. Again, concentration gradients across the substrate surface appeared to have a greater influence on the microstructure than temperature or pressure.
- Deposition experiments showed that SiB_4 was the only phase obtained in the Si-B-Cl-H deposition system. Si, B, and SiB_6 deposition, while predicted by the thermodynamic modeling, was not favored due to etching reactions and mass transport issues. SiB_6 was predicted to be the preferred silicon boride phase.
- Separate alumina injectors were necessary to deliver BCl_3 and $SiCl_4$ directly to the hot zone to prevent reaction between them and inhibition of the hafnium chlorination reaction. This separation of the gases led to insufficient mixing, which in turn caused variations in coating

morphology and composition.

- The thermochemical modeling suggests that higher pressures and lower hydrogen concentrations should be better for producing two-phase boride coatings, with a wide range of processing conditions capable of producing the two-phase coatings. This implies that variety of compositions and microstructures can be deposited. While kinetic and design considerations caused the deposition experiments to be focused on a narrower range of conditions, a variety of microstructural features were revealed by SEM characterization for both the single and two-phase coatings.
- Microstructural characteristics could not be directly related to processing conditions, with both domed and faceted morphologies were deposited at the temperatures and pressures used in this study.

Appendix A

P=1 atm.
T=1100K
H/(Zr + Si + B + Cl)= 10

LEGEND

- ● ZrB_2
- ○ ZrB_2 + B
- ■ ZrB_2 + SiB_6
- □ ZrB_2 + SiB_6 + B
- ◆ ZrB_2 + SiB_3
- ◇ ZrB_2 + Si
- ▲ ZrB_2 + SiB_3 + Si
- △ ZrB_2 + SiB_6 + SiB_3

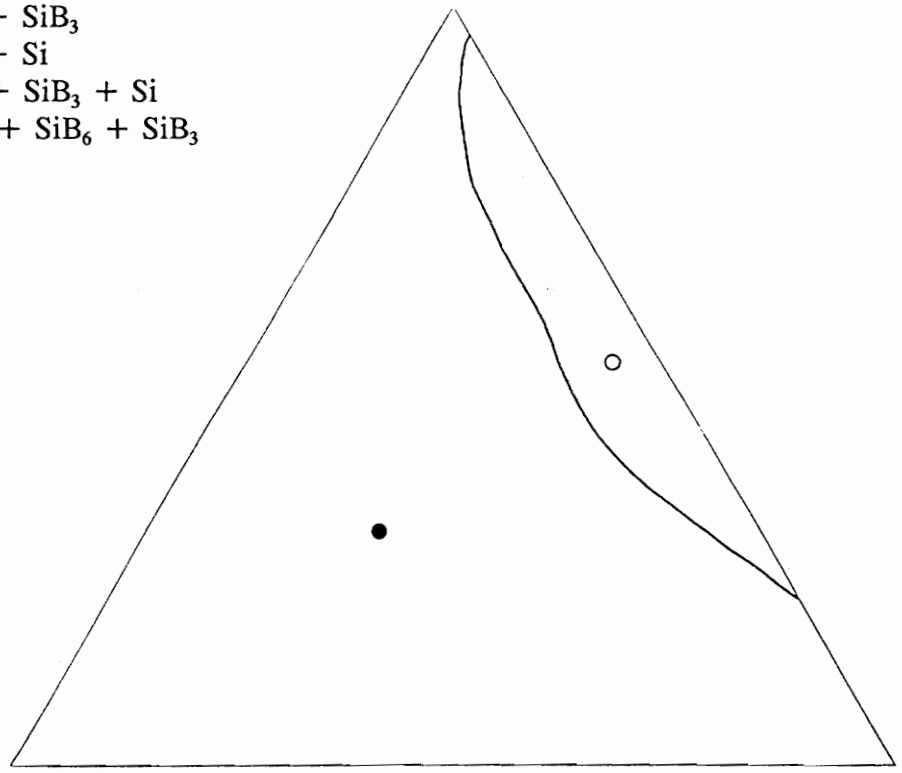

P=1 atm.
T=1500K
H/(Zr + Si + B + Cl)= 10

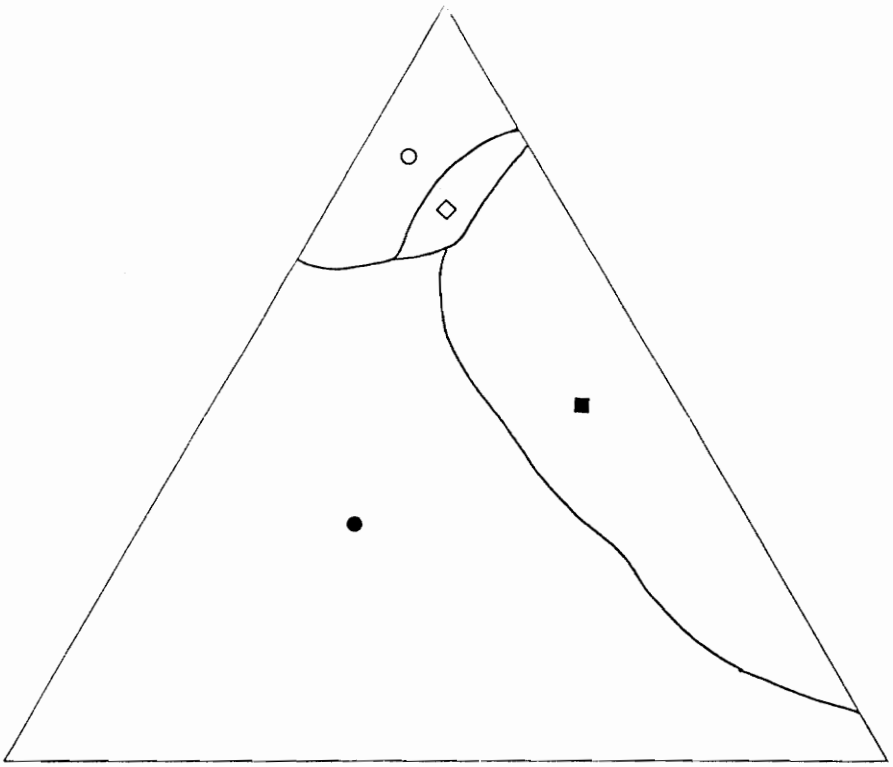

P=1 atm.
T=1100K
H/(Zr + Si + B + Cl)= 25

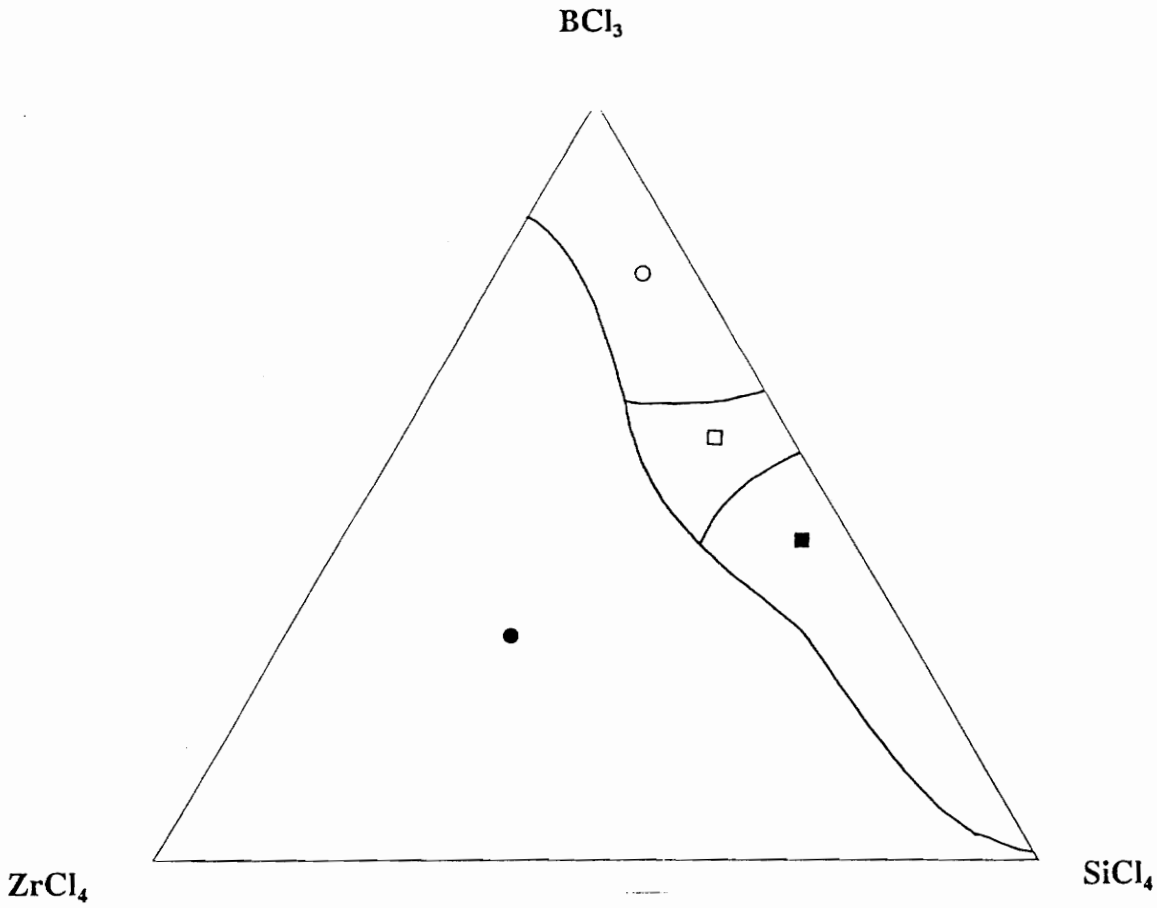

P=1 atm.
T=1300K
H/(Zr + Si + B + Cl)= 25

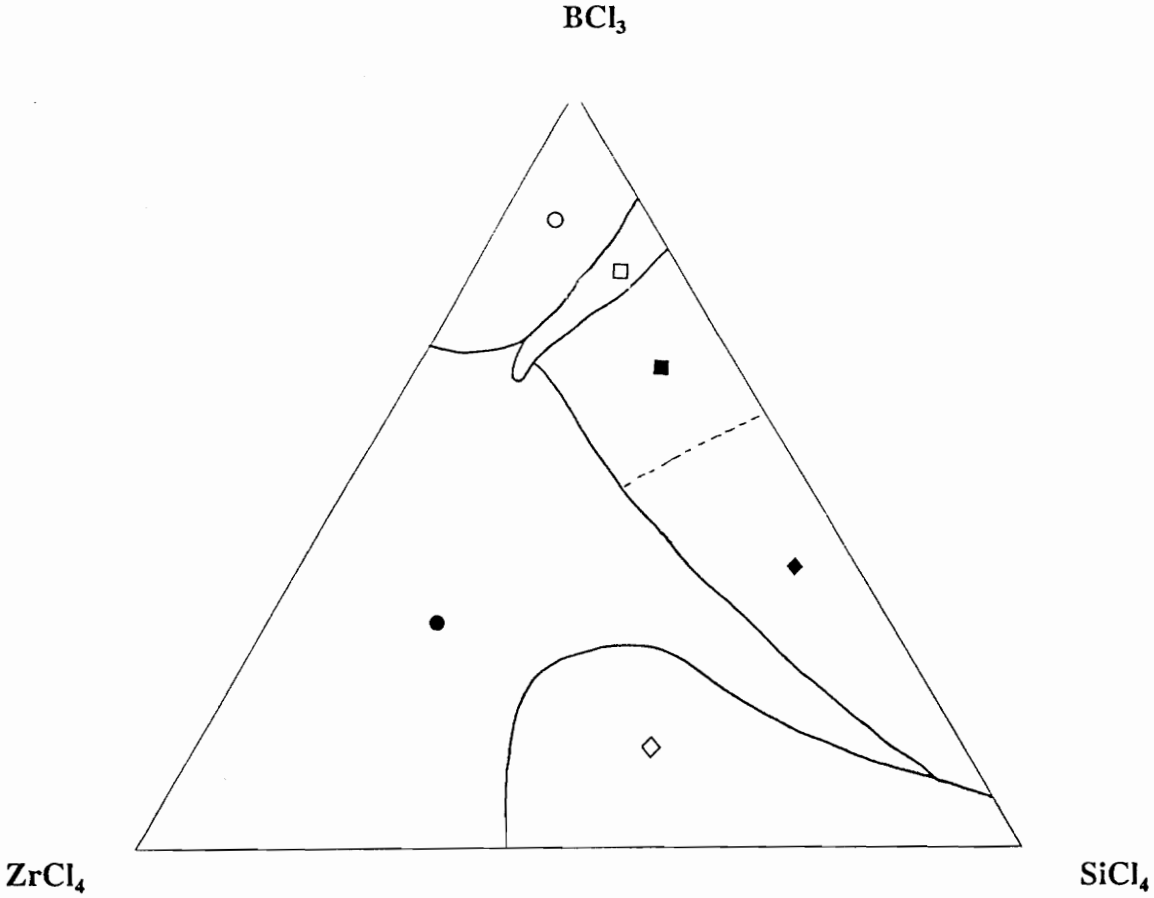

P=1 atm.
T=1500K
H/(Zr + Si + B + Cl)= 25

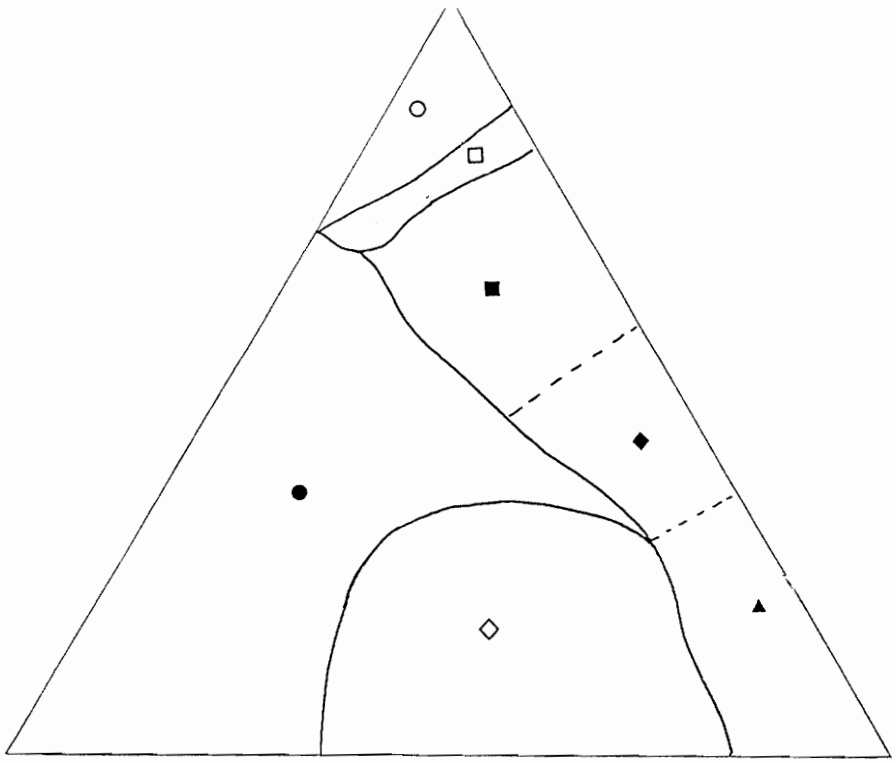

P=1 atm.
T=1100K
H/(Zr + Si + B + Cl)= 50

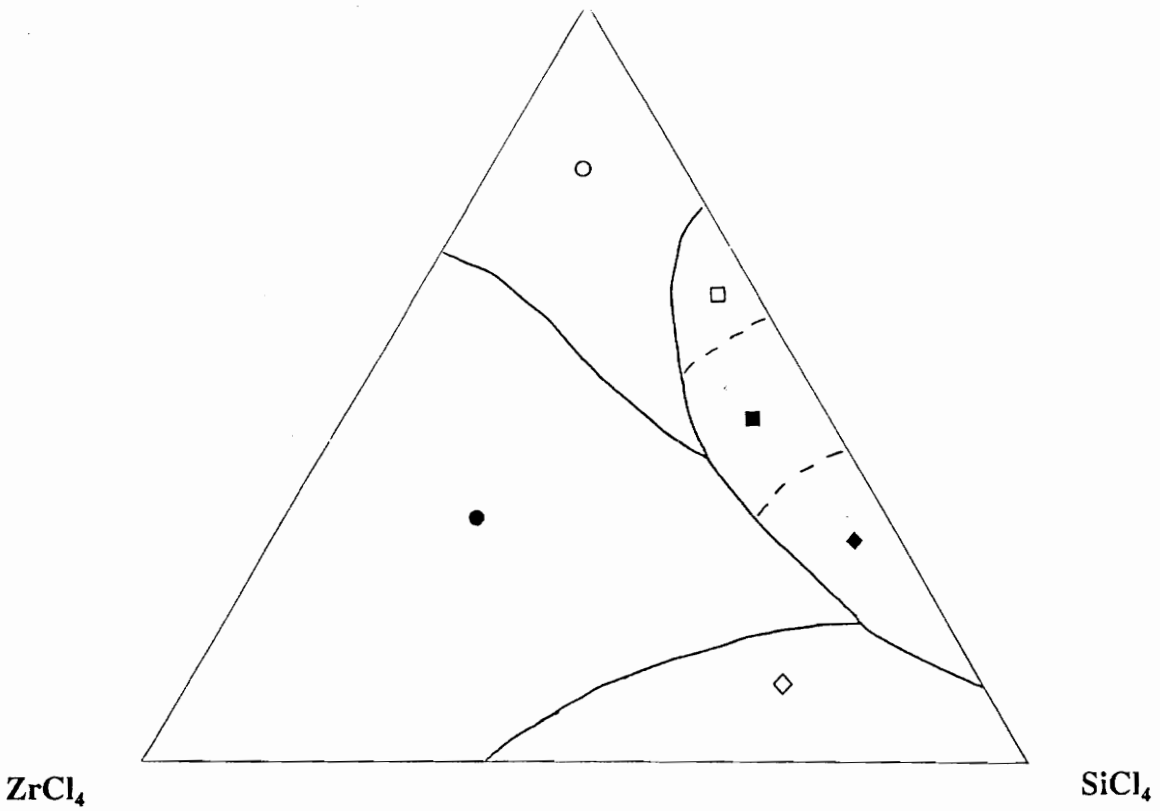

P=1 atm.
T=1300K
H/(Zr + Si + B + Cl)= 50

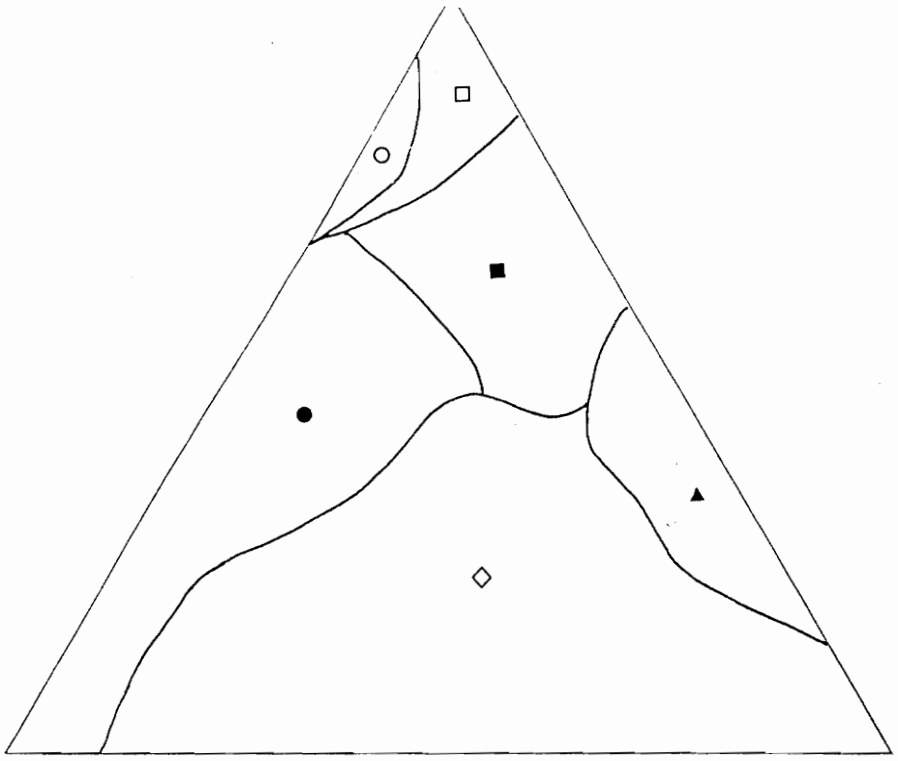

P=1 atm.
T=1500K
H/(Zr + Si + B + Cl)= 50

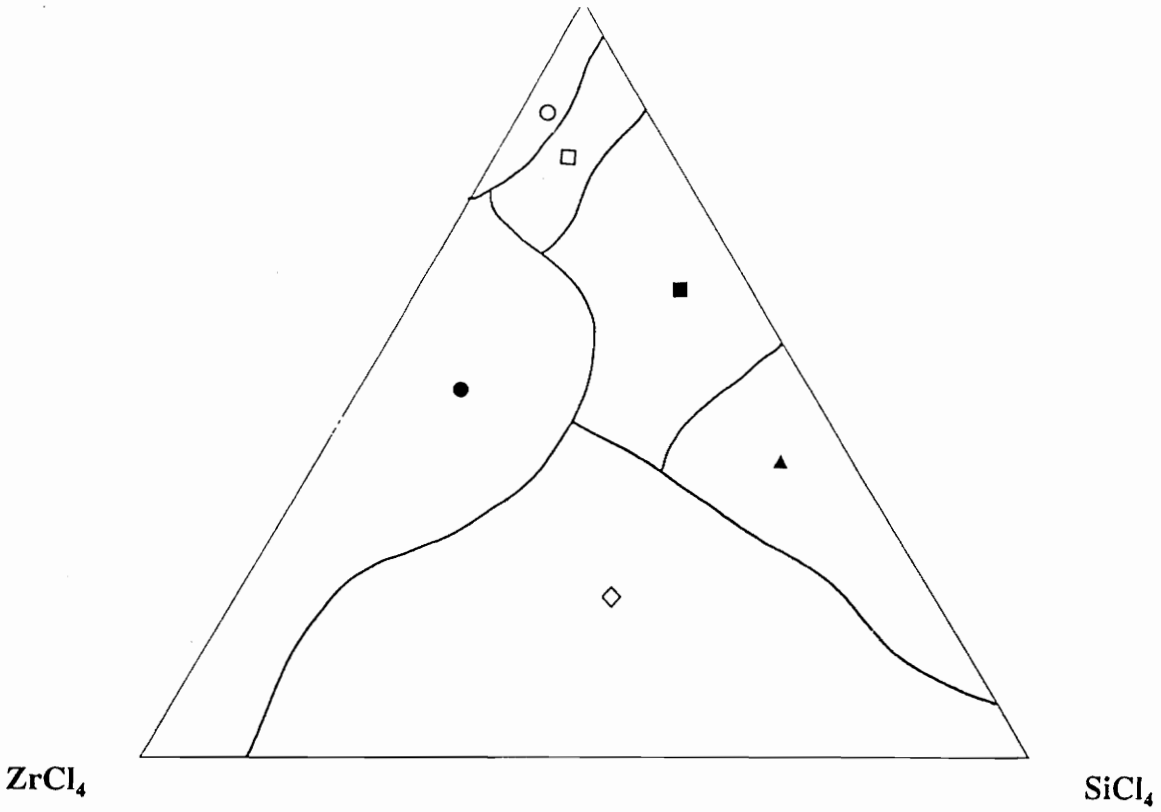

P=0.1 atm.
T=1100K
H/(Zr + Si + B + Cl)= 10

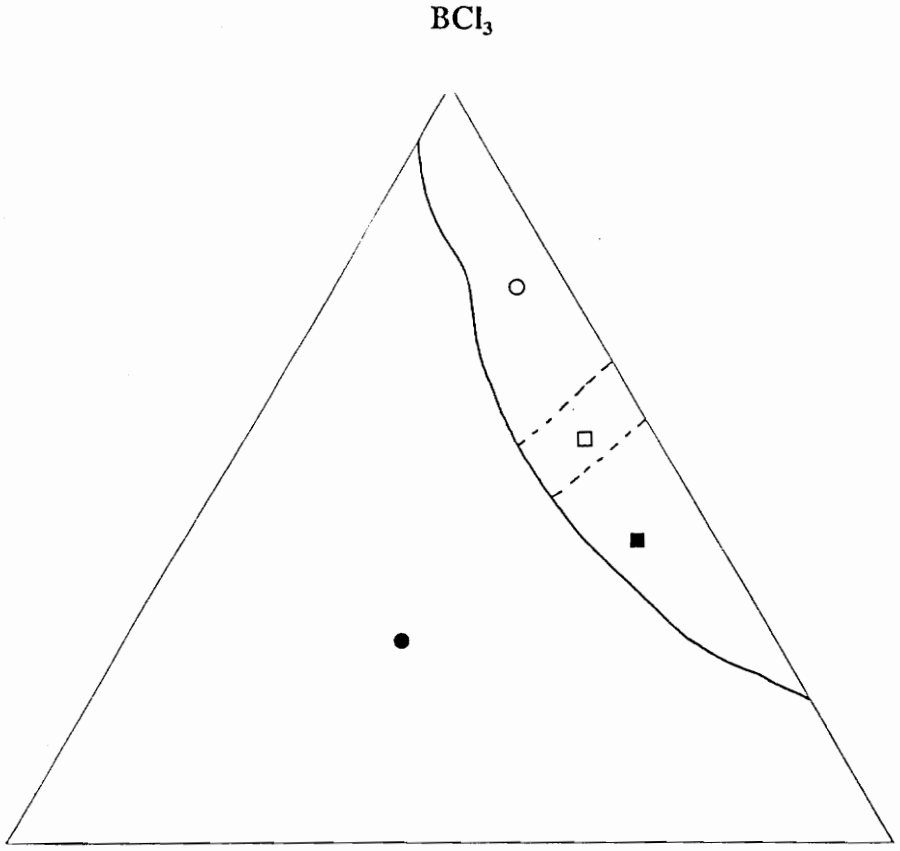

P=0.1 atm.
T=1300K
H/(Zr + Si + B + Cl)= 10

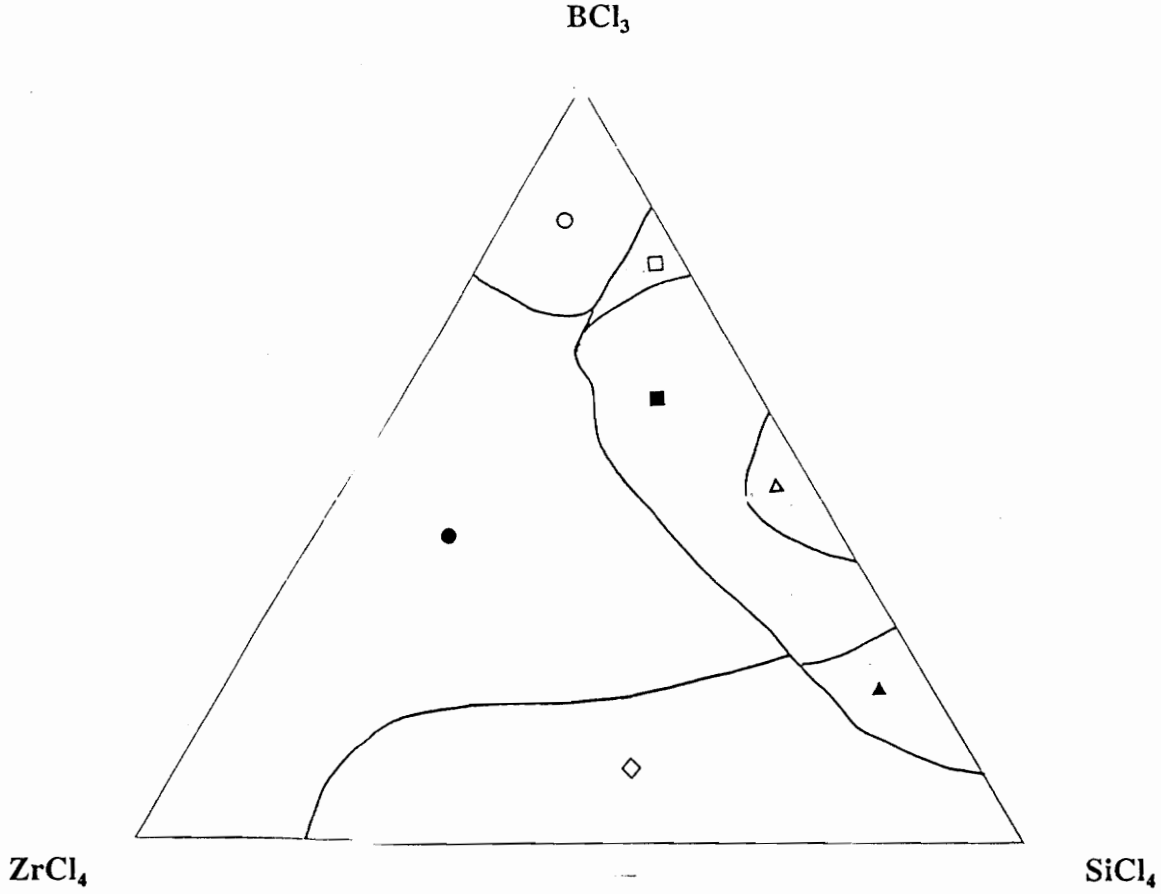

P=0.1 atm.
T=1500K
H/(Zr + Si + B + Cl)= 10

BCl_3

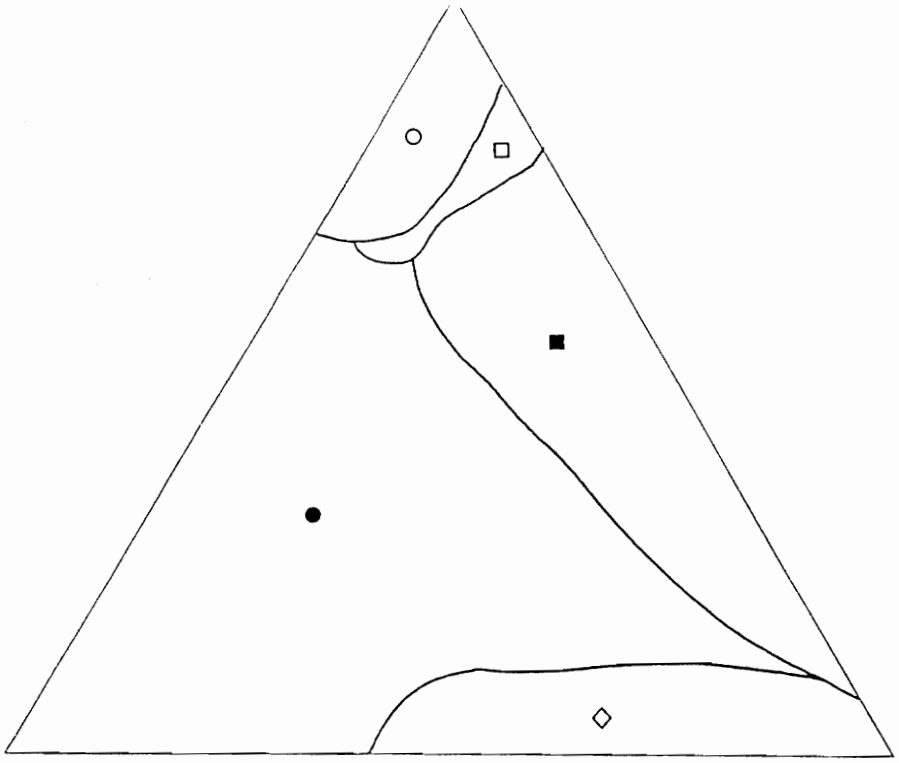

$ZrCl_4$ $SiCl_4$

P=0.1 atm.
T=1100K
H/(Zr + Si + B + Cl)= 25

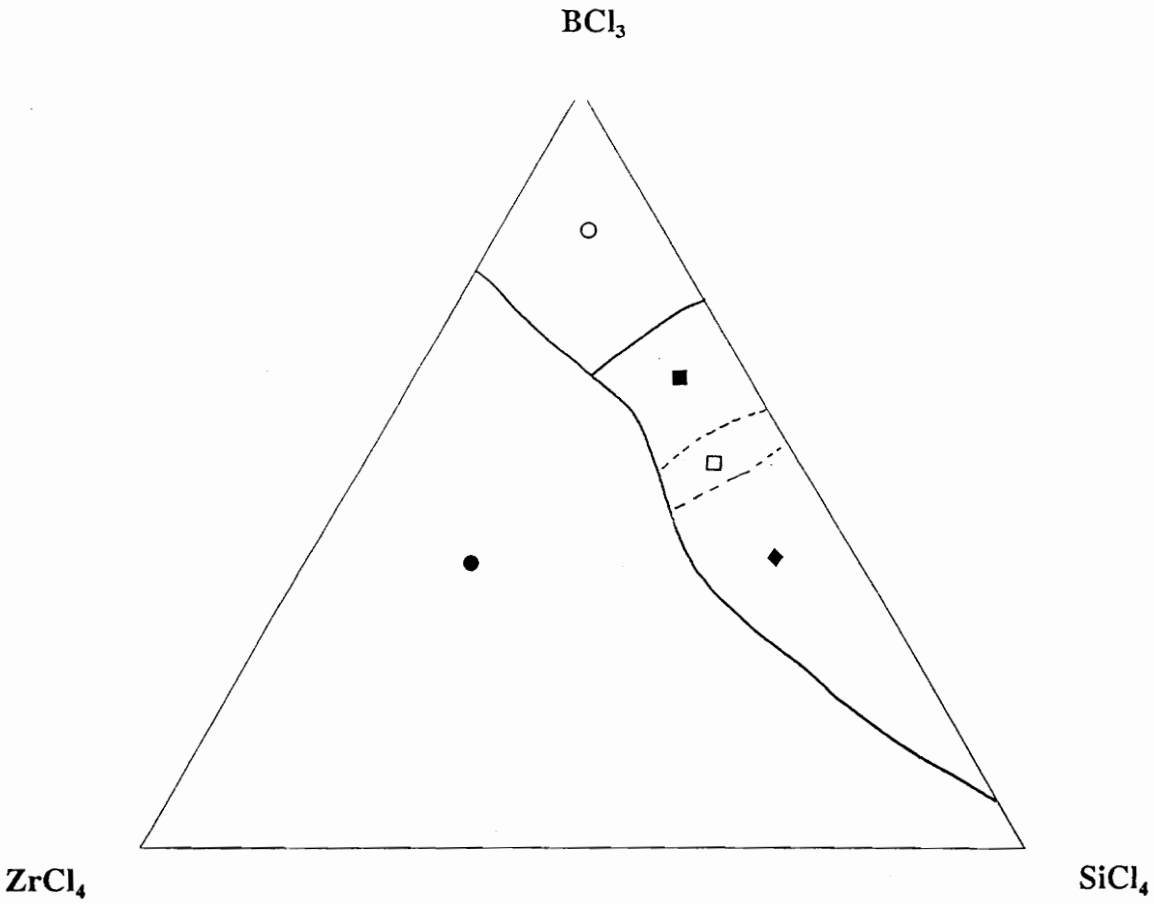

P=0.1 atm.
T=1300K
H/(Zr + Si + B + Cl)= 25

BCl_3

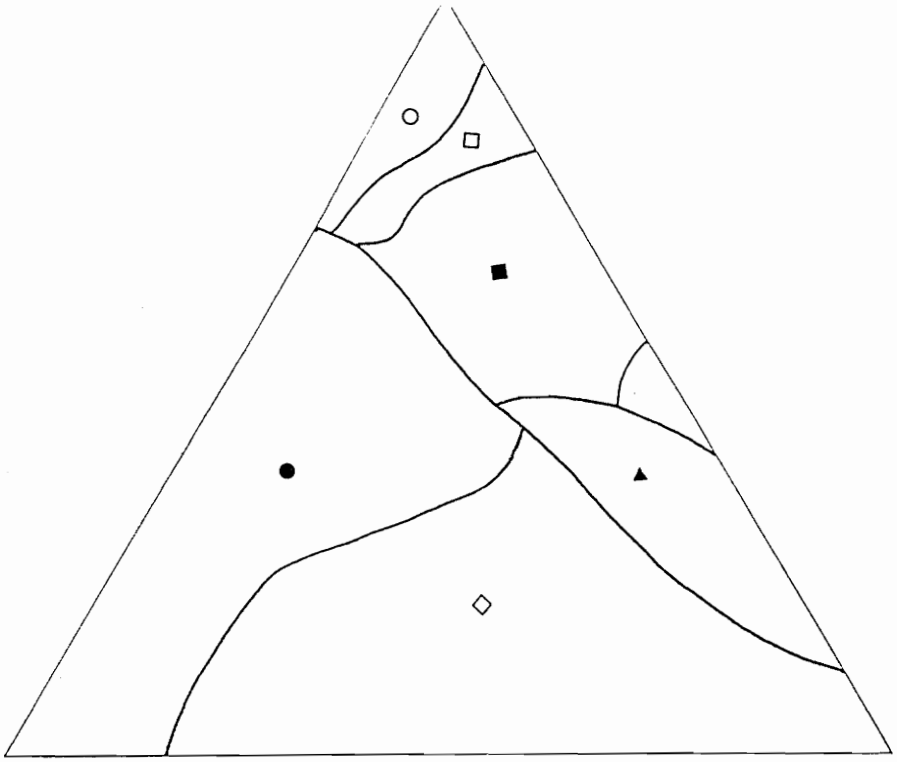

$ZrCl_4$ $SiCl_4$

P=0.1 atm.
T=1500K
H/(Zr + Si + B + Cl)= 25

BCl_3

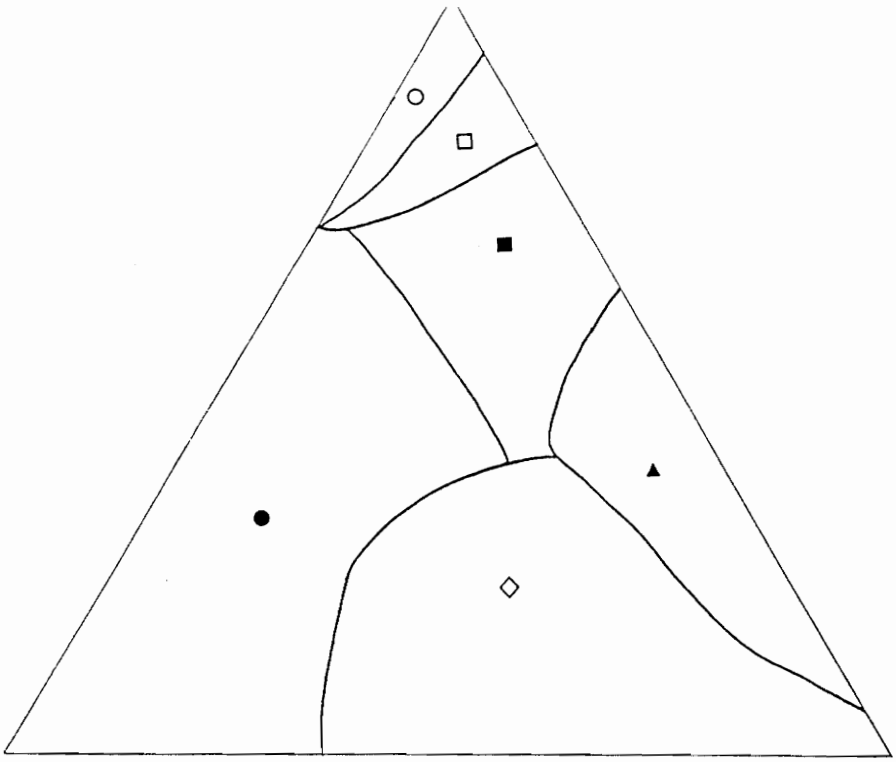

$ZrCl_4$ $SiCl_4$

P=0.1 atm.
T=1100K
H/(Zr + Si + B + Cl)= 50

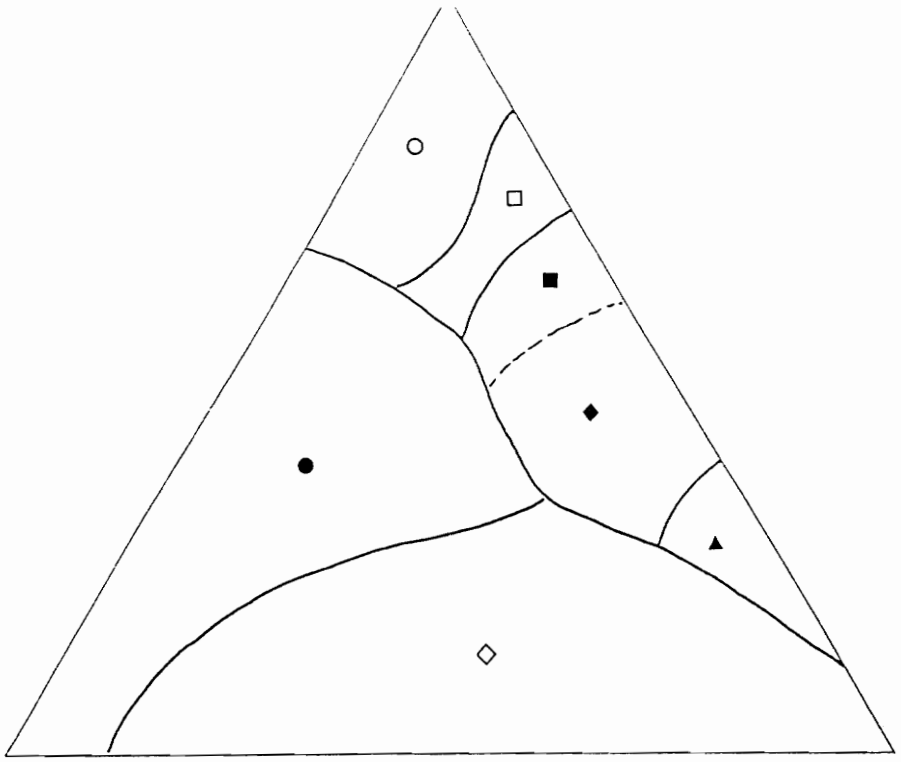

P=0.1 atm.
T=1300K
H/(Zr + Si + B + Cl)= 50

BCl_3

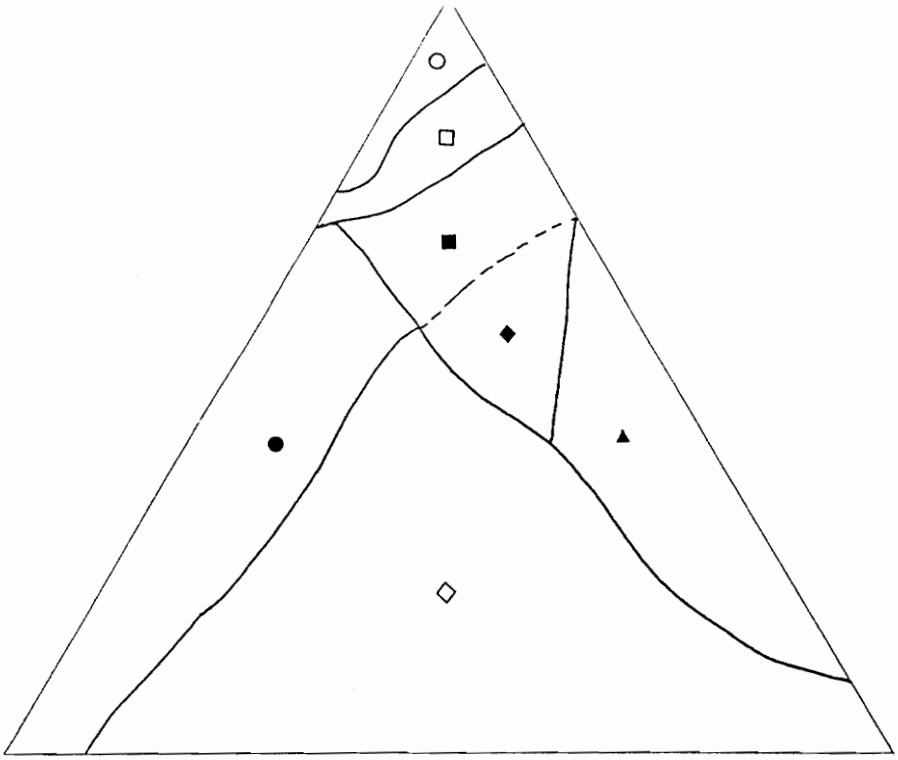

$ZrCl_4$ $SiCl_4$

P=0.1 atm.
T=1500K
H/(Zr + Si + B + Cl)= 50

BCl_3

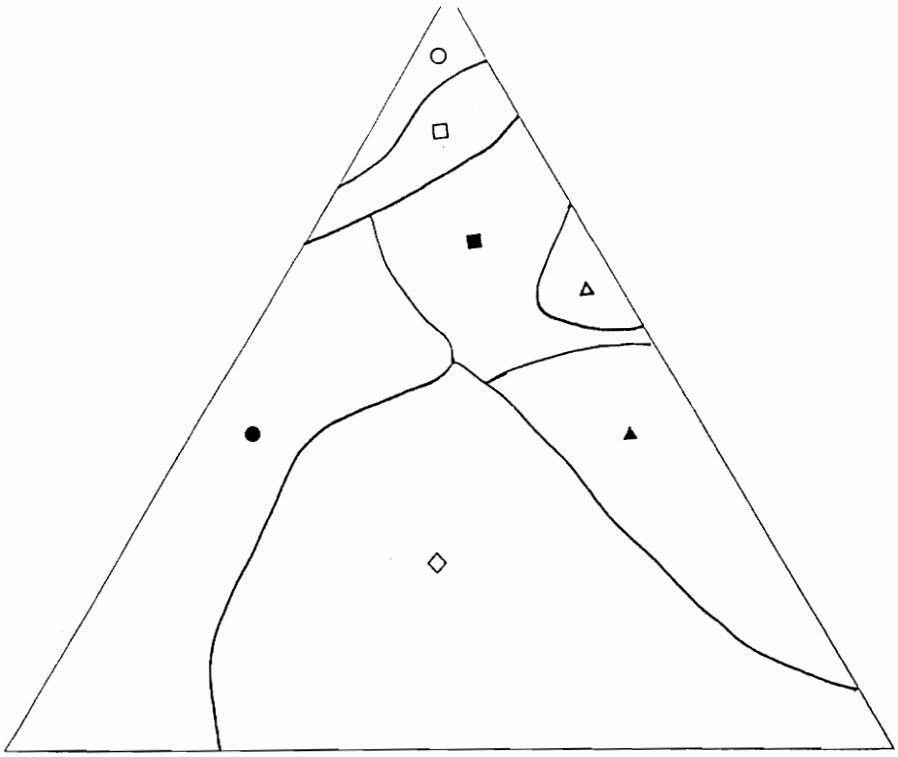

$ZrCl_4$ $SiCl_4$

P=0.02 atm.
T=1100K
H/(Zr + Si + B + Cl)= 10

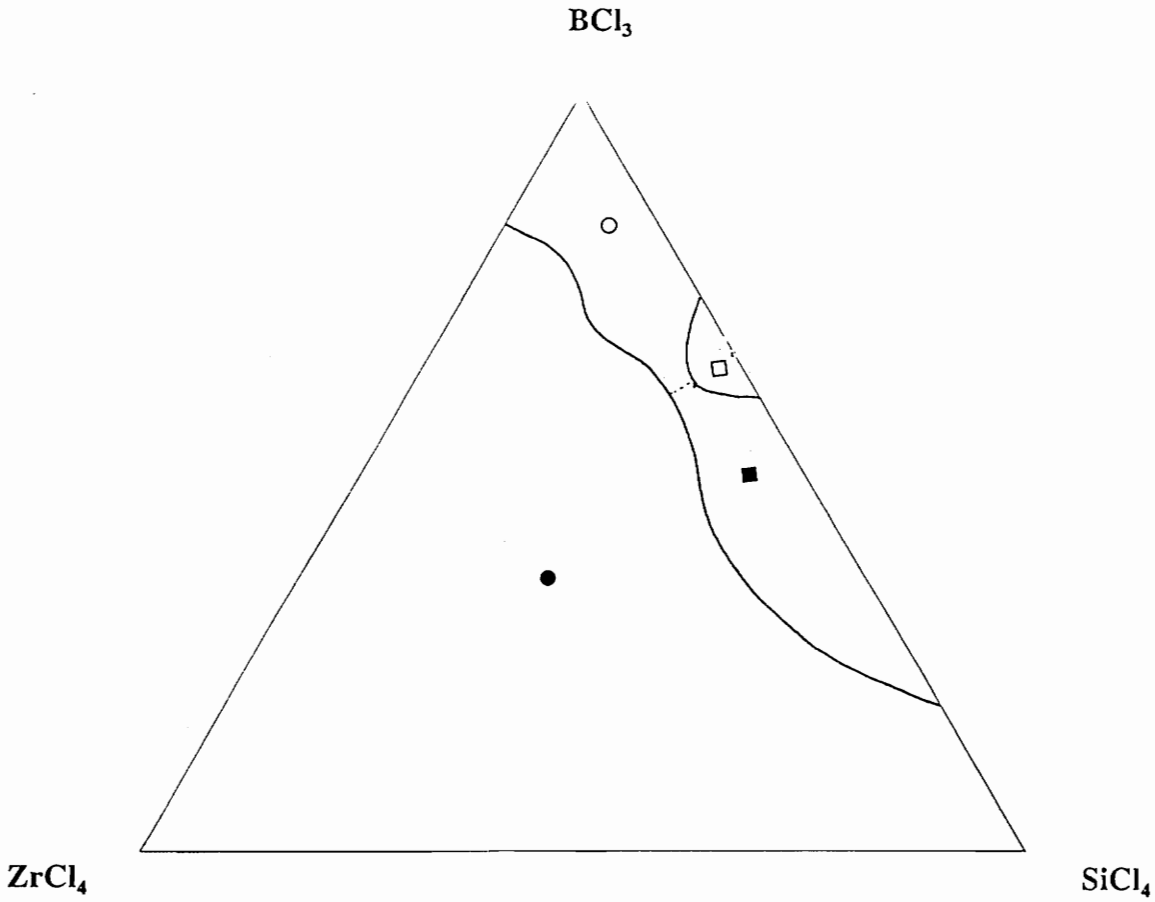

P=0.02 atm.
T=1300K
H/(Zr + Si + B + Cl)= 10

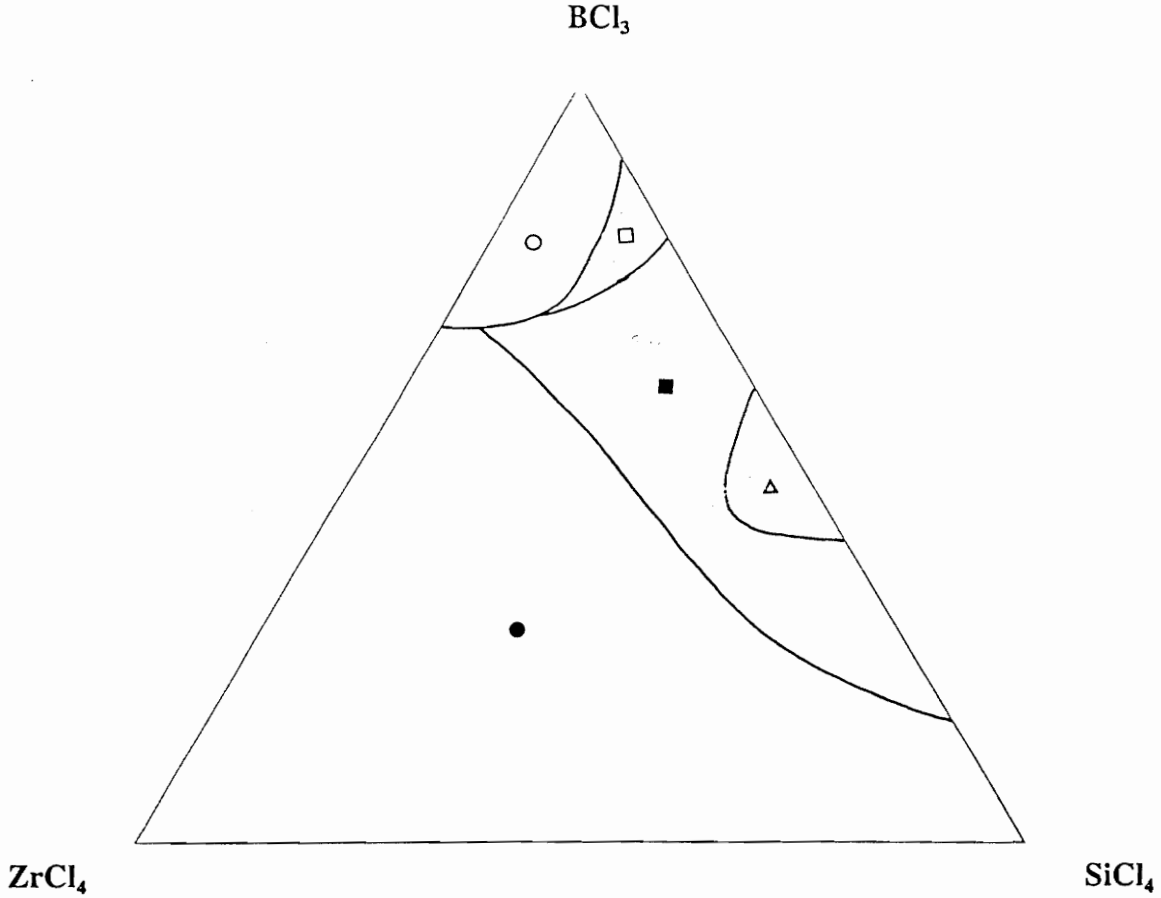

P=0.02 atm.
T=1500K
H/(Zr + Si + B + Cl)= 10

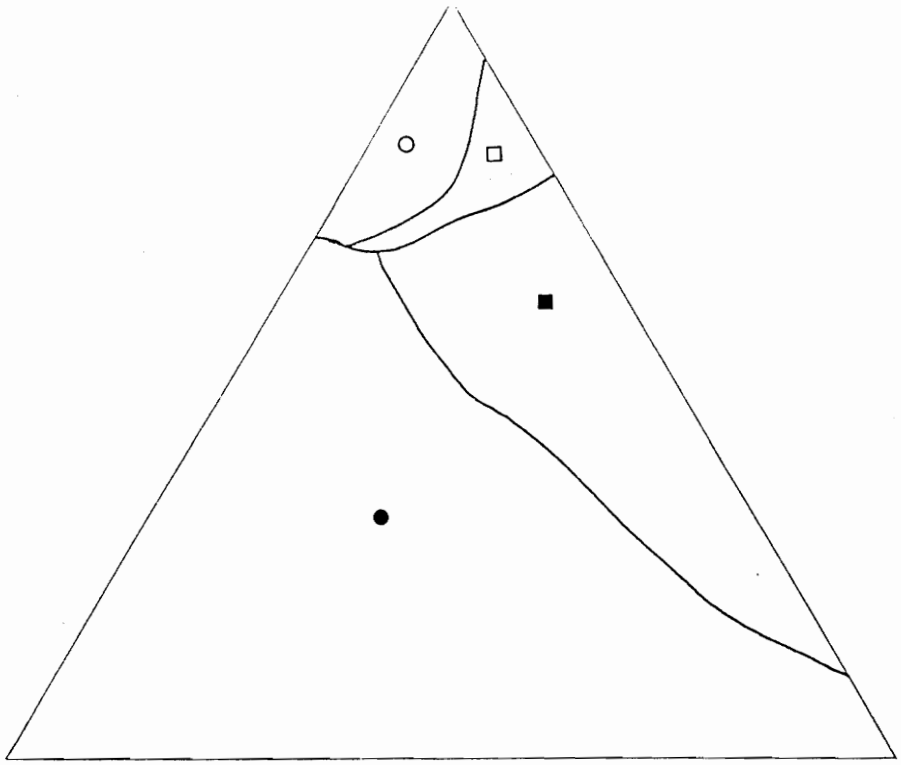

P=0.02 atm.
T=1100K
H/(Zr + Si + B + Cl)= 25

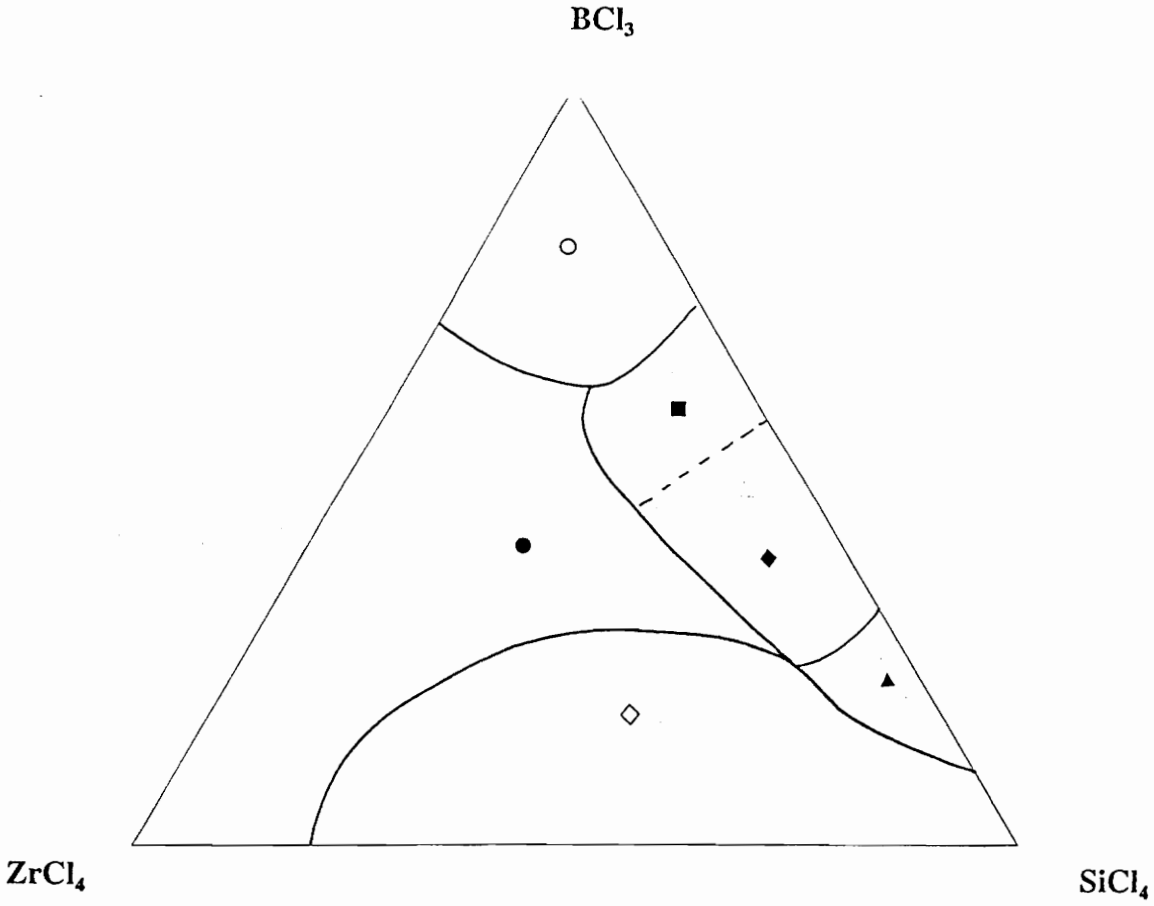

P=0.02 atm.
T=1300K
H/(Zr + Si + B + Cl)= 25

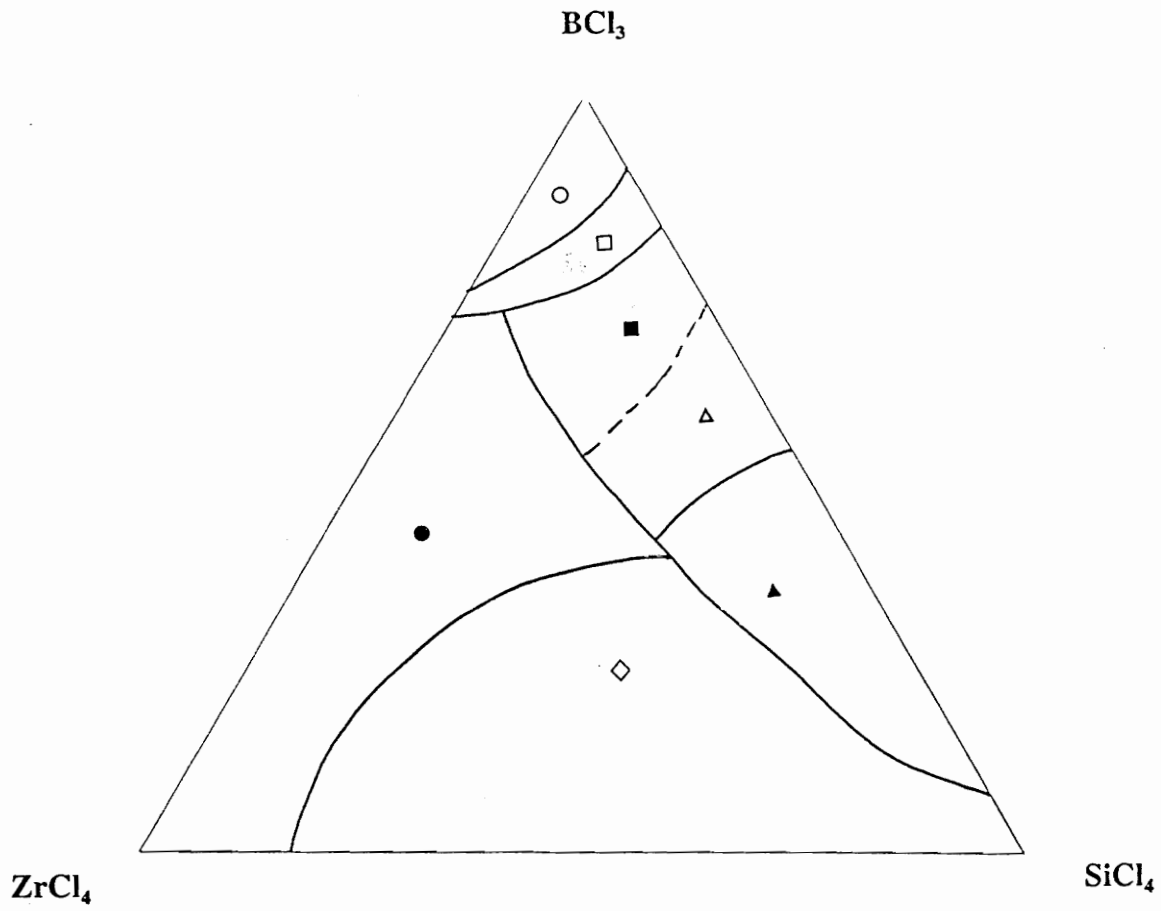

P=0.02 atm.
T=1500K
H/(Zr + Si + B + Cl)= 25

BCl_3

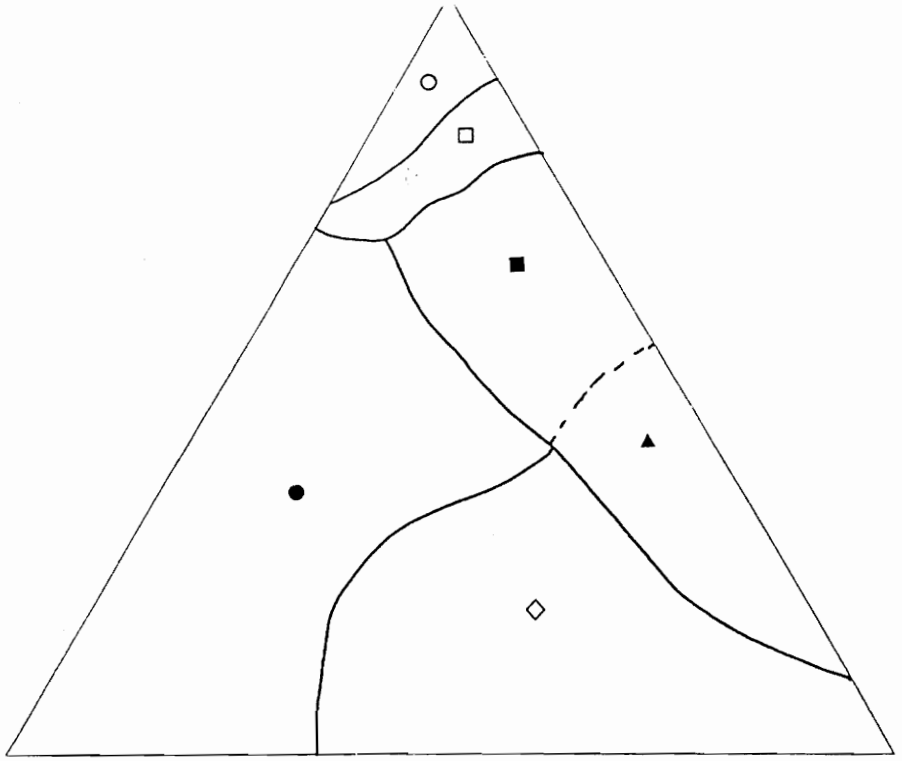

$ZrCl_4$ $SiCl_4$

P=0.02 atm.
T=1100K
H/(Zr + Si + B + Cl)= 50

BCl_3

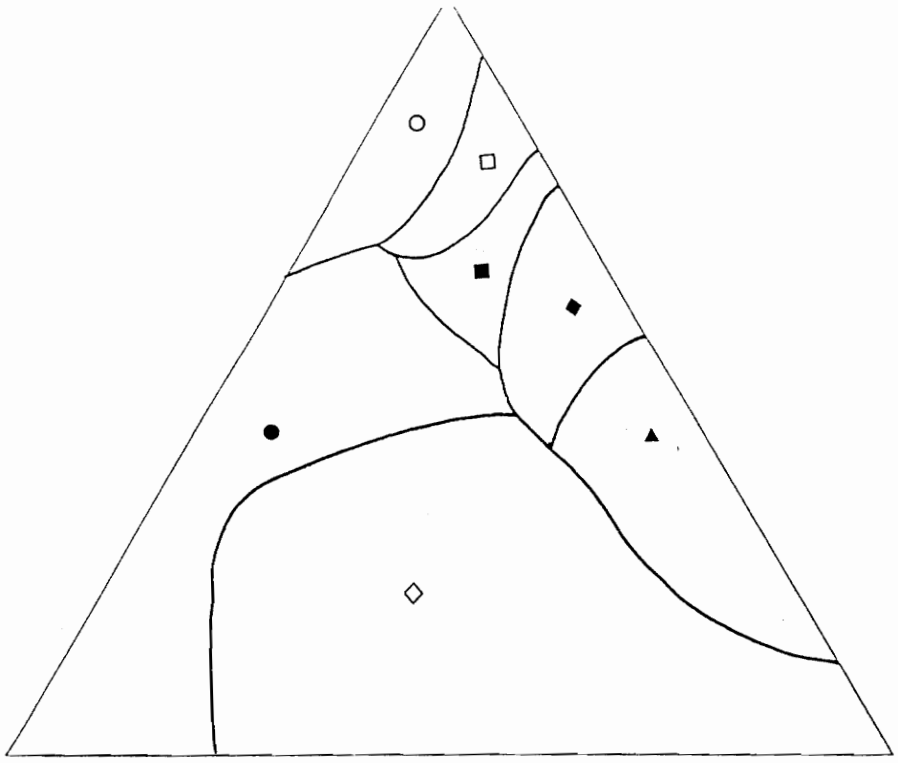

$ZrCl_4$ $SiCl_4$

P=0.02 atm.
T=1300K
H/(Zr + Si + B + Cl)= 50

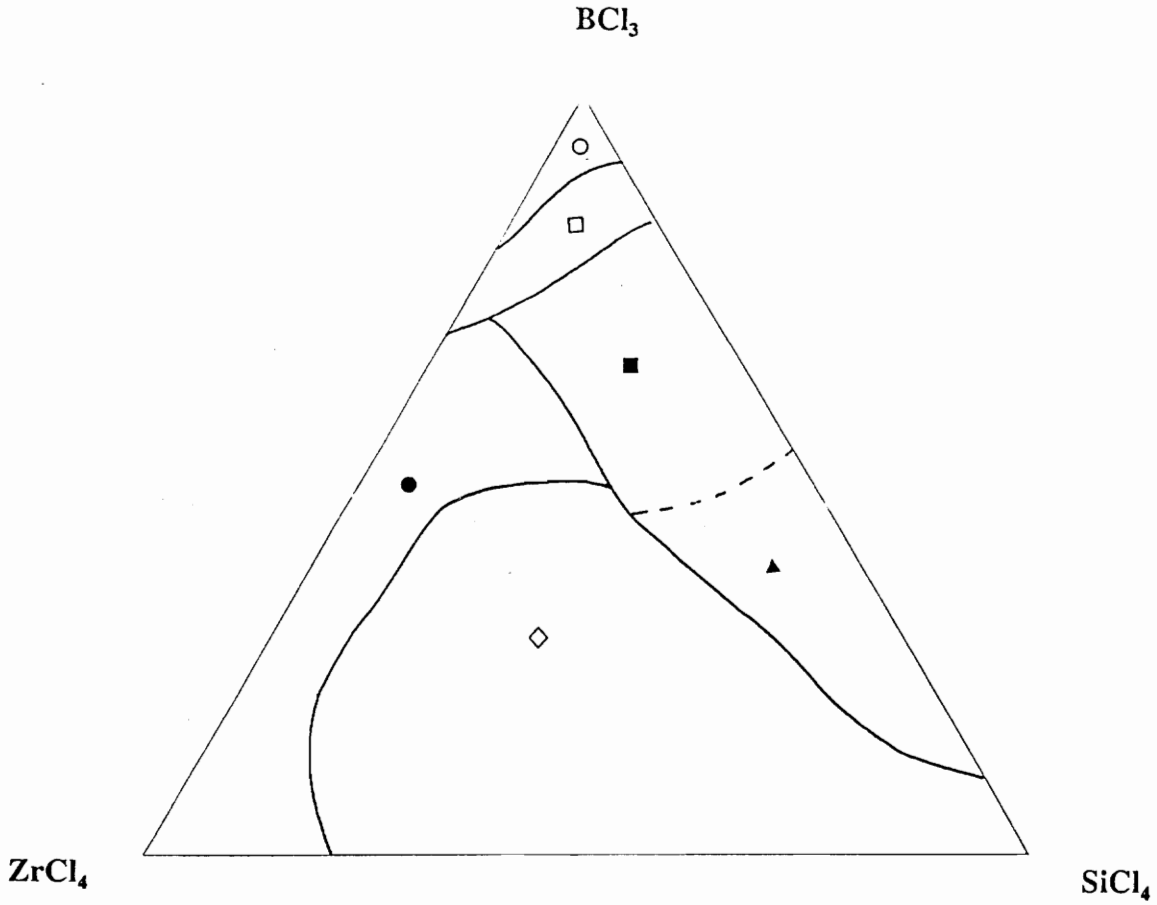

P=0.02 atm.
T=1500K
H/(Zr + Si + B + Cl)= 50

BCl_3

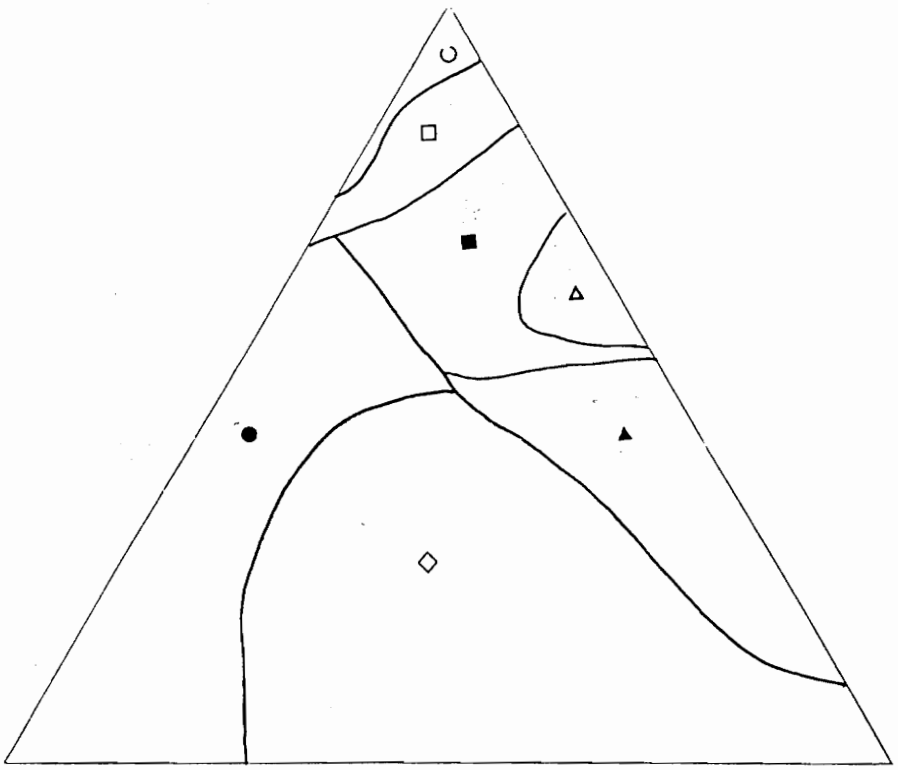

$ZrCl_4$ $SiCl_4$

REFERENCES

1. Kaufman, L. and E.V. Clougherty, "Investigation of Boride Compounds for Very High Temperature Applications," AFML-RTD-TDR-63-4096, 1963.

2. Porter, personal communications, 1994.

3. Berkowitz-Mattuck, J.B., "High-Temperature Oxidation: III. Zirconium and Hafnium Borides," J. Electrochemical Soc., 113 (9), 908-914, 1968.

4. Clougherty, E.V. "Research and Development of Refractory Oxidation-Resistant Diborides," AFML-TR-68-190, 1968.

5. Tripp, W.C., Davis, H.H. and H.C. Graham, "Effect of SiC Addition on the Oxidation of ZrB_2," Ceramic Bulletin, 52 (8), 612-616, 1973.

6. Rasky, D.J., Bull, J.D. and H.K. Tran, "Ablation Response of Advanced Refractory Composites," The 15th Conference on Metal Matrix, Carbon, and Ceramic Matrix Composites, 153-180, 1991.

7. Talmy, I.G., Wuchina, E.J., and J.A. Zaykoski, "Ceramics in the NbB_2-CrB_2 System," Proceedings of the Materials Research Society: Ceramic Matrix Composites, Boston, MA, in print.

8. Fenter, J.R., "Refractory Diborides as Engineering Materials," SAMPE Quarterly, 2 (3), 1-15, 1971.

9. Wiley, D.F., Manning, W.R. and O. Hunter, "Elastic Properties of Polycrystalline TiB_2, ZrB_2, and HfB_2 from Room Temperature to 1300K," J. Less-Common Metals, 18, 149-157, 169.

10. Moisan, H. and A. Stock, "Preparation et Proprietes de deux Borures de Silicium: SiB_3 et SiB_6," C. R. Ac. Sc. Paris, 131, 139-143, 1900.

11. Brewer, L., Sawyer, D.L., Templeton, D.H. and C.H. Dauben, "A Study of the Refractory Borides," J. Am Ceram. Soc., 34, 173-179, 1951.

12. Stavrolakis, J.A., Barr, H.N. and H.H. Rice, "An Investigation of Boride Cermets," Ceramic Bulletin, 35, 47-52, 1956.

13. Colton, E., "Preparation of Tetraboron Silicide,B_4Si," J. Am. Ceram. Soc., 82, 1002, 1960.

14. Tremblay, R. and R. Angers, "Preparation of High Purity SiB_4 by Solid State

Reaction Between Si and B," Ceramics International, 15, 73-78, 18989.

15. Samsonov, G.V. and V.M. Sleptosov, "Investigation of the Solubility of Boron in Silicon," Russ. J. Inord. Chem., 8, 1047-1048, 1963.

16. Brosset, C. and B. Magnusson, "The Silicon-Boron System," Nature, 187, 54-55, 1960.

17. Matkovich, V.I., "A New Form of Boron Silicide, B_4Si," Acta Cryst., 13, 679-680, 1960.

18. Feigelson, R.F. and W.D. Kingery, "Physical Properties of Polycrystalline Silicon Borides," Ceramic Bulletin, 42 (11), 688-693, 1963.

19. Rizzo, H.F., Weber, B.C. and M.A. Schwartz, "Refractory Compositions Based on Silicon-Boron-Oxygen Reactions," J. Am. Ceram. Soc, 43 (10), 497-504, 1960.

20. Talmy, I.G., Zaykoski, J.A. and E.J. Wuchina, "Ceramics in the CrB_2-Al_2O_3 System," Presented at 19th Annual Conference on Ceramic Matrix Composites, Cocoa Beach, Fl, Jan. 1995.

21. Cline, C.F. and D.E. Sands, "A New Silicon Boride,SiB_4," Nature, 185, 456, 1960.

22. JCPDS Powder Diffraction File, Joint Committee on Powder Diffraction Standards, International Center for Diffraction Data, Swarthmore, PA, 1993.

23. Olesinski, R.W. and G.J. Abbaschian, "The B-Si System," The Bulletin of Alloy Phase Diagrams, 5 (5), 478-484, 1984.

24. Rudy, E. and S. Windisch, "The Hf-B System, Part I. Vol IX.," AFML-TR-65-2, 1966.

25. Rogl, and Potter, "A Critical Review and Thermodynamic calculation of the Binary System Hafnium-Boron," CALPHAD, 12 (3), 207-218, 1988.

26. Gokhale, A.B. and G.J. Abbaschian, "The Hf-Si System," Bull. Alloy Phase Diagrams, 10 (4), 390-393, 1989.

27. Brukl, C.E., "Ternary Phase Equilibria in Transition Metal-B-C-Si Systems, Part I. Vol. 13," AFML-TR-65-2, 72, 1968.

28. Rudy, E., "Ternary Phase Equilibria in Transition-Metal Boron-Carbon-Silicon

Systems. Part V. Compendium of Phase Diagram Data," AFML-TR-65-2, May 1969.

29. Van Arkel, A.E. and J.H. deBoer, "Preparation of Pure Titanium, Zirconium, Hafnium, and Thorium Metals," Z. Anorg.Allegem.Chem., 148, 345, 1925.

30. Pierson, H.O., Handbook of Chemical Vapor Deposition Principles, Technology and Applications, Noyes Publications, New Jersey, 1992.

31. Ohring, M., The Materials Science of Thin Films, Academic Press, Boston, 1992.

32. Bryant, W.A., "Review: The Fundamentals of Chemical Vapor Deposition," J. Mat. Sci., 12, 1285-1306, 1977.

33. Yee, K.K., "Protective Coatings for Metals by Chemical Vapor Deposition," International Metals Review, 23 (1), 19-39, 1978.

34. Stinton, D.P., Besmann, T.M. and R.A. Lowden, "Advanced Ceramics by Chemical Vapor Deposition Techniques," Ceramic Bulletin, 67 (2), 350-354, 1988.

35. Lowden, R.A., "Characterization and Control of the Fiber-Matrix Interface in Ceramic Matrix Composites," ORNL/TM-11039, 1989.

36. Besmann, T.M., Sheldon, B.W., Lowden, R.A. and D.P. Stinton, "Vapor-Phase Fabrication and Properties of Continuous-Filament Ceramic Composites," Science, 253, 1104-1109, 1991.

37. Campbell, I.E., Powell, C.F., Nowicki, D.H. and B.W. Gonser, "The Vapor Deposition of Refractory Materials," J. Electrochem. Soc, 96 (5) 318-333, 1949.

38. Landingham, R.L. and W. Casey, "Ultrafine Dispersion Strengthening of Tungsten by Chemical Vapor Deposition," J. Less-Common Metals, 26, 173-198, 1972.

39. Huegel, F.A. and W.R. Holman, "CVD Tungsten and Tungsten-Rhenium Alloys for Structural Applications, III. Recent Developments," Proceedings of the Second International Conference on CVD, 171-192, 1970.

40. Nicholl, A.R., Hildebrandt, U.W. and G. Wahl, "The Properties of a Chemical Vapor-Deposited Silicon Base Coating for Gas Turbine Blading," Thin Solid Films, 64, 321-326, 1979.

41. Blocher, J.M., "Nuclear Fuel Particles Coated with Mixture of Pyrolytic Carbon and Silicon Carbide," U.S. Patent 3,249,509, 1966.

42. Kaae, J.L. and T.D. Gulden, "Structure and Mechanical Properties of Codeposited Pyrolytic C-SiC Alloys," J. Am. Ceram. Soc., 54 (12), 605-609, 1971.

43. Atkins, R.J. and J.C. Bokros, "The Deposition of Pure and Alloyed Isotropic Carbons in Steady-State Fluidized Beds," Carbon, 12, 439-52, 1974.

44. Hirai, H., "CVD of Si_3N_4 and its Composites," Emergent Process Methods for High Technology Ceramics, The Davis, Palmour and Porter, eds., 19th University Conference on Ceramic Science, NC State, Nov. 8-10, 1982.

45. Hirai, T., Hayashi and A. Tanaka, "Effect of $TiCl_4$ Addition on the Structure of Chemically Vapor-Deposited Si_3N_4," Proceedings of the Fourth European Conference on CVD, 503-508, 1983.

46. Hirai, T. and S. Hayashi, "Preparation and some Properties of Chemically Vapor-Deposited Si_3N_4-TiN Composite," J. Mat. Sci., 17, 1320-1328, 1982.

47. Hirai, T. and S. Hayashi, "Density and Deposition Rate of Chemically Vapor Deposited Si_3N_4-TiN Composites," J. Mat. Sci., 18, 2401-2406, 1983.

48. Hayashi, S., Hirai, S., Hiraga, K. and M. Hirabayashi, "Microstructure of Si_3N_4 Composites Prepared by Chemical Vapor Deposition," J. Mat. Sci., 17, 3336-3340, 1982.

49. Nickl, J.J. and C. Von Braunmuhl, "Chemical Vapor Deposition in the Systems Silicon-Carbon and Silicon-Carbon-Nitrogen," J. Less Common Metals," 37, 317-329, 1974.

50. Zirinski, S. and E.A. Irene, "Selective Studies of Chemical Vapor Deposited AlN-Si_3N_4 Mixture Films," J. Electrochem. Soc., 125 (2), 305-14, 1978.

51. Nickl, J.J., Schweitzer K.K. and P. Luxenburg, "Chemical Vapor Deposition of the Systems Ti-Si-C and Ti-Ge-C," Proceedings of the Second International Conference on CVD, 297, 1970.

52. Stinton, D.P. and W.J. Lackey, "Simultaneous Chemical Vapor Deposition of SiC-Dispersed Phase Composites," Ceramic Engineering and Science Proceedings, 6 (7-8), 707-713, 1985.

53. Lackey, W.J., Freeman, G.B., Hanigofsky, J.A., Thompson, J.R. and G.J.

Gerard, "Ultrafine Microstructure Composites Prepared by Chemical Vapor Deposition," ONR Report A-4699-2, Dec. 1988.

54. Besmann, T.M., "Chemical Vapor Deposition in the Boron-Carbon-Nitrogen," J. Am Ceram. Soc., 73 (8), 2498-2501, 1990.

55. Besmann, T.M., "Thermodynamic Analysis of the Chemical Vapor Deposition of Composite Si_3N_4-BN Coatings," J. Am. Ceram. Soc., 69 (1), 69-74, 1986.

56. Besmann, T.M. and E.J. Wuchina, unpublished research, 1987.

57. Lowden, R.A., More, K.L., Besmann, T.M. and R.D. James, "Microstructural Characterization of Multiphase Coatings Produced by Chemical Vapor Deposition," Proceedings of the Materials Research Society: Chemical Vapor Deposition of Refractory Metals and Ceramics, 168, 159-166, 1989.

58. Golda, E.M. and B. Gallois, "Chemical Vapor Deposition of Multiphase Boron-Carbon-Silicon Ceramics," Proceedings of the Materials Research Society; Chemical Vapor Deposition of Refractory Metals and Ceramics, 250, 167-172, 1991.

59. Lackey, W.J., Smith, A.W., Dillard, D.M. and D.J. Twait, "Codeposition of Dispersed Phase Ceramic Composites," Proceedings of the Tenth International Conference on Chemical Vapor Deposition, 1987.

60. Lackey, W.J., Smith, A.W. and D.J. Twait, "Chemical Vapor Deposition of Oxidation-Resistant HfB_2 + SiC Composites, Ceram. Eng. Sci. Proc., 9 (9-10), 1223-1232, 1988.

61. Moers, K., "Methods for Preparation of Pure High-Melting Carbides, Nitrides, and Borides and Description of a Few of Their Properties," Z. Anorg. Allgem. Chem., 198, 243-261, 1931.

62. McCandless, L.C., Withers, J.C., and C.R. Brummett, "High Strength, High Modulus, Low Density Boron Silicide Monofilaments, and Method of making Same," U.S. Patent 3,607,367, 1971.

63. Armas, B., Combescure, C., Male, G. and M.Morales, "A Study of the Thermal Decomposition of Gaseous Si-B Bromides under Reduced Pressure," J. Less-Common Metals, 67, 449-453, 1979.

64. Armas, B. and C. Combescure, "Chemical Vapor Deposition at Low Pressure in the System Silicon-Boron," Proceedings of the Sixth International Conference on Chemical Vapor Deposition, 77-5, 181-182, 1977.

65. Goto, T., Mukaida, M. and T. Hirai, "Chemical Vapor Deposition of Silicon Borides," Proceedings of the Materials Research Society: Chemical Vapor Deposition of Refractory Metals and Ceramics, 168, 167-172.

66. Dirkx, R.R. and K.E. Spear, "A Morphological Study of Silicon Borides Prepared by CVD," Emergent Process Methods for High-Technology Ceramics, Davis, Palmour, and Porter, eds., 17, 359-369, 1982.

67. Motozima, S., Sugiyama, K. and Y. Takahashi, "Chemical Vapor Deposition of Tetraboride Silicide Whiskers," Bull Chem. Soc. Japan, 48 (5), 1463-1466, 1975.

68. Spear, K.E. and R.R. Dirkx, "Predicting the Chemistry in CVD Systems," Proceedings of the Materials Research Society, Vol. 168, 1989.

69. Gebhardt, J.J. and R.F. Cree, "Vapor-Deposited Borides of Group IVA Metals," J. Am Ceram. Soc., 48 (5), 1965.

70. Shinavski, R.A. and R.J. Diefendorf, "Chemical Vapor Infiltration of Hafnium Diboride Matrix Composites," Ceram. Eng. Sci. Proc., 1992.

71. Sheehan, J. A., personal communications, Aug. 1994.

72. Lowden, R.A., personal communications, 1993.

73. Stull, D.R. and H. Prophet, eds, JANAF Thermochemical Tables, Second Ed., U.S. Gov. Printing Office, Washington, DC, 1971.

74. Barin, I., Thermochemical Data of Pure Substances, VCH Publishers.

75. Spear, K.E. and R.R. Dirkx, "Optimization of Thermodynamic Data for Silicon Borides," CALPHAD, 11 (2), 167-175, 1987.

76. Greenwood, N.N. and A. Earnshaw, Chemistry of the Elements, Pergamon Press, Oxford, 1984.

77. Sichen, D., "Standard Gibbs Energies of Formation of the Carbides of Vanadium by Emf Measurements," Met. Trans. B, 21, 313-320, 1990.

78. Bloem, J., "Gas Phase Diffusion and Surface reactions in the Chemical Vapor Deposition of Silicon," Pure & Applied Chemistry, 50, 435-447, 1978.

79. Brinkley, S.R., "Calculation of the Equilibrium Composition of Systems of Many Constituents," J. Chem. Phys., 15 (2), 107-110, 1947.

80. White, W.B., Johnson, S.M. and G.B. Danzig, "Chemical Equilibrium in Complex Mixtures," J. Chem. Phys., 28 (5), 751-755, 1958.

81. Eriksson, G., "Thermodynamic Studies of High Temperature Equilibria XII. SOLGASMIX," Chem. Scripta, 8, 100-103, 1975.

82. Eriksson, G., "Thermodynamic Studies of High Temperature Equilibria III. SOLGAS," Acta Chem. Scan., 25, 2651-2658, 1971.

83. Besmann, T.M., "SOLGASMIX-PV, a Computer Program to Calculate Equilibrium Relationships in Complex Chemical Systems," ORNL/TM 5775, Oak Ridge National Lab, 1977.

84. Spear, K.E., "Principles and Applications of CVD," Pure & Applied Chemistry, 54 (7), 1297-1311, 1982.

85. Shinavski, R.J., personal communication, Jan. 1995.

86. Spear, K.E. and R.R. Dirkx, "Predicting the Chemistry in CVD Systems," Proceedings of the Materials Research Society, Vol. 168, 1989.

87. Spear, K.E. and R.R. Dirkx, "Role of High Temperature Chemistry in CVD Processing," High Temperature Science, 27, 107-129, 1990.

88. Besmann, T.M. and K.E. Spear, "Analysis of the Chemical Vapor Deposition of Titanium Diboride I. Equilibrium Thermodynamic Analysis," J. Electrochem. Soc., 124 (5), 786-790, 1977.

89. Besmann, T.M., "Applications of Thermochemical Modeling to Chemical Vapor Deposition Processes," Proceedings of the First International Conference on Surface Modification Technology, Sudarshan and Bhat, eds., 311-325, 1988.

90. Cox, D.F., personal communications, May, 1991.

91. Butler, J. E., personal commumications, 1993.

92. Kingon, A.I., Lutz, L.J. Liaw, P. and R.F. Davis, "Thermodynamic Calculations for the Chemical Vapor Deposition of Silicon Carbide," J. Am. Ceram. Soc., 66 (8), 558-566, 1983.

93. Blocher, J.M., Browning, M.F. and D.M. Barrett, "Chemical Vapor Deposition of Ceramic Materials," Emergent Process Methods for High-Technology Ceramics, Vol. 17, Davis, Palmour, and Porter, eds., 299-315, 1984.

94. Sheehan, J.A., personal communications, July 1994.

95. Zaykoski, J.A., "Desiliconization of Mullite Whisker Felt," University of Maryland, Aug. 1988.

96. MKS Instruction Manual, "Type 1259 Mass Flow Controllers," MKS Instruments, 1990.

97. Powder Diffraction File, Joint Committee on Powder Diffraction Standards, International Center for Diffraction Data, Swarthmore, PA, 1993.

98. Snyder, R., personal communication, June 1990.

99. Snyder, R. L. and R.L. Bish, "Quantitative Analysis," Modern Powder Diffraction, Vol. 20, Bish and Post, eds., Mineralogical Society of America, Washington, D.C., 1989.

100. Wuchina, E.J., "The Hexagonal-to-Monoclinic Phase Transformation in Celsian," Master's Thesis, University of Maryland, April, 1991.

101. Besmann, T.M., personal communications, 1995.

102. Van der Brekel, C.H.J., "Characterization of Chemical Vapor Deposition Processes," Philips Res. Repts., 32, 118-133, 1977.

103. Besmann, T.M. and K.E. Spear, "Analysis of the Chemical Vapor Deposition of Titanium Diboride II. Kinetics," J. Electrochem. Soc., 124 (5), 790-797, 1977.

104. Wuchina, E.J., "Kinetic Examination of the Silicon Carbide CVD Reaction," Presentation at Annual Meeting of the American Ceramic Society, Pittsburgh, April, 1986.

105. Rao, C.N.R. and K.J. Rao, Phase Transformations in Solids, McGraw Hill Publishing Co., New York, 1978.

106. Klein, M. and B. Gallois, "Detemination of the Roughness of CVD Surfaces by Laser Scattering," Proceedings of the materials Research Society, Vol. 250, 85-92, 1991.

107. Vanderdrift, A., "Evolutionary Selection: A Principle Governing Growth Orientation in Vapour-Deposited Layers," Philips Research Reports, 22, 267-288, 1967.

108. Hurt, R.H. and M.D. Allendorf, "Rapid Growth of Ceramic Films by Particle-Vapor Deposition," CVD of Refractory Metals and Ceramics, Vol. 250, 59-64, 1992.

109. Sears, G.W. and R.C. DeVries, "Morphological Development of Aluminum Oxide Crystals Grown by Vapor Deposition," J. Chem. Phys., 19 (11), 2837-2845, 1963.

110. Lowden, R.A., personal communications, July, 1992.

111. Lowden, R.A., Reister, L. and M.A. Akerman, "Modification of Optical Surfaces Employing CVD Boron Carbide Coatings," Proceedings of the Materials Research Society: Chemical Vapor Deposition of Refractory Metals and Ceramics, 250, 173-178, 1991.

112. Lackey, W.J., personal communications, 1990.

113. Loonam, A.C., "Thermodynamics," Vapor Deposition, Powell, Oxley, and Blocher, eds., John Wiley and Sons, New York, 1966.

114. Bylander, E.G., "Kinetics of Silicon Crystal Growth from $SiCl_4$ Decomposition," J. Electrochem. Soc, 109 (12), 1171-1175, 1962.

115. Carlton, H.E., Oxley, J.H., Hall, E.H. and J.M. Blocher, "Kinetics of the Hydrogen Reduction of Boron Trichloride to Boron," Proceedings of the Second International Conference on CVD, x-x, 19xx.

116. Troyanov, S.I., Izmailovich, A.S., Tsirelnokov, V.I. and L.N. Komissarova, "Reaction of Hafnium (IV) Chloride with Metallic Hafnium," Russ. J. Inorg. Chem., 14 (4), 452-454, 1969.

117. Izmailovich, A.S., Tsirelnikov, V.I. and L.N. Komissarova, "Lower Chlorides of Hafnium," Russ. J. Inorg. Chem., 24 (9), 1309-1313, 1979.

118. Shinavski, R.J. and R.J. Diefendorf, "Reaction Kinetics of CVD Hafnium Diboride and Implications for Use as a Composite Matrix," Proceedings of the Twelfth International Conference on CVD, 385-391, 1993.

VITA

Eric Joseph Wuchina was born in Altoona, PA on November 29, 1964. After graduating from Beaver High School in 1983, he attended Virginia Tech and co-opped at Oak Ridge National Labs. Upon receiving a B.S. in Materials Engineering in 1988, he was hired by the Ceramic Science and Technology Group at the Naval Surface Warfare Center in Silver Spring, MD, and earned an M.S. in Engineering Materials at the University of Maryland in 1991. A fellowship from NSWC allowed him to return to Blacksburg to pursue a PhD in Materials Engineering Science. He is a member of the American Ceramic Society and the Materials Research Society. He is an avid traveler, spending much time on the road in the fall to attend Pittsburgh Steeler games in Three Rivers Stadium and Hokie games, both in Lane Stadium and less friendly environs. Upon graduation, he intends to play as much golf as possible, with a goal of breaking 80 in his newly found free time.